



**Defense Nuclear Agency
Alexandria, VA 22310-3398**



DNA-TR-95-76

Plasma Driven Water Shock

**Gary R. Hess
Mission Research Corp.
1720 Randolph Road, SE
Albuquerque, NM 87106-4245**

March 1996

Technical Report

CONTRACT No. DNA 001-91-C-0138

**Approved for public release;
distribution is unlimited.**

19960322 033

DOES QUALITY MATTER?

Destroy this report when it is no longer needed. Do not return to sender.

PLEASE NOTIFY THE DEFENSE NUCLEAR AGENCY,
ATTN: CSTI, 6801 TELEGRAPH ROAD, ALEXANDRIA, VA
22310-3398, IF YOUR ADDRESS IS INCORRECT, IF YOU
WISH IT DELETED FROM THE DISTRIBUTION LIST, OR
IF THE ADDRESSEE IS NO LONGER EMPLOYED BY YOUR
ORGANIZATION.



DISTRIBUTION LIST UPDATE

This mailer is provided to enable DNA to maintain current distribution lists for reports. (We would appreciate your providing the requested information.)

- ☐ Add the individual listed to your distribution list.
- ☐ Delete the cited organization/individual.
- ☐ Change of address.

NOTE:

Please return the mailing label from the document so that any additions, changes, corrections or deletions can be made easily. For distribution cancellation or more information call DNA/IMAS (703) 325-1036.

NAME: _____

ORGANIZATION: _____

OLD ADDRESS

CURRENT ADDRESS

TELEPHONE NUMBER: () _____

DNA PUBLICATION NUMBER/TITLE

CHANGES/DELETIONS/ADDITIONS, etc.)

(Attach Sheet if more Space is Required)

DNA OR OTHER GOVERNMENT CONTRACT NUMBER: _____

CERTIFICATION OF NEED-TO-KNOW BY GOVERNMENT SPONSOR (if other than DNA): _____

SPONSORING ORGANIZATION: _____

CONTRACTING OFFICER OR REPRESENTATIVE: _____

SIGNATURE: _____

CUT HERE AND RETURN



DEFENSE NUCLEAR AGENCY
ATTN: IMAS
6801 TELEGRAPH ROAD
ALEXANDRIA, VA 22310-3398

DEFENSE NUCLEAR AGENCY
ATTN: IMAS
6801 TELEGRAPH ROAD
ALEXANDRIA, VA 22310-3398

REPORT DOCUMENTATION PAGE			Form Approved OMB No. 0704-0188	
<small>Public reporting burden for this collection of information is estimated to average 1 hour per response including the time for reviewing instructions, searching existing data sources, gathering and maintaining the data needed, and completing and reviewing the collection of information. Send comments regarding this burden estimate or any other aspect of this collection of information, including suggestions for reducing this burden, to Washington Headquarters Services, Directorate for Information Operations and Reports, 1215 Jefferson</small>				
1. AGENCY USE ONLY (Leave blank)		2. REPORT DATE 960301		3. REPORT TYPE AND DATES COVERED Technical 910924 - 940331
4. TITLE AND SUBTITLE Plasma Driven Water Shock			5. FUNDING NUMBERS C - DNA 001-91-C-0138 PE - 62715H PR - RS TA - RF WU - DH315830	
6. AUTHOR(S) Gary R. Hess				
7. PERFORMING ORGANIZATION NAME(S) AND ADDRESS(ES) Mission Research Corp. 1720 Randolph Road, SE Albuquerque, NM 87106-4245			8. PERFORMING ORGANIZATION REPORT NUMBER MRC/ABQ-R-1742	
9. SPONSORING/MONITORING AGENCY NAME(S) AND ADDRESS(ES) Defense Nuclear Agency 6801 Telegraph Road Alexandria, VA 22310-3398 SPWE/DiNova			10. SPONSORING/MONITORING AGENCY REPORT NUMBER DNA-TR-95-76	
11. SUPPLEMENTARY NOTES This work was sponsored by the Defense Nuclear Agency under RDT&E RMC Code B4662D RS RF 00221 7010A AC 25904D.				
12a. DISTRIBUTION/AVAILABILITY STATEMENT Approved for public release; distribution is unlimited.			12b. DISTRIBUTION CODE	
13. ABSTRACT (Maximum 200 words) This report describes the development and testing of the Phase II Plasma Driven Water Shock (PDWS II) simulator as a continuation of the effort to develop a high energy density alternative to conventional high explosive (HE) water shock systems used for simulation of nuclear generated underwater shocks. The PDWS technique involves the rapid discharge of electrical energy, stored capacitively at high voltage, through a water plasma formed by electrical breakdown between fixed electrodes. The small volume of the plasma combined with extremely fast energy deposition results in a more nuclear like response than that obtained by the slower, more bulky HE energy release. Comparative experimental results have shown the necessity of rapid energy injection to achieve high coupling efficiency. There are strong implications based on these results for simulation using high explosives (HE) or numerical calculations that depend upon HE results. The fact that the coupling efficiency from the plasma to the water is strongly dependent upon the energy density for the microsecond time scales used here, implies that relationships developed for shock characteristic behavior from HE tests dependent upon available chemical energy or "yield" may be extremely suspect when applied to nuclear generated phenomena with radically different behavior than conventional explosives.				
14. SUBJECT TERMS UNDEX Water Shock Plasma Discharge			15. NUMBER OF PAGES 108	
			16. PRICE CODE	
17. SECURITY CLASSIFICATION OF REPORT UNCLASSIFIED	18. SECURITY CLASSIFICATION OF THIS PAGE UNCLASSIFIED	19. SECURITY CLASSIFICATION OF ABSTRACT UNCLASSIFIED	20. LIMITATION OF ABSTRACT SAR	

UNCLASSIFIED

SECURITY CLASSIFICATION OF THIS PAGE

CLASSIFIED BY:

N/A since Unclassified.

DECLASSIFY ON:

N/A since Unclassified.

EXECUTIVE SUMMARY

This report describes the development and testing of the Phase II Plasma Driven Water Shock (PDWS II) simulator as a continuation of the effort to develop a high energy density alternative to conventional high explosive (HE) water shock systems used for simulation of nuclear generated underwater shocks. The PDWS technique involves the rapid discharge of electrical energy, stored capacitively at high voltage, through a water plasma formed by electrical breakdown between fixed electrodes. The small volume of the plasma combined with extremely fast energy deposition results in a more nuclear like response than that obtained by the slower, more bulky HE energy release.

A shaped discharge has been successfully implemented to produce a spherical pressure wave from an effective energy density of 584 J/cm^3 as the source. This was accomplished with circuit efficiencies (η_c) as high as 72%. Both Tourmaline and PVDF gauges were used to measure the time dependent pressure. Shock rise times less than 200 ns were observed with PVDF gauges at 15 cm. Peak pressures of 11 MPa were recorded at 45 cm. Based upon conservative estimates (time limited integration of lower reading Tourmaline gauges) the highest plasma efficiency (η_p) was 18%. The highest total efficiency (η_T) was 3.1%.

Reflections internal to the plasma channel have been identified as the source of oscillations observed in the main part of the shock. The hydrocode simulations performed during both phases have shown this behavior as well and provided a means to determine characteristic frequencies at early times. Additionally, these simulations have shown that substantial energy can be added to the shock by reflecting energy from a high acoustic impedance surface.

For the energy deposition times tested in this phase, it has been shown that higher energies lead to lower coupling efficiencies from the plasma to the water. Specifically, the greater the energy per unit length of the discharge, the lower the coupling.

Also reduced energy injection times have been shown to have higher coupling efficiencies, but at the sacrifice of circuit efficiency for the circuit configuration tested.

Comparative experimental results have shown the necessity of rapid energy injection to achieve high coupling efficiency. In Phase I, the overdamped response demonstrated an estimated total efficiency of 40% while the oscillatory response had an estimated efficiency of only 14%. In Phase I though, the energy injection time was an order of magnitude faster (less than 300 ns). In Phase II, with energy injection times from 2 to 5 μ s, the total efficiencies were about an order of magnitude smaller (1 to 4%). The difference is believed to be due to thermal losses and poor coupling due to rapid separation of the shock from the vapor layer. With an assumed similar circuit efficiency (70%), subsequent analysis of hydrocode simulations with order of magnitude higher linear energy densities (5 kJ/cm) and instantaneous energy injection showed a total efficiency of about 8%.

What was believed at the time to be very large shock energies due to the comparatively greater loudness of Phase II over Phase I, is now attributed to bubble collapse. Although the coupling efficiencies were lower in Phase II, the circuit efficiency was just as high. This indicates that substantial energies were imparted to creation of steam and subsequent bubble growth. The estimated free-field bubble size for the 4-5 kJ plasma energies obtained in the experiment is approximately 21 cm in diameter with a period or time to collapse of 39 ms. The bubble collapse pressure would be extremely high in this case due to the bubble size.

There are strong implications based on these results for simulation using high explosives (HE) or numerical calculations that depend upon HE results. The fact that the coupling efficiency from the plasma to the water is strongly dependent upon the energy density for the microsecond time scales used here, implies that relationships developed for shock characteristic behavior from HE tests dependent upon available chemical energy or "yield" may be extremely suspect when applied to nuclear generated phenomena with radically different behavior than conventional explosives.

Additionally, the relatively higher temperatures associated with the plasma state found in electrical discharges and nuclear explosions due to their higher initial energy densities casts further doubt on HE comparisons. These effects and their relative importance in shock generation should be given priority for study rather than calculations, tests, demonstrations, or simulator development that provide estimates of "range to effect" that may bear no relationship to the physics of interest.

The current effort to develop a simulator using a water plasma is premature. Less emphasis should be placed on creation of a spherical wave for simulation and more attention should be devoted to development of a better understanding of the extreme time-scale sensitivity of the near field coupling from the plasma, early time thermal losses, and subsequent bubble behavior. If it is true that a nuclear event has only 60% of the efficiency of HE, it is possible that the subsequent bubble collapse could have an impulse close to or larger than the primary shock. This would result from the greater effectiveness at bubble growth for the higher temperature nuclear event than HE, in the same fashion as the water plasma. The implications of such a double-bang for structures response justifies the effort involved to determine if "fast-burn," high density energy release produces different bubble phenomena than HE. Based on the results of this experiment, nuclear coupling may be even less efficient than indicated above.

CONVERSION TABLE

Conversion factors for U.S. Customary to metric (SI) units of measurement.

MULTIPLY TO GET	BY BY	TO GET DIVIDE
angstrom	$1.000\ 000 \times E^{-10}$	meters (m)
atmosphere (normal)	$1.013\ 25 \times E^{+2}$	kilopascal (kPa)
bar	$1.000\ 000 \times E^{+2}$	kilopascal (kPa)
barn	$1.000\ 000 \times E^{-28}$	meter ² (m ²)
British thermal unit (thermochemical)	$1.054\ 350 \times E^{+3}$	joule (J)
calorie (thermochemical)	4.184 000	joule (J)
cal (thermochemical/cm ²)	$4.184\ 000 \times E^{-2}$	megajoule/m ² (MJ/m ²)
curie	$3.700\ 000 \times E^{+1}$	*gigabecquerel (GBq)
degree (angle)	$1.745\ 329 \times E^{-2}$	radian (rad)
degree Fahrenheit	$t_k = (t_f + 459.67)/1.8$	kelvin (K)
electron volt	$1.602\ 19 \times E^{-19}$	joule (J)
erg	$1.000\ 000 \times E^{-7}$	joule (J)
erg/second	$1.000\ 000 \times E^{-7}$	watt (W)
foot	$3.048\ 000 \times E^{-1}$	meter (m)
foot-pound-force	1.355 818	joule (J)
gallon (U.S. liquid)	$3.785\ 412 \times E^{-3}$	meter ³ (m ³)
inch	$2.540\ 000 \times E^{-2}$	meter (m)
jerk	$1.000\ 000 \times E^{+9}$	joule (J)
joule/kilogram (J/kg) radiation dose absorbed	1.000 000	Gray (Gy)
kilotons	4.183	terajoules
kip (1000 lbf)	$4.448\ 222 \times E^{+3}$	newton (N)
kip/inch ² (ksi)	$6.894\ 757 \times E^{+3}$	kilopascal (kPa)
ktap	$1.000\ 000 \times E^{+2}$	newton-second/m ² (N·s/m ²)
micron	$1.000\ 000 \times E^{-6}$	meter (m)
mil	$2.540\ 000 \times E^{-5}$	meter (m)
mile (international)	$1.609\ 344 \times E^{+3}$	meter (m)
ounce	$2.834\ 952 \times E^{-2}$	kilogram (kg)
pound-force (lbs avoirdupois)	4.448 222	newton (N)
pound-force inch	$1.129\ 848 \times E^{-1}$	newton-meter (N·m)
pound-force/inch	$1.751\ 268 \times E^{+2}$	newton/meter (N/m)
pound-force/foot ²	$4.788\ 026 \times E^{-2}$	kilopascal (kPa)
pound-force/inch ² (psi)	6.894 757	kilopascal (kPa)
pound-mass (lbm avoirdupois)	$4.535\ 924 \times E^{-1}$	kilogram (kg)
pound-mass-foot ² (moment of inertia)	$4.214\ 011 \times E^{-2}$	kilogram-meter ² (kg·m ²)
pound-mass/foot ³	$1.601\ 846 \times E^{+1}$	kilogram/meter ³ (kg/m ³)
rad (radiation dose absorbed)	$1.000\ 000 \times E^{-2}$	**Gray (Gy)
roentgen	$2.579\ 760 \times E^{-4}$	coulomb/kilogram (C/kg)
shake	$1.000\ 000 \times E^{-8}$	second (s)
slug	$1.459\ 390 \times E^{+1}$	kilogram (kg)
torr (mm Hg, 0° C)	$1.333\ 22 \times E^{-1}$	kilopascal (kPa)

*The becquerel (Bq) is the SI unit of radioactivity; 1 Bq = 1 event/s.

**The Gray (Gy) is the SI unit of absorbed radiation.

TABLE OF CONTENTS

Section	Page
EXECUTIVE SUMMARY	iii
CONVERSION TABLE	vi
FIGURES	viii
1 INTRODUCTION	1
1.1 TECHNICAL OBJECTIVES	1
1.2 TECHNICAL APPROACH	2
2 PHASE II SIMULATOR DESIGN	6
2.1 ELECTRICAL DESIGN	6
2.2 MECHANICAL DESIGN	11
2.3 ELECTRODE DESIGN	14
3 SMOOTH PARTICLE HYDRODYNAMIC CODE DEVELOPMENT ...	18
3.1 ACOUSTIC REFLECTOR	19
3.2 SMOOTH PARTICLE HYDRODYNAMIC CODE SIMULATIONS .	20
4 EXPERIMENTAL RESULTS	48
4.1 INTRODUCTION	48
4.2 ELECTRICAL PERFORMANCE	53
4.3 SHOCK PERFORMANCE	67
5 CONCLUSIONS	91
6 REFERENCES	94

FIGURES

Figure		Page
2-1	Circuit analysis results for Phase II pulsed power system design.	12
2-2	Layout of Phase II experiment.	13
2-3	Initial electrode design.	15
2-4	Final electrode design.	16
3-1	Strength of various commercially available ceramics.	21
3-2	Phase I SPH simulation showing progression of shock out to 1 cm and the time dependent pressure response at 0.25, 0.5, and 0.75 cm.	23
3-3	Phase I PDWS pressure pulse response at 30 cm.	24
3-4	SPH simulation of 10 cm plasma discharge in water demonstrates cylindrical shock wave (pressure in dynes/cm ²).	26
3-5	SPH simulation of 10 cm plasma discharge in water demonstrates reflecting boundary. Notice how the reflected shock disrupts the vapor bubble created by the discharge and how the spherical boundary focuses the reflected shock (pressure in dynes/cm ²).	27
3-6	SPH pressure probe time histories at 45° to 4 cm discharge axis show cylindrical dependence in wave and plasma internal reflection. . .	29
3-7	SPH simulation of alumina and water in planar geometry. Pressure time history at 1.5 cm from initial hot water slab adjacent to insulator (pressure in dynes/cm ²). Note how the reflection from the insulator isapproaching the initial outgoing shock.	31
3-8	SPH simulation of initial and insulator reflected shock waves in planar geometry at 2.5 μ s (pressure in dynes/cm ²). Note how the reflected shock has overtaken the initial shock.	32
3-9	SPH 2-D (infinite in z) geometry for curved insulator discharge simulation.	34
3-10	Peak mechanical power density vs. angle for straight and curved discharge simulations.	35

FIGURES (Continued)

Figure		Page
3-11	Velocity and time of arrival parameters vs. angle for shock produced from curved discharge simulation.	36
3-12	3-D geometry for SPH simulation of hemispherical alumina insulator and 20 kJ discharge to model expected configuration for Phase II experiment.	38
3-13	SPH geometry for the hemispherical insulator in the x-y plane (approximately at $z = 1.5$ mm) with the edge of the alumina identified and the locations of the probes both in the alumina and the water.	39
3-14	SPH results from 3-D simulation showing the peak pressures in the wave at the five probes and their distances from the origin of the problem. A line is also plotted to show the alumina surface relative to the origin.	40
3-15	Plot of the average velocity of the shock from the initial plasma boundary to the probes based on their distance from the boundary and the transit time from t_0 to the time of arrival of the shock.	41
3-16	Plot of the time dependent pressure response from the probe located 4.74 mm above the insulator in the water. Note the arrival time of the shock was about 380 ns which gives an average velocity from the plasma of 5895 m/s. Note also the primary shock and the apparent reflected shock from the alumina surface.	43
3-17	Plot of the response from the probe located 7.5 mm above the surface also in the plane of the discharge. Note how the reflected shock has overtaken the primary and only the internal reflection perturbation is visible.	44
3-18	SPH pressure field in x-y plane at 3.75 μ s. The vertical axis is x. The discharge occurs in the plane of the page. Note the sphericity of the main shock and the discontinuities in the secondary pulses which may be due to an instability. The pressure is in dynes/cm ² so the highest pressure in the shock front is 250 MPa.	45

FIGURES (Continued)

Figure		Page
3-19	SPH pressure field in the y-z plane at 3.75 μ s. The vertical axis is y. The bright red spot inside the alumina is due to a numerical instability. The discharge was into the page on the horizontal axis. Note the trend of spherical convergence. The pressure is in dynes/cm ² so the maximum real pressure is 325 MPa in the portion of the wave moving along the y direction. Along z the maximum pressure is 250 MPa and is coincident with the position of the shock in the x-y plane.	46
4-1	Circuit diagram for experiment. Note the load has been shorted and the resistance shown is that for the loop from the voltage monitor through the load.	50
4-2	Voltage for calibration shot with the load shorted out. The peak voltage was 65% of the charge voltage.	51
4-3	Current trace for calibration shot. The peak current was 22 kA or 7.86 times the charge voltage which indicates an impedance of 0.127 Ω	52
4-4	Geometry for electrodes and ceramic insulator/reflector that was used to support the initiation wire for the discharge and to form the discharge in a curve for shock wave shaping.	54
4-5	Voltage response (with and without the inductive correction) for a 3.7 cm discharge. Note that the underdamped response indicates a very low average plasma resistance.	56
4-6	Current response for a 3.7 cm discharge.	57
4-7	Electrical power for a 3.7 cm discharge. The reactive power is evident in the calculation with the uncorrected voltage monitor response.	58
4-8	Plasma energy for a 3.7 cm discharge. Note how even the inductively corrected data overshoots and oscillates about the final value due to the reactive power in the circuit. The 10-90% energy delivery time was 2.2 μ s.	59

FIGURES (Continued)

Figure		Page
4-9	Plasma resistance for a 3.7 cm shot. Note that the resistance falls three decades in 3.8 μ s.	60
4-10	Voltage response for a 9 cm discharge. Note that the response is highly damped indicating a much higher average plasma resistance for the longer discharge path. Also the inductive correction shows a fully damped response.	62
4-11	Current response for a 9 cm discharge.	63
4-12	Electrical power for a 9 cm discharge. Note that the inductive correction makes almost a 20% difference in the peak power.	64
4-13	Plasma energy for a 9 cm discharge. Note that the inductive correction completely removes the overshoot in the energy integral. Also the 10-90% energy delivery time is 4.2 μ s.	65
4-14	Plasma resistance for a 9 cm shot. Note that the resistance takes 8 μ s to fall three decades.	66
4-15	Tourmaline gauge pressure reading at 45 cm for Shot # 32. Note the strong rarefaction that appears to clip the pulse and the long duration responses out to 100 μ s.	69
4-16	Pressure response at 45 cm for Shot # 48. This shot also exhibits a strong rarefaction with an after pulse. Note that the channel saturated at about 4 MPa.	70
4-17	Overlay of pressure responses for Shots 32 and 48.	71
4-18	Shock energy density versus injected plasma energy. Note that the long discharge produced 30% stronger shocks from the same geometric 8.25 cm ³ volume. This demonstrates one of the main hypotheses of the experiment.	74
4-19	Shock energy density plotted against the 10-90% plasma energy injection time. The injection time has slightly stronger impact than the energy.	76

FIGURES (Continued)

Figure		Page
4-20	The shock energy density plotted against the linear plasma energy density (plasma energy divided by the discharge length).	77
4-21	The average plasma power density was obtained by dividing the linear energy density by the injection time. Although these data show the strongest dependence, the correlation is poor.	78
4-22	Plot of efficiency of coupling plasma energy to shock energy (η_p) The coupling efficiency falls off inversely with energy.	79
4-23	Plot of isotropic efficiency (η_p) versus linear energy density (E_l). In this case the coupling efficiency falls off inversely with the square of the energy density.	80
4-24	The coupling efficiency correlation with injection time is poor (0.71) due to a couple of outlying points. The efficiency scales as $t_p^{1/3}$	81
4-25	Very large scatter is observed in the coupling efficiency versus average linear plasma power density. In this case the efficiency scales as the square root of P_l	82
4-26	Plot of circuit efficiency (η_c) versus the discharge gap length. Note that the optimum efficiency was likely between 5 to 7 cm where a critically damped pulse would be expected to provide more energy than the overdamped discharges of 9 cm.	84
4-27	Plot of the total efficiency (η_T), obtained by the product of the coupling or isotropic efficiency and the circuit efficiency, versus the discharge length. Note that although the long discharges had very low coupling efficiencies, because of the higher circuit efficiency the total efficiency was higher.	86
4-28	Plot of range data for two shots with gauges positioned from 7.6 cm to 61 cm. The solid line is the relationship $E_d = 22.6 R^{-1.5}$	87
4-29	Plot of pressure data versus range for several shots. The 70 MPa, 3.81 cm point is estimated since the pressure was out of range for the gauge and digitizer. The dashed line is the best fit to the data and exhibits an R^{-1} dependence.	89

SECTION 1

INTRODUCTION

This report describes the development and testing of the Phase II Plasma Driven Water Shock (PDWS II) simulator. This is a continuation of the effort to develop a high energy density alternative to conventional high explosive (HE) water shock systems used for simulation of nuclear generated underwater shocks (Ref. 1). The PDWS technique involves the rapid discharge of electrical energy, stored capacitively at high voltage, through a dissociated water plasma formed by electrical breakdown between fixed electrodes. The small volume of the plasma combined with extremely fast energy deposition results in a more nuclear like response than that obtained by the slower HE energy release. The Phase I and II efforts demonstrated very high circuit efficiencies ($> 80\%$ stored energy converted to plasma energy) and high plasma efficiencies (Phase I, 50% and Phase II 18% plasma energy converted to mechanical energy). The combined efforts have shown the importance of very rapid energy loading (submicrosecond) for efficient conversion of plasma energy to a mechanical response.

The Phase I and Phase II efforts have provided the technology development necessary to scale the technology to very high peak powers from the one to ten gigawatts demonstrated to the tens of terawatts necessary to achieve scalable peak overpressures for simulation. The Phase II effort has also demonstrated a discharge gap implementation that effectively reduces the discharge volume to boost the energy density beyond that of conventional high explosives.

1.1 TECHNICAL OBJECTIVES.

The primary thrust of the PDWS II program was to develop the technology to produce a shock on a 1:3000 scale to a 100 kT nuclear generated shock. That is to say the peak and duration of the pressure pulse at one meter in the laboratory would be equivalent to that at 3 km due to a 100 kT device.

There were two specific areas of development which were addressed to achieve this objective: efficient loading of the appropriate amount of electrical energy into the discharge and keeping the discharge volume as small as possible. The first area was addressed through design of the pulsed power circuit based upon the Phase I results and within the funding constraints of the program. The second area was addressed by hydrocode simulation of the discharge interaction with the discharge gap structure and experimentation with the pulsed power circuit and the plasma discharge. Therefore, the two primary objectives for this Phase II program were: (1) to design and build a low impedance, well damped, high energy circuit to drive the discharge, and (2) to test the discharge to characterize the electrical and mechanical response and the resultant water shock. A secondary objective, to test the effects of bottom and surface conditions, was not investigated due to schedule and funding considerations. The key hypothesis was that the discharge channel could be shaped to produce a spherical shock from an essentially cylindrical plasma channel and produce a higher effective energy density. A secondary hypothesis was that backward propagating shock energy could be reflected from a high acoustic impedance surface and added to the main shock from the plasma.

1.2 TECHNICAL APPROACH.

The program was divided into five main tasks to accomplish the above objectives. The first task consisted of the efforts necessary to design the complete simulator pulsed power train, shock instrumentation tank and associated support systems. This involved the necessary analytical and numerical analyses and engineering design and drafting to provide the plans for fabrication and assembly of the pulsed power system and discharge gap. The second task was devoted to procurement, fabrication, assembly and checkout. A mechanically switched capacitor bank, discharge gap, deionized water system, shock measurement tank and pulsed power and shock diagnostics were specified and assembled. Measurement and characterization of the discharge and shock parameters were conducted in the third task. A selection of electrical energies was used to drive the discharge and shock measurements were made at various ranges. The fourth task was the bottom and surface effects testing

mentioned previously. The final task was production of the final report which presents the results of the program.

1.2.1 Task 1 - Phase II Simulator Design.

There were three main elements of Task 1. Mechanical design of the capacitor bank, switch, strip line electrical feed to the gap, discharge gap, tank and tank support systems directly supported the fabrication. Electrical design of the pulsed power circuit including electrical breakdown analyses of high voltage components provided the guidelines for the mechanical designs. Finally, two and three dimensional hydrocode analyses of an instantaneously loaded water plasma and voltage flashover surface were conducted to confirm the performance of a shaped discharge and optimized dielectric surface.

As described in the Phase II proposal, the ideal system would consist of a circuit that could deliver the entire desired plasma energy (20 kJ) in a few hundred nanoseconds. This megavolt level, one tenth terawatt device would necessarily be very large and very expensive and could not be accomplished in a Phase II effort. The choice was made instead to pursue a very low impedance ($< 0.1 \Omega$) switched capacitor circuit that could deliver this energy in a few microseconds. This would provide an order of magnitude higher electrical power than that demonstrated in Phase I and for similar efficiency levels would provide the energy density necessary to achieve the desired scaling.

1.2.2 Task 2 - Simulator Procurement, Fabrication, Assembly, and Checkout.

Once the designs were completed, procurement and fabrication were to start. Unfortunately the hydrocode model development had not proceeded as expected and permission to commence Task 2 was delayed until hydrocode results were available. Designs were implemented as quickly as possible and some used capacitors were utilized until the long lead-time capacitors were delivered. This minimized the impact of the delay.

One of the key aspects of the technology development was the electrical efficiency. A great deal of time was devoted to diagnostic development during the checkout that would allow measurements as close to the load as possible. Several designs of voltage and current probes were implemented before confidence was obtained in their accuracy simultaneously with their survivability. These issues were dealt with even into the testing task where shock measurements were conducted.

1.2.3 Task 3 - Shock and Discharge Characterization.

This task was devoted to shock measurements under conditions where the discharge gap-length, shape, energy, and power were varied. Both Tourmaline and PVDF gauges were used and shock rise times less than 200 ns were observed 15 cm from the discharge. Peak pressures of 11 MPa were observed at 45 cm. Maximum circuit efficiencies (η_c) of 72% were obtained. The largest plasma efficiency (η_p) obtained was 18%. The fundamental conclusion developed from this testing is described in more detail later, but the results essentially showed that energy must be loaded quickly before the water wall moves very far from the discharge. After a certain time (hundreds of nanoseconds), the shocked region has moved out to the point that subsequent energy loaded is transmitted acoustically through the plasma and is dissipated thermally rather than contributing to the main shock. This conclusion is supported both by hydrocode simulations and experimentation but to be strictly quantified will require additional research. There are numerous applications for this technology that are commercially based and environmentally strategic and dictate further study of this phenomena independent of the simulation objective. In spite of the decades of research that have been devoted to underwater plasmas, new things are learned daily that result in better understanding of this very complicated environment (Ref. 2).

1.2.4 Task 4 - Shock Effects Tests.

Due to many of the difficulties encountered during the testing, insufficient funds and time remained to complete Tasks 4 and 5. The objectives of Task 4 at the time the proposal was submitted were to study the effect of rock bottoms on the shock. Some anomalous behavior

had been observed in previous HE tests, but, in conjunction with hydrocode simulation, it was later shown that this was likely due to fractures in the bottom strata and so a joint decision was made to continue the characterization as long as funding would permit.

SECTION 2

PHASE II SIMULATOR DESIGN

2.1 ELECTRICAL DESIGN.

Basic design parameters were established by a simple scaling analysis and review of the Phase I results. The primary objective of the initial theoretical and experimental investigations was to demonstrate the feasibility of generating a pressure-time profile similar to that produced from underwater nuclear detonations with a high power electrical discharge (Plasma Driven Water Shock (PDWS)). Use of this technique has the potential to produce a response in water that has a much greater effective energy density than high explosives (HE) that have traditionally been used to simulate such detonations in lieu of actual tests. This technique also avoids the chemical combustion products that can contaminate the surrounding fluid and degrade the pressure response. Finally, a plasma discharge is more representative of nuclear-like energy deposition times and temperatures than HE. In the late forties, Cole advanced relationships that described the behavior of the pressure response with time, distance and source energy (Ref. 3). These relationships, shown below, and their corresponding coefficients were determined empirically from numerous tests with HE.

$$P(t) = P_m e^{-t/\tau} \quad (2.1)$$

$$P_m = k_p \left(\frac{W^{1/3}}{R} \right)^{a_p} \quad (2.2)$$

$$\frac{\tau}{W^{1/3}} = k_\tau \left(\frac{W^{1/3}}{R} \right)^{a_\tau}, \quad (2.3)$$

where

$P(t)$ \equiv pressure in psi

P_m \equiv maximum shock wave pressure

t \equiv time in ms

τ \equiv e-folding decay constant for the experimental pressure decay.

W \equiv explosive yield in kilotons (kT) for nuclear, pounds (lbs) for high explosive (HE) and inch-pounds (in-lbs) for electrical discharge (PDWS)

R \equiv range in ft

k and a are constants that match the shock wave peak pressure and decay behavior dependence on yield and range to experiment. The appropriate constants to be used for the various shock generating mechanisms are shown in Table 2-1.

Table 2-1. Constants for Cole's relations for various energy release mechanisms.

	k_p	a_p	k_τ	a_τ
Nuclear	4,380,000	1.13	2.274	-0.22
TNT	21,600	1.13	0.052	-0.23
C-4*	27,500	1.22	0.0454	-0.28
PDWS**	117	1.92	—	—

*Obtained by the Phillips Laboratory and NMERI (Ref. 4).

**Obtained from the plasma driven water shock demonstration conducted in Phase 1. (Note that the range (R) is in inches.)

The Phase I effort demonstrated peak pressures of 7.7 MPa (1120 psi) with 130 J estimated in the shock at 30 cm from the discharge. This also corresponds to about 0.1 gm TNT and therefore scales as 1:10,000 to 100 kT nuclear. An estimated 320 J of stored electrical energy was available to the plasma. This would correspond to a minimum electrical to mechanical conversion efficiency of 40% since some of the shock energy would be lost in propagation. This occurred in a plasma channel of 7 cm length and mm scale radius which would result in an energy density of 1 kJ/cm³. High explosives (TNT) provide an energy density of 6.92 kJ/cm³ by comparison. Thus if the discharge energy were boosted to 40 kJ, for the same volume, the energy density would be six times that of HE. It was desired to

demonstrate point source behavior in the shock rather than the cylindrical geometry described above. The solution was to reduce the effective volume of the discharge by forming it over a curved, electrically insulating and acoustically reflecting surface. With a 1.254 cm radius of curvature a 4 cm long discharge could be produced. This results in an effective volume of 8.24 cm³ or an energy density of nearly 5 kJ/cm³. The expectation was that much of the backward propagating energy would reflect from the dielectric and join the main shock. This would provide essentially twice the energy density depending upon the reflection coefficient. To be conservative though, if only 10 kJ were delivered to the plasma and the pressure followed a cube root dependence with yield, the Phase II device would be 1:2300 scale to 100 kT.

Previously used theoretical treatments for calculation of the resistance of the discharge were found to be inappropriate for the pulse shapes and time scales associated with the Phase I and II experiments. Therefore to estimate the energy loading which could be obtained in Phase II it was necessary to scale the Phase I results. The basis for this scaling was the common formula (Ref. 5):

$$W_d = \left(\frac{V_o^2}{4Z} \right) \tau_r \quad (2.4)$$

where

W_d = energy dissipated in the plasma discharge,

V_o = the voltage across the gap,

Z = the circuit impedance, $(L/C)^{1/2}$ (L and C are the circuit inductance and capacitance), and

τ_r = the resistive time of the discharge and dependent on the discharge gap (d) and the electric field ($E = V_o/d$).

The Phase I voltage, electric field, and impedance were approximately 315 kV, 50 kV/cm, and 2.5 Ω . The voltage fall time across the gap was 120 ns. The resistive time scales as

$E^{4/3}$ (Ref. 6). Therefore, to provide significantly more plasma energy and maintain high, effectively spherical, energy density, these parameters must be balanced. Gap reduction was necessary to support decreased effective volume and yet the electric field had to be reduced to provide greater resistive time. A maximum operating voltage of 100 kV was considered reliable. Over a 4 cm gap this provided a 25 kV/cm electric field, or a factor of 16 increase in resistive time. However, the factor of 3.15 reduction in voltage resulted in a factor of 10 decrease in the energy loading so the gain was only 1.6. This required a reduction of the impedance to 0.08Ω in order to obtain at least a 50 fold increase in plasma energy. The minimum expected obtainable inductance was 50 nH so an 8 μ F capacitance was necessary to achieve the desired impedance. At 100 kV this had a stored electrical energy of 40 kJ.

An estimated 335 J were in the Phase I discharge and so a predicted Phase II discharge energy was over 16 kJ with the times 50 scaling. Assuming the acoustically reflecting dielectric provided a gross acoustic impedance mismatch, 100% reflection with a 50% plasma to water shock coupling efficiency gave a 16 kJ shock at the origin with as much as 8 kJ expected at 30 cm due to losses. The estimated Phase I demonstrated electro-mechanical conversion efficiency was 40% at 30.5 cm, so for 40 kJ stored a 16 kJ shock was possible. If the Phase I shock energy, at this same range, was scaled by 50 a 6.5 kJ shock was possible. Based upon this 6.5 to 16 kJ range an expected minimum peak pressure was calculated from:

$$W_s = \left(\frac{4\pi R^2 P^2 \Delta t}{\rho C_s} \right) \quad (2.5)$$

where

W_s \equiv the shock energy in J

R \equiv the range from the discharge in m

Δt \equiv the full width half maximum (FWHM) pulsewidth in s

ρ \equiv the initial water density in kg/m³

c_s \equiv the shock velocity in m/s.

For 6.5 kJ and a scaled 20 μ s FWHM pulsewidth the peak pressure at 30 cm was calculated to be 20.8 MPa (3011 psi). This pressure was on the order of 1:3000 scale and deemed acceptable. Any higher shock energy or contributions due to reflection would only provide better scaling.

A stripline configuration to feed the electrodes was chosen since it offered the lowest expected inductance and could be reliably operated at 100 kV. Dimensions were maintained that kept surface electric fields below breakdown thresholds if the enclosure for the stripline was insulated with SF₆ gas. The inductance of a stripline is given approximately by:

$$L = 12.5 (dl)/w \quad \text{nH/cm} \quad (2.6)$$

where d is the gap between plates and l and w are the length and width respectively. The dimensions chosen were $d = 0.95$ cm (0.375"), $l = 50.8$ cm (20") and $w = 45.7$ cm (18"). This resulted in a calculated inductance of 13 nH. A 3/8" thick teflon sheet was used for the dielectric since it has a dielectric strength of 550 V/mil. This would support an electric field of 200 kV/cm or a factor of two higher field than expected at 100 kV DC capacitor charge voltage. The width and length were set primarily by the capacitor dimensions but also by the overall inductance of the circuit. Four capacitors in parallel were assumed to contribute 7.5 nH. The ground return to the stripline was assumed to have 13 nH and the electrodes and discharge were assumed to add 26.5 nH. This totalled 60 nH and would provide an impedance of 0.087 Ω .

To achieve at least 8 μ F with four symmetric connections, the individual capacitor value commercially available was 3 μ F. This brought the total capacitance value to 12 μ F. Therefore the stored energy would be 60 kJ and the impedance would be no more than 0.09 Ω even if the inductance was higher than estimated.

A circuit simulation was performed with the above parameters for a fixed resistance which idealized the circuit resistance and the required time averaged discharge resistance to achieve near critical damping. This circuit and the time dependent waveforms from the analysis are shown in Figure 2-1. The capacitor initial condition was 100 kV. The peak voltage obtained was 73 kV and the peak current was 530 kA. The power pulse was approximately 3 μ s wide at the base and had a peak of 38 GW. Ninety percent of the energy was delivered to the load in 2 μ s. Therefore if the plasma resistance was at least 100 m Ω the circuit efficiency would be 71% and 43 kJ would be delivered to the plasma. Note that a 100 m Ω load is close to the circuit impedance and therefore would exhibit the highest power.

Independent simulations of the circuit were performed by Tom Martin of Sandia National Laboratory with the circuit analysis code SCREAMER and an internal submodel which specifically treated the time dependent resistance presumably due to the plasma channel expansion. For the above same circuit parameters and a 3.0 μ s delivery time several gap lengths were simulated. The 2 cm gap dissipated 24 kJ, the 4 cm gap 37 kJ and the 8 cm gap 50 kJ. These simulations provided confidence that the electrical design would provide high efficiency and substantial energy for shock formation.

2.2 MECHANICAL DESIGN.

Figure 2-2 depicts the experiment lay out. The basic mechanical design consisted of an aluminum box which bolted to the capacitor flanges with a gasket to seal the interior. The high voltage plate was mounted to the capacitor high voltage terminals with 1.5" diameter aluminum standoffs which raised the plate to a safe distance to avoid breakdown to the box bottom which served as ground. The teflon insulator was placed over this plate and extended past the plate nearly to the walls of the box. The current return plate of the stripline was clamped in place to compress the dielectric and was strapped to the inside of the box to complete the electrical connection to the capacitor ground. This plate bolted to a feedthrough electrode which was O-ring sealed to a rectangular, PVC, SF₆/water interface flange bolted to the flat face of a D-shaped tank. The actual discharge electrodes were

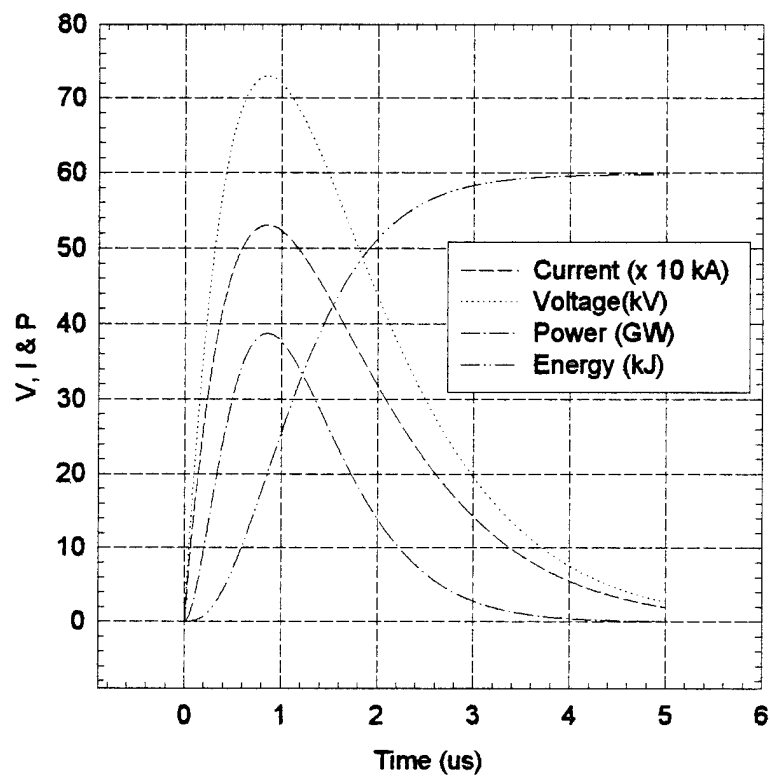
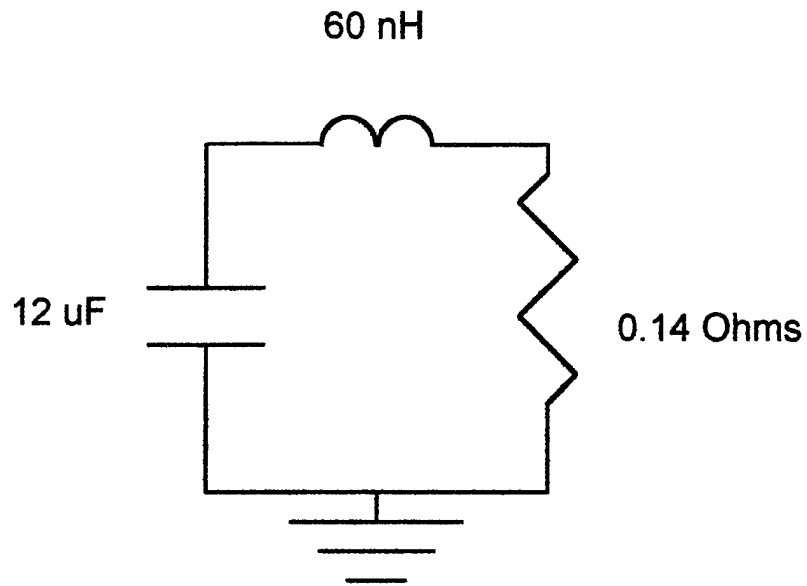


Figure 2-1. Circuit analysis results for Phase II pulsed power system design.

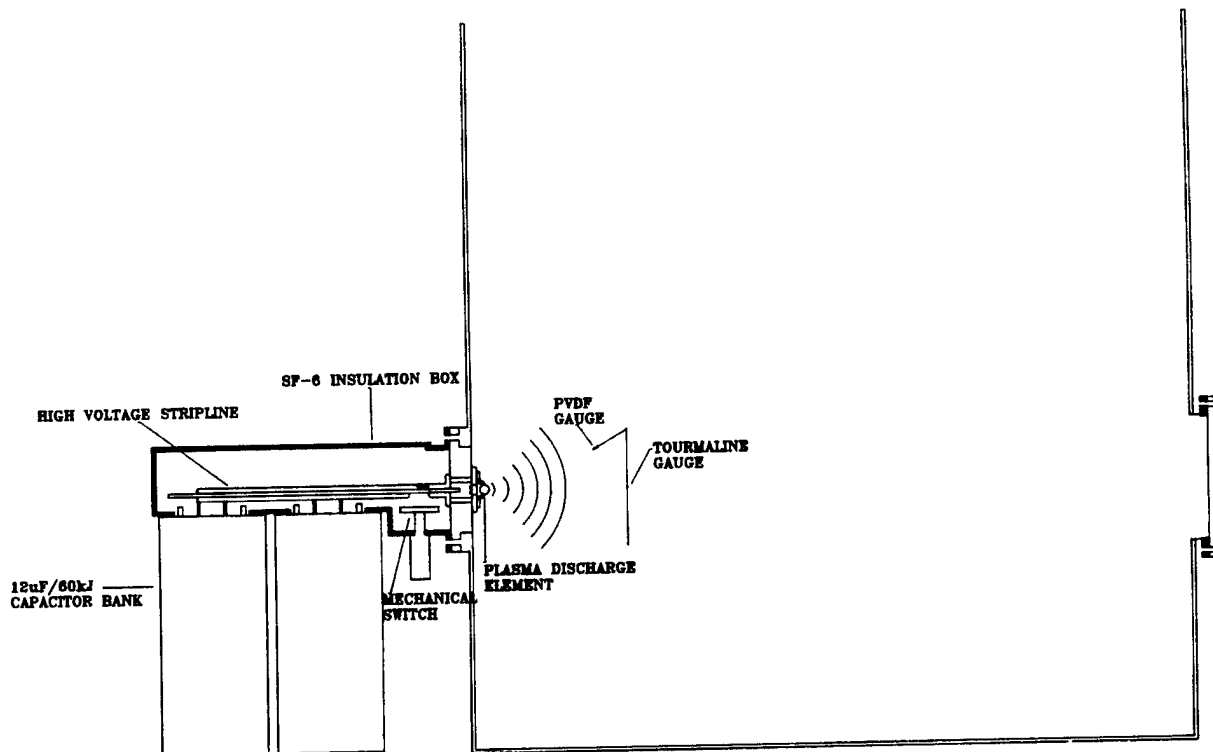


Figure 2-2. Layout of Phase II experiment.

attached to the other side of this feedthrough to serve as the cathode. Initially a Rogowski coil was imbedded in this feedthrough to serve as a current diagnostic. An identical anode was located below the cathode with a similar feedthrough, but minus the Rogowski. Initially several different voltage probe designs were attached to this feedthrough in the gas box. The electrical path was completed by a pneumatically driven brass plate to eliminate the losses inherent in a fluid switch.

An aluminum channel frame was magnetically attached to the tank walls and self locking clamps allowed crossmembers to be attached and easily repositioned. These crossmembers held PVC tube frames which held the tourmaline and PVDF gauges in position. Large viewports were welded to the tank to allow video diagnostics.

The tank was rested on high durometer ribbed rubber pads to minimize coupling of the shock into the concrete floor and to isolate the tank if it should float up in voltage.

The capacitor bank was mounted on a wheeled plate which could be raised and lowered with leveling legs. These legs also had rubber pads in contact with the concrete. This was a crude but effective way of damping the shock and reflections that the mechanical components were subjected to.

Twin 10 gpm deionizer columns with a bank of 0.2 micron filters were used to recirculate the water and filter out organics. A 3000 gal. polyethylene storage tank was permanently plumbed to the shock tank which allowed the tank to be drained and filled in approximately 15 minutes.

2.3 ELECTRODE DESIGN.

A set of stainless steel angle brackets were fabricated which held small Cu-W pins as the final conductors. A PVC backing bracket was clamped to the face of the electrical feedthroughs with the angle brackets. The PVC was machined to allow the surface flashover dielectric to be held in place with the Cu-W pins. This arrangement did not survive the higher energy shots and was replaced by cylindrical feedthroughs and a cylindrical SF₆/water interface flange. Unfortunately, this "two-wire" configuration had more inductance than the stripline geometry originally implemented. This is discussed in more detail in the experimental section.

The flashover dielectric chosen was Alumina. This material had the highest acoustic impedance of the readily available ceramics in addition to high compressive strength. One inch diameter slugs were purchased which provided a 4 cm direct discharge path length over the front surface. To ensure that the discharge would form where desired a 1 mil copper wire was installed over the ceramic piece. Figures 2-3 and 2-4 show the initial and final electrode designs. The final electrodes were 1.5" diameter stainless steel and after tens of shots the surface directly exposed to the shock was badly crushed. However this final design successfully implemented the discharge pins vertically to prevent their destruction and a sacrificial backing plate that prevented direct damage to the feedthrough flange. Indirect shock transmitted to the feedthrough flange from the cylindrical electrodes resulted in a

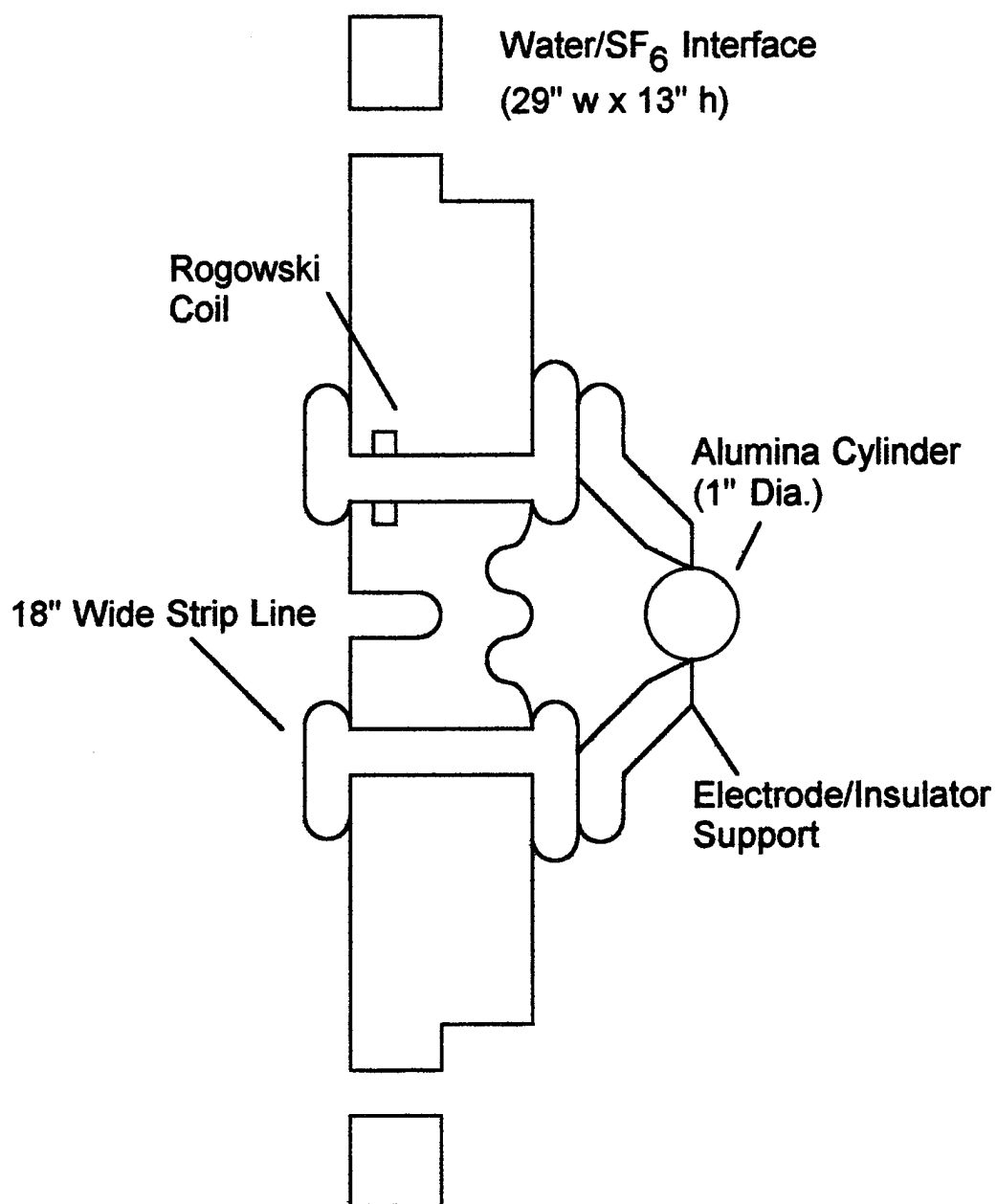


Figure 2-3. Initial electrode design.

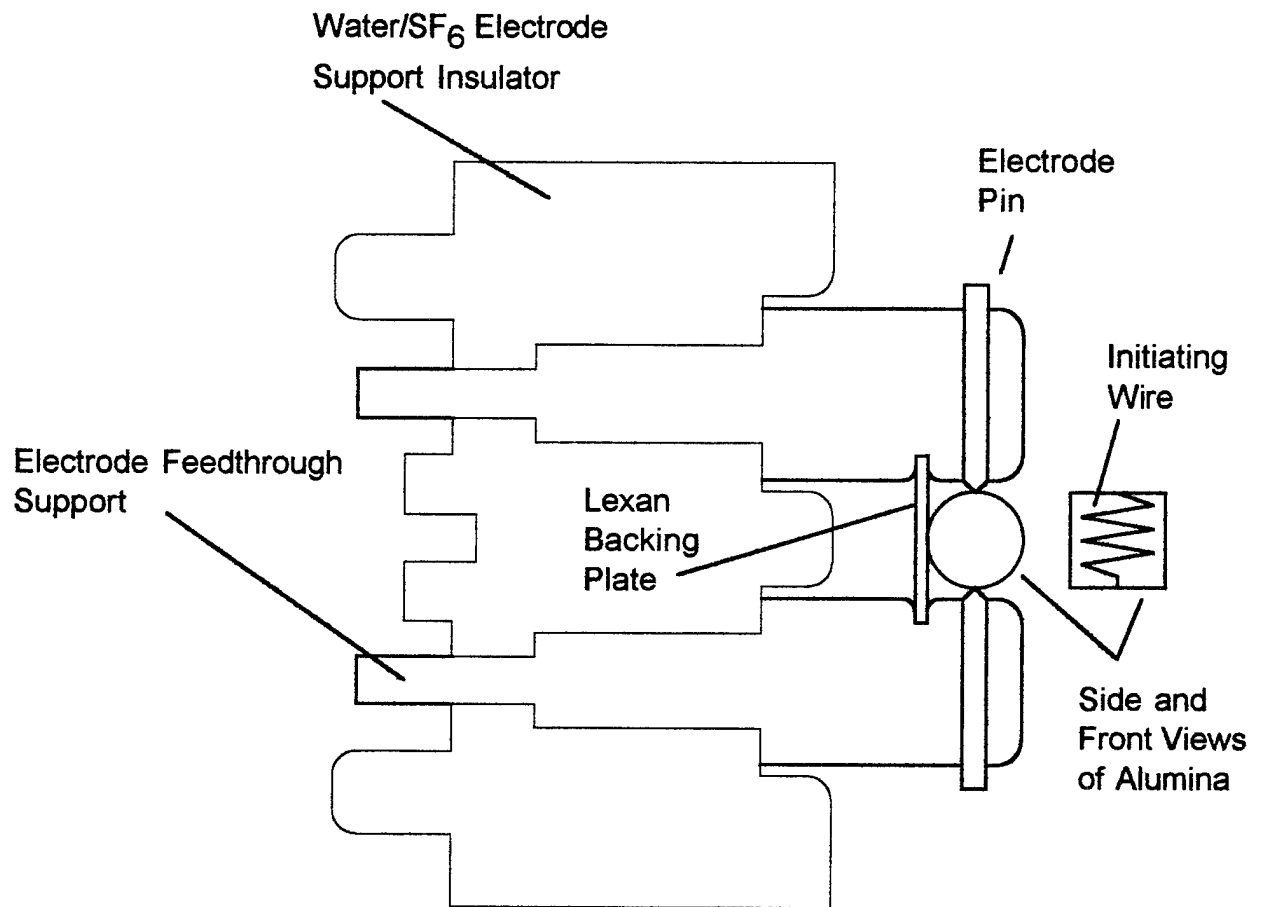


Figure 2-4. Final electrode design.

complete catastrophic failure of the feedthrough flange after every 20 shots. These flanges were made of G-10 and later PVC. Other materials were considered that would have been mechanically stronger, but they were not manufactured in the size needed to machine to shape and custom casting was financially prohibitive. The choice of alumina was made based upon a study of ceramic properties. Simulations of the shock interaction with this material were conducted during the design phase and are described in the next section.

SECTION 3

SMOOTH PARTICLE HYDRODYNAMIC CODE MODEL DEVELOPMENT

When a plasma discharge, chemical detonation or nuclear detonation occurs in water, there is an immediate, very intense pressure wave created in the surrounding fluid. Because a density gradient develops across the width of this response, the portion of the wave behind the front travels faster and the pressure wave front steepens. This is the formation of a shock wave with a velocity that exceeds the sound speed in the ambient fluid medium until energy losses and geometric effects result in degradation of the shock front and the wave slows to the acoustic speed. Near the source, immediately behind the shock, a rarefaction occurs that propagates backward to the center of the energy deposition and, in water, a bubble is formed. This bubble will continue to grow as the interior cools and the fluid/vapor boundary expands at a lower rate than the outgoing shock (much less than the sound speed). Therefore, at some point in this process, the outgoing shock detaches from the fluid/vapor wall and the bubble grows into the stagnating water. If energy is still being added, it will contribute to the growth of the bubble but not to the intensity of the shock. Because of the inertia of the bubble wall and the difference in density between the water and the vapor, acoustic reflections may occur in the interior. The hydrocode simulations performed during both phases have shown this behavior which explains experimentally observed oscillations in the tail of the shock.

Further model development of the shock response and interaction with a reflector was continued under the Phase II effort with the Smooth Particle Hydrodynamic code (SPH). Initially a 2-D cylindrical channel geometry with a 10 cm length was modeled to compare to the Phase I, 1-D simulations. A 4 cm length was then modeled since this represented the expected Phase II geometry. This model was extended to 3-D for the same length, but wrapped over an alumina surface of 1.25 cm curvature radius. The rationale for the use of alumina and the results of the modeling are described below.

3.1 ACOUSTIC REFLECTOR.

In the near field, a cylindrical discharge will produce a cylindrical wave which defeats the purpose of simulating a detonation which effectively originates from a point. In order to have high electrical efficiency a long gap is necessary to ensure the maximum dissipation of energy in the plasma. By forcing the discharge over a curved surface this high electrical efficiency could be maintained while the effective volume of the source was reduced. Spherical wave behavior could be forced in the near field to more closely simulate a point source. Of course, to increase the effective energy density it was necessary to reflect as much of the backward propagating energy into the forward half sphere as possible. Ideally the discharge would occur over a half sphere on an infinite, planar dielectric which would positively reflect the backward incident wave into the outgoing shock in the water.

Water has a density (ρ) of 1 g/cm^3 and a sound speed (c) of $1.5 \times 10^5 \text{ cm/s}$. The specific acoustic impedance is given by the ρc product and for water is $1.5 \times 10^5 \text{ g/cm}^2\text{-s}$. For air the impedance is $42 \text{ g/cm}^2\text{-s}$. An acoustic wave incident from water onto air will reflect with a negative pressure since the impedance of air is less than that of water. In fact, it will reflect nearly 100% because of the extreme difference in the impedances. This is called a free-surface reflection. Analogous to this is a reflection from a surface with a higher acoustic impedance but with positive pressure. Table 3-1 shows the corresponding values specific to various ceramics that would be candidates for a positive reflector and surface flashover dielectric surface.

Note that although beryllia has the highest sound speed, it has the lowest density and zirconia has the highest density, but it has nearly the lowest sound speed. Consequently the material of choice was alumina because it has the highest acoustic impedance ($3.8 \times 10^6 \text{ g/cm}^2\text{-s}$) which is 25 times greater than that of water. Consequently, the alumina/water interface would reflect 92% of the incident energy. For a $20 \text{ }\mu\text{s}$ pressure pulse, the ceramic would have to be 10 cm thick so that any free surface behind the ceramic would be far enough away to avoid clipping the shock with a negative pressure or rarefaction wave.

Table 3-1. Ceramic insulator characteristics (Ref. 7).

Material	ρ (g/cm ³)	E ($\times 10^6$ psi)	Longitudinal Velocity (m/s)
AlN	3.26	45	9756
Al ₂ O ₃ (sintered, ~5% porosity)	3.965	53	9600
BeO (~5% porosity)	3.01	45	10153
3Al ₂ O ₃ •2SiO ₂ (mullite porcelain)	3.156	10	4674
ZrO ₂ (sintered, stabilized, ~5% porosity)	5.6	22	5204

From Figure 3-1, alumina has a Young's modulus equal to that of steel. So it was also expected to be strong enough to support the compressional wave.

3.2 SMOOTH PARTICLE HYDRODYNAMIC SIMULATIONS.

Multi-dimensional simulations with the Smooth Particle Hydrodynamic (SPH) code were performed. SPH is a gridless, Lagrangian hydrodynamic technique that offered many advantages over more traditional computation techniques. SPH has been tested on a variety of shock propagation problems including the Noh, Sod and Sedov/von Neumann adiabatic blast wave. For the Phase I and Phase II problems SPH was an attractive approach because it runs in 1, 2 or 3 dimensions and offers a variety of physics models. Thus, rather than a simple replication of the experiment, the computation served as a tool to understand the effects of geometry and structural interactions important to the achievement of higher effective energy density.

In Phase I, simulations were performed with a 0.1 cm portion of the 1 cm problem volume instantaneously heated to 2500 K which is the equivalent of 330 J/cm of energy released. The effects of this instantaneous deposition were observed by snapshots (in time) of the

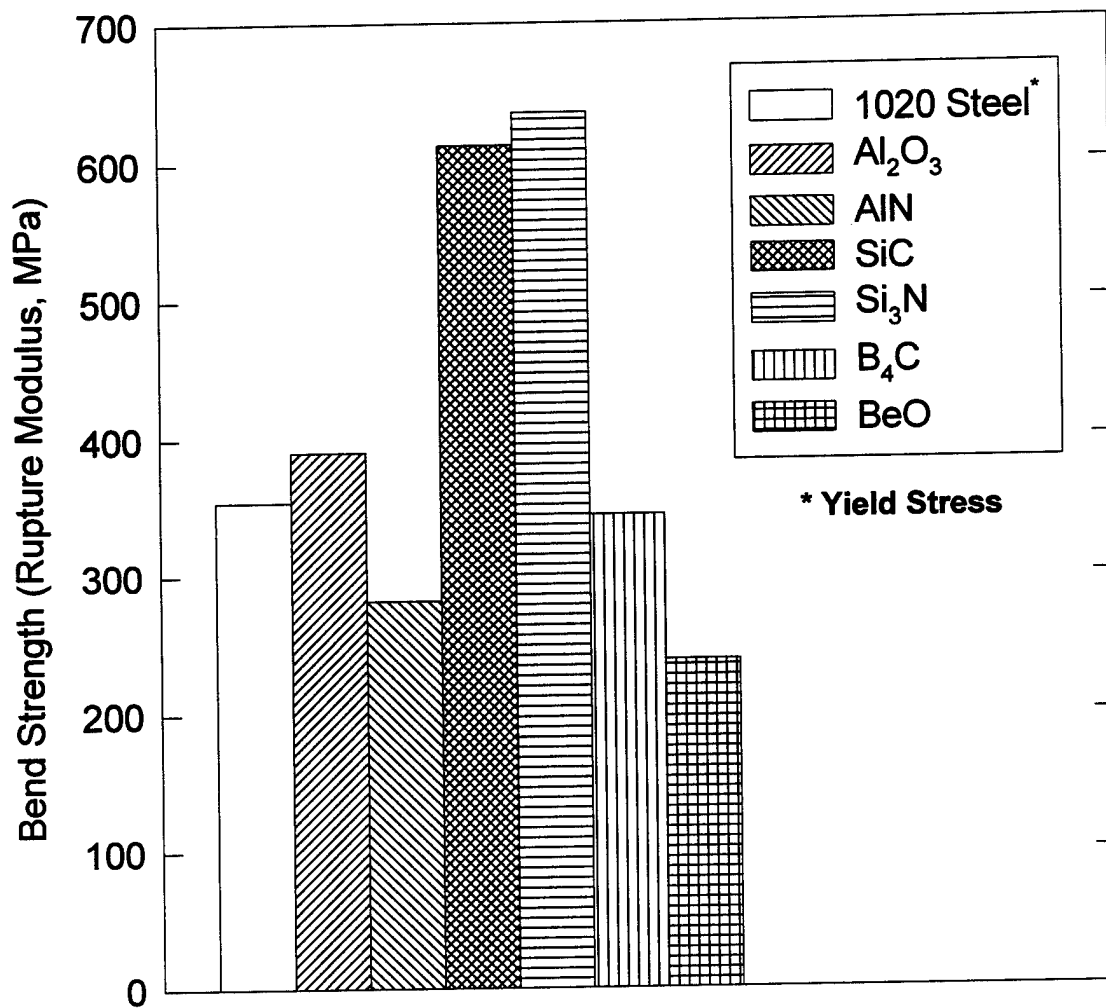
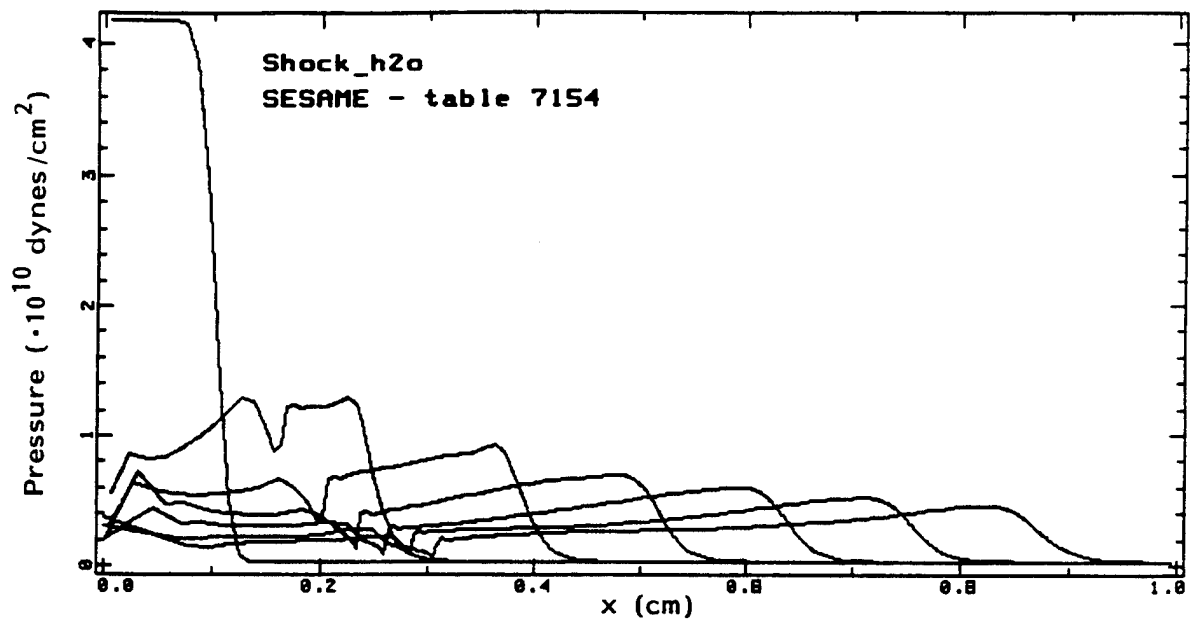


Figure 3-1. Strength of various commercially available ceramics.

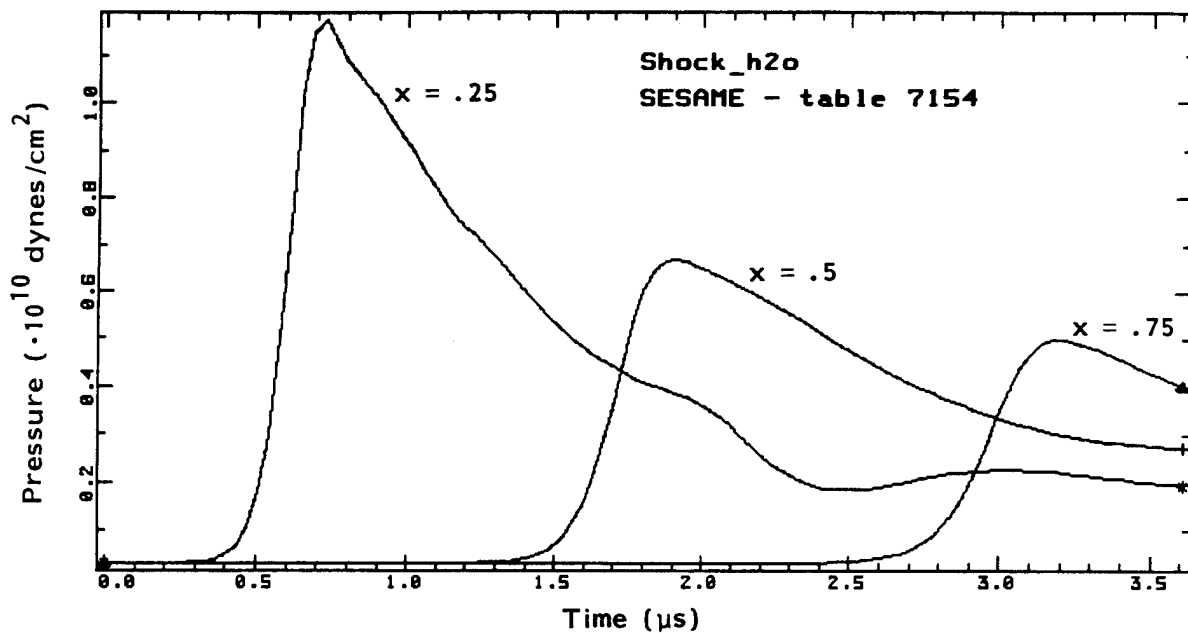
pressure throughout the problem volume and by pressure probes spaced 0.25, 0.5 and 0.75 cm away from the origin.

Figure 3-2 shows the progression for a one dimensional simulation in a cylindrical geometry using the SESAME tabular equation of state for water from Los Alamos National Laboratory. Note that at $t = 0$, the pressure in the heated interior is 4.19 GPa (41.5 kbar) and the ambient pressure is 101 kPa (1 bar). After the first half microsecond the peak pressure in the propagating wave has fallen to nearly one fourth that value and an oscillation with a wavelength of 0.5 mm has occurred. This oscillation only propagates 1.5 mm in the time the outgoing shock has travelled 6 mm. From the lower plot in Figure 3-2 it can be seen that the average velocity of the shock from 0.25 to 0.5 cm was about 2200 m/s. So the sound speed behind the shock is an average of about 550 m/s. This is only a little higher than that of air at room temperature which is 350 m/s. At 550 m/s a 0.5 mm wavelength represents a 1.1 MHz frequency. At 2200 m/s, a 1.1 MHz frequency wave has a 2 mm wavelength which is the same as the two-way transit distance in the original plasma channel. Since the original channel density was the same as ambient it can be surmised that the oscillation is the result of reflections internal to the plasma channel and result from the plasma/water boundary.

Initially it was thought that this reflection was an artifact of the problem initial conditions. In a practical situation, the water would undergo high voltage stress prior to ionization with some pre-breakdown current leading to full current. The full current would have a finite rise time controlled by circuit parameters and the resistance of the discharge. Therefore the energy would be introduced over time and a more gradual channel growth would result. However, from Figure 3-3 we can see the same type of perturbation following the shock front still evident 30 cm away (666.4 microseconds after the ≈ 200 ns discharge) in the Phase I experiment. Note the perturbation is about 6 μ s after the shock peak and has a characteristic period of about 1 μ s. In this case the discharge gap was 7 cm in length. At 1500 m/s if this were a structural reflection, the reflecting surface would have had to have been 4.5 mm from the shock source. Since the nearest structure from the center of the source was 3.5 cm, the perturbation is clearly part of the incident shock. The FWHM shock



Propagating pressure pulse every 0.6 μ s



Time response of pressure at 0.25, 0.5, and 0.75 cm

Figure 3-2. Phase I SPH simulation showing progression of shock out to 1 cm and the time dependent pressure response at 0.25, 0.5, and 0.75 cm.

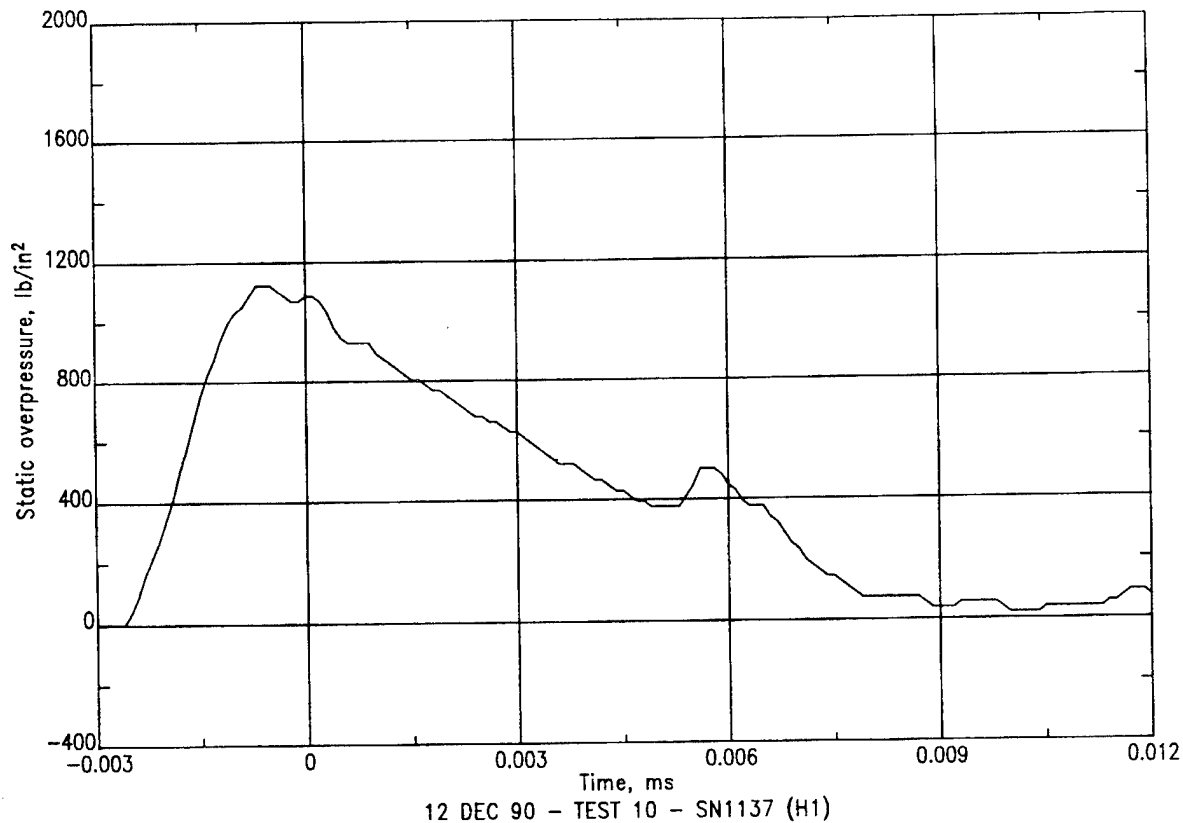


Figure 3-3. Phase I PDWS pressure pulse response at 30 cm.

pulsewidth was $4.5 \mu\text{s}$ and the energy was delivered in less than 5% of this time. Over the 200 ns delivery time the plasma channel could have grown to a millimeter scale diameter. The characteristic wavelength of the perturbation is about 1.5 mm which is consistent with the estimated channel diameter. More recent simulations on an unrelated project with a newer version of the code have demonstrated the same internal reflection behavior (Ref. 8). Evidently the phenomena is real and probably can be expected to occur in nuclear generated shocks as well.

The first simulations in this phase of the effort were intended to compare to the Phase I results from the 1-D cylindrical geometry. Table 3-2 shows the parameters for a run in 2-D cylindrical coordinates. The "plasma discharge" was represented by a small uniformly hot region with zero initial velocity and a steep temperature gradient at the boundary. To keep the number of particles to a reasonable level, yet be able to see the pressure response out to 15 cm, the resolution had to be reduced. So in this case, the initial radius was 3 mm. In

order to match the peak initial pressure over the 10 cm discharge length in 2-D, the linear energy density had to be greater. In retrospect, matching the energy density would have been more appropriate. Useful information was obtained, however.

Table 3-2. SPH parameters for 10 cm discharge in water.

Region →	Plasma Region	Background Region
Substance →	H ₂ O	H ₂ O
Initial temperature	2,500 K	300 K
Peak initial pressure	4×10^{10} dynes/cm ² (40 GPa)	—
Initial density	1 g/cm ³	1 g/cm ³
Number particles	100	10,000
Energy density	8.4 kJ/cm	—
Length	10 cm	(15 cm × 2)
Radius	0.3 cm	15 cm
Materials Method	SESAME	SESAME
Boundary	Free	Reflecting

Snapshots of the problem volume pressure in the vertical plane are shown in Figures 3-4 and 3-5 (a, b upper left to right; c, d lower left to right) in 10 μ s increments for the first 30 μ s and then for 30 μ s after the incident shock has reflected from the boundary. In Figure 3-4a the hot core initial condition is shown. As early as 10 μ s (Figure 3-4b) the shock has detached from the hot plasma and has moved several channel diameters from the initial channel wall. After 20 μ s, a rarefied region behind the shock encloses a still hot, but cooled core. Any additional energy added after 10 μ s, in this case, would not be expected to couple to the outgoing shock since it would travel through this region with a significantly lower velocity. At 30 μ s, a distinct dumbbell shaped bubble has formed in the interior that has approximately an 18 mm radius. This is an average bubble wall velocity of 500 m/s. The

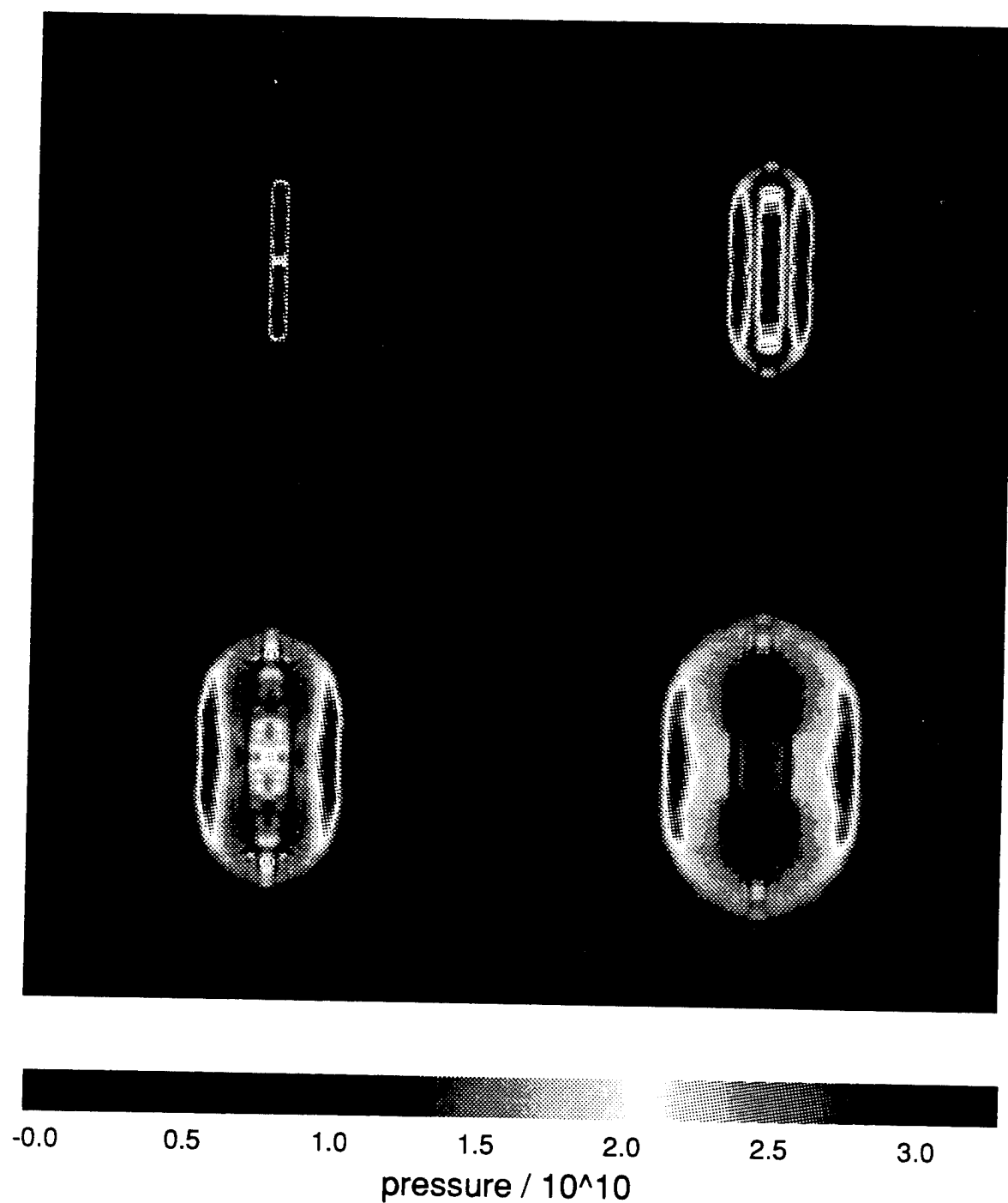


Figure 3-4. SPH simulation of 10 cm plasma discharge in water demonstrates cylindrical shock wave (pressure in dynes/cm²).

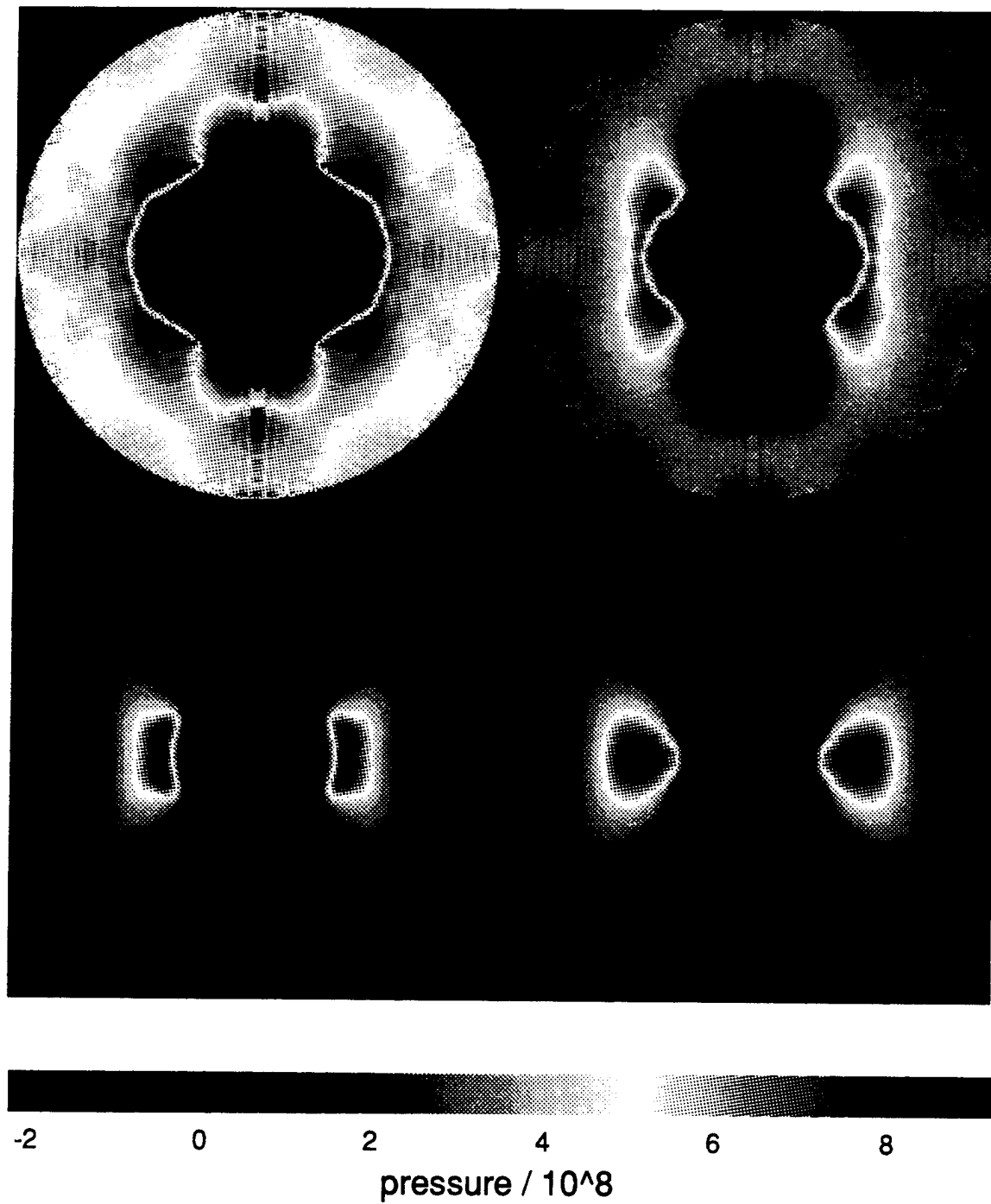


Figure 3-5. SPH simulation of 10 cm plasma discharge in water demonstrates reflecting boundary. Notice how the reflected shock disrupts the vapor bubble created by the discharge and how the spherical boundary focuses the reflected shock (pressure in dynes/cm²).

expanding shock wave remains cylindrical throughout the entire problem, but is reflected and focused from the boundary.

Note (Figure 3-5a) that by 160 μ s the reflected shock has encountered the bubble and caused it to distort. Without the reflection the bubble would have continued to grow to a substantial radius. Thus any reflections from surrounding structures could be expected to severely impact the natural bubble growth that occurs after the energy release.

Note also in Figure 3-5 how the spherical boundary has focused the shock from the initial cylindrical shape to a collapsing toroid. This demonstrates the ability of the code to deal with reflections. This was important for the design of the discharge electrodes.

An additional run was performed in order to obtain results for a 4 cm free-field (no reflecting boundary) discharge. In this case 20 kJ total energy was the initial condition. This was the expected plasma energy for the Phase II experiment. Figure 3-6 shows the time-domain pressure at three points away from the discharge. Probes were inserted in the simulation at 0.5, 1.5 and 3 cm ranges on a line 45° to the axis of the discharge to show the cylindrical shape of the shock. Note again the secondary reflection in the response. The peak pressure falls off with distance as would be expected but note that this occurs much more rapidly than $1/R$. This is due to the cylindrical shape consistent with the profiles shown in Figure 3-4. Also there seems to be an angular dependence in the strength of the secondary reflection, that was apparent in Figure 3-4d as well, where the secondary reflection appears to emanate only perpendicular to the discharge axis.

The linear energy density for this run was 5 kJ/cm. Estimates of the total shock energy at 0.5 μ s into the simulation indicated a coupling efficiency of only 17% (3400 J). Approximately 17 kJ is portioned into the multi-phase fluid behind the shock. At 6 μ s, the sausage shaped bubble had grown to a 1.2 cm diameter (7.4 cm³) with an average internal temperature of 3000 K. This represents an average bubble wall velocity of 750 m/s. Note that, at this time, the shock was out to nearly 2 cm from the initial channel and had an

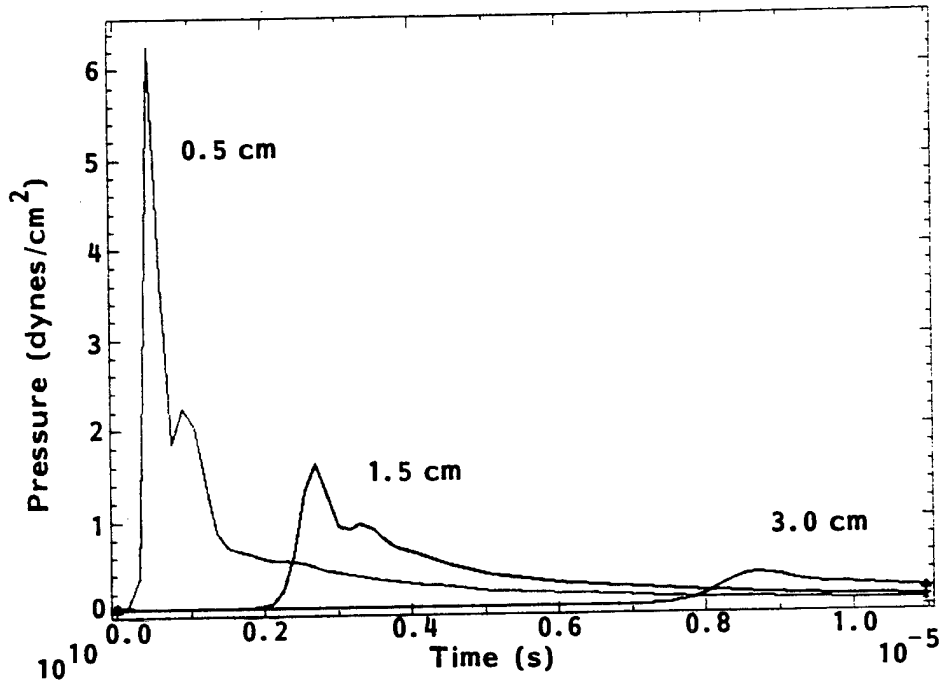


Figure 3-6. SPH pressure probe time histories at 45° to 4 cm discharge axis show cylindrical dependence in wave and plasma internal reflection.

average velocity of 3000 m/s. As early as 3 μ s the bubble was over 0.25 cm behind the tail end of the shock wave which indicates rapid separation of the plasma/ shock boundary.

Cole derived a relationship for the energy associated with radial water flow (Y) as a function of the experimental bubble radius (R_b)

$$Y = \frac{4\pi}{3} P_o R_b^3 \quad (3.1)$$

where P_o is the hydrostatic pressure at the explosion depth (Ref. 3). A corresponding relationship describes the bubble oscillation period (T_b) or time to first collapse

$$T_b = 1.83 R_b \left(\frac{\rho_o}{P_o} \right)^{1/2} . \quad (3.2)$$

This relationship can be expressed in terms of the work by the Willis relation (Ref. 9):

$$T_b = 1.14 \rho_o^{1/2} \frac{Y^{1/3}}{P_o^{5/6}} \quad (3.3)$$

Y can be related to the HE charge weight (W) or the plasma energy (E_p) empirically with a constant that reduces the total available energy by that portioned to the outgoing shock and the internal energy stored in the gas or plasma. In the case of a plasma where η_p = shock energy/plasma energy,

$$T_b = 1.14 \left(\frac{\rho_o^{1/2}}{P_o^{5/6}} \right) [(1 - \eta_p) E_p]^{1/3} . \quad (3.4)$$

The bubble radius can be found from

$$R_b = 0.623 \left[(1 - \eta_p) \frac{E_p}{P_o} \right]^{1/3} \quad (3.5)$$

For the above run $\eta_p = 0.17$ so the bubble produced would reach a radius of 34 cm and would collapse after 62 ms. This would be a huge bubble.

To test the ability to use a ceramic reflector, a 2-D planar geometry run was simulated. In this case a 4 cm wide slab of Alumina was insulated by a slab of ambient fluid (0.5 mm thick by 4 cm wide). The equation of state for Al_2O_3 was also available in the SESAME table at Los Alamos. Adjacent to this a square tube of heated fluid (0.5 mm per side) was used to simulate a discharge over a ceramic surface. Figure 3-7 shows the time history out to 2.5 μs . Note the same secondary reflection due to the channel still appears about 1 μs after the primary peak, but between this response and the primary is the reflected pulse from the Alumina surface only 0.3 μs behind the primary peak. This juxtaposition shows that the reflected pulse from the alumina has travelled through the water compressed by the outgoing shock and is catching up to it. This is more evident in Figure 3-8 where it is seen that when the primary reaches 2 cm the alumina reflected pulse has merged with the primary. Physical justification for use of an alumina reflector was shown by this run.

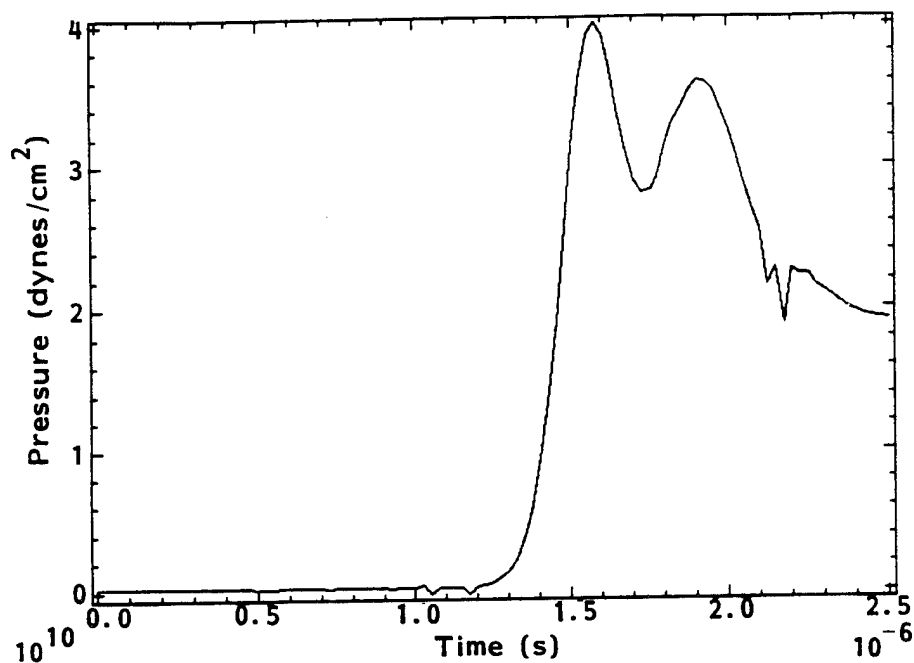


Figure 3-7. SPH simulation of alumina and water in planar geometry. Pressure time history at 1.5 cm from initial hot water slab adjacent to insulator (pressure in dynes/cm²). Note how the reflection from the insulator is approaching the initial outgoing shock.

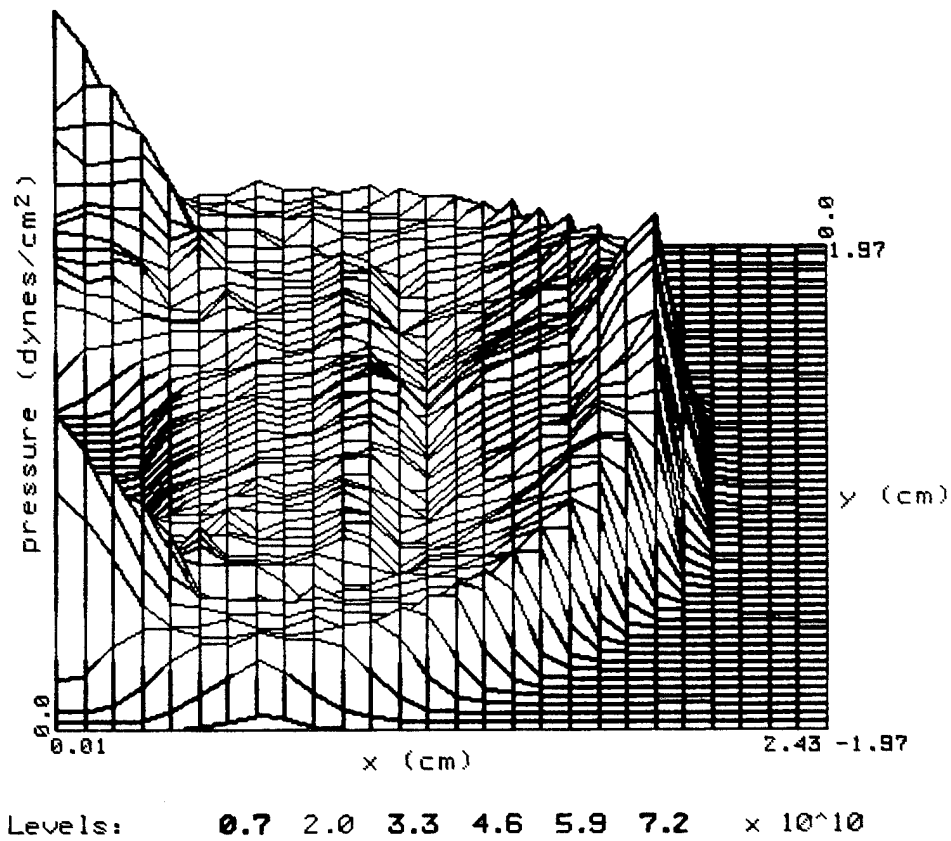


Figure 3-8. SPH simulation of initial and insulator reflected shock waves in planar geometry at 2.5 μ s (pressure in dynes/cm²). Note how the reflected shock has overtaken the initial shock.

The next step in these simulations was to provide a curved surface over which the discharge could track in order to compress the effective volume from which the shock would emanate. This was expected to provide a more point source like behavior. Figure 3-9 shows the 2-D geometry for these simulations. In this case the radius of curvature of the surface was 2.0 cm and the simulation was run until the shock propagated 1.0 cm away from the surface. Any further propagation would have resulted in excessive run times. Initial 3-D runs on the DNA/LANL Cray had indicated that this machine would have insufficient memory to run the full problem (500,000 particles) which would allow direct comparison with the experimental data to be taken at 30 cm. The key issue with the curved insulator was to determine if a spherical wave could be produced from such a geometry.

Figure 3-10 is a plot of the peak mechanical power density (P_d) at 0.5 cm from the insulator surface vs. angle for a curved and a straight discharge. The angle is taken from the probe position relative to the y axis in the x - y plane. The peak mechanical power density is calculated from the pressure by

$$P_d = \frac{P^2}{\rho c} \quad (3.6)$$

where P is the peak pressure and ρc is the acoustic impedance (density times the sound speed). Note how the pure cylindrical wave intensity falls to only 30% of the peak at 30° and to essentially zero at 90° as expected while the curved discharge provides a wave that maintains 80% of the peak-on-axis intensity out to 60° and falls to only 30% of the peak at 90° . This is nearly a spherical wave in the x - y plane at only 0.5 cm. As the wave propagates further it will converge to spherical well before the experimental measurement range.

Figure 3-11 plots the power density at 0.5 cm, average velocity from 0.5 to 1.0 cm and the time of arrival at 0.5 cm and 1.0 cm as a function of the above angle. Note that the velocity profile and the transit times are very uniform with angle which is another indication of the near spherical propagation. These simulations provided confidence that a spherical wave could be produced close to the source by bending the discharge.

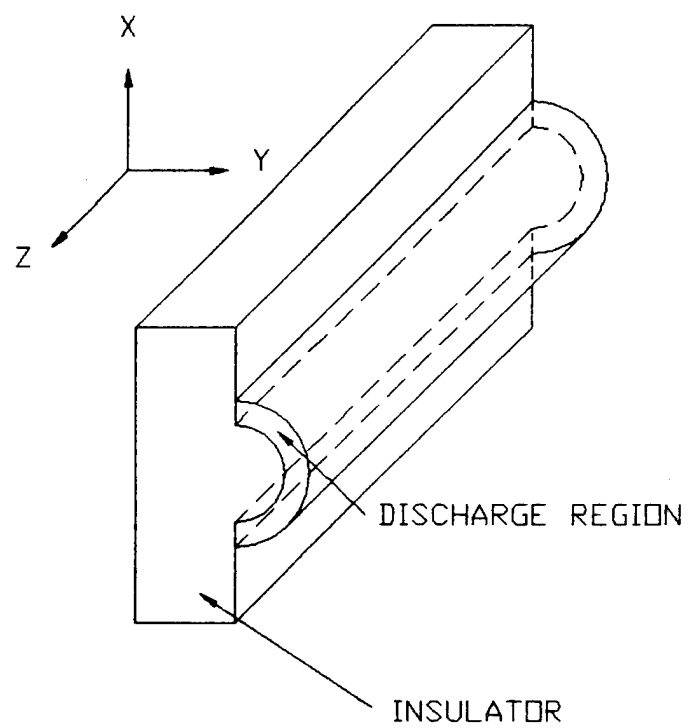


Figure 3-9. SPH 2-D (infinite in z) geometry for curved insulator discharge simulation.

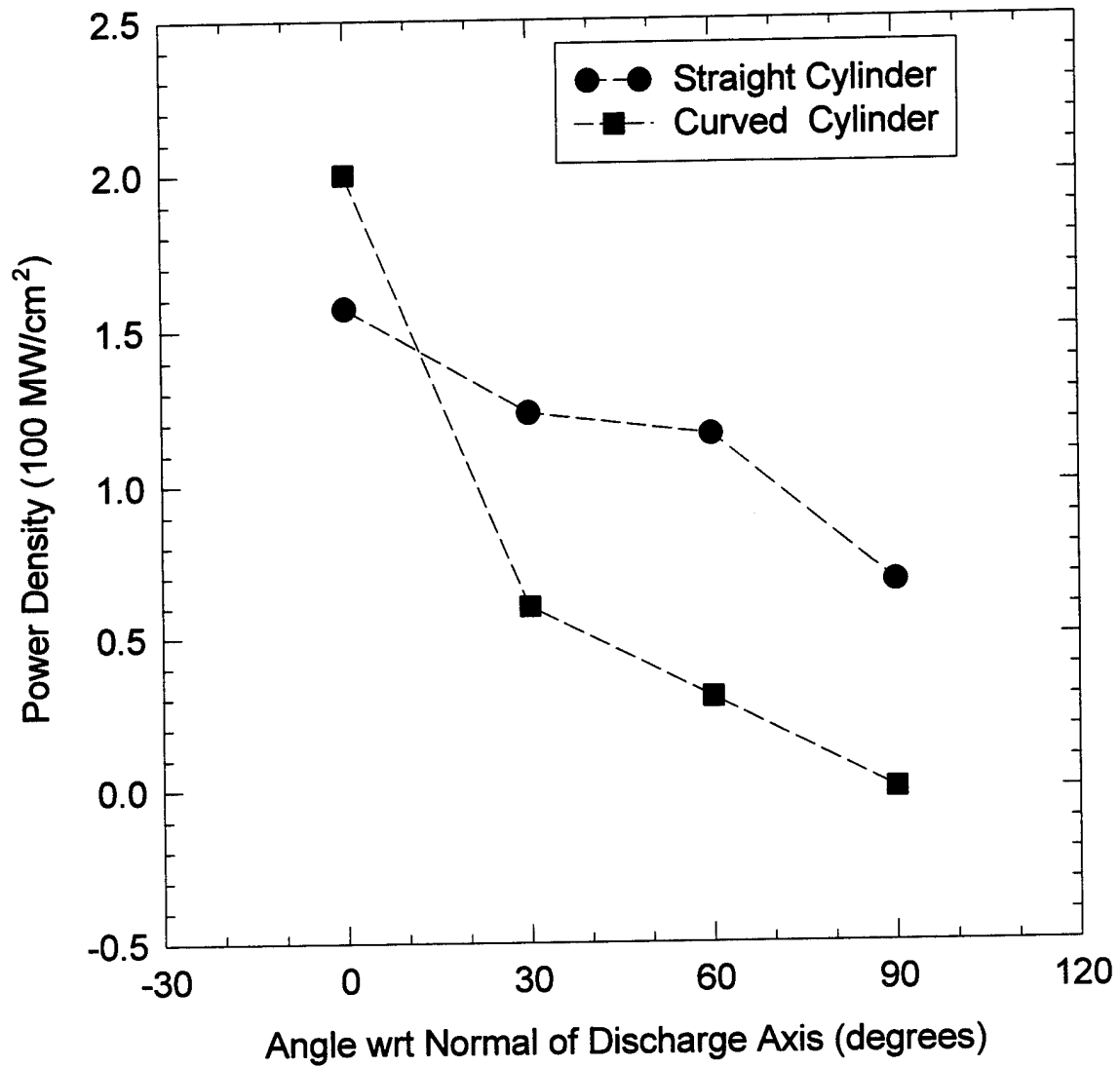


Figure 3-10. Peak mechanical power density vs. angle for straight and curved discharge simulations.

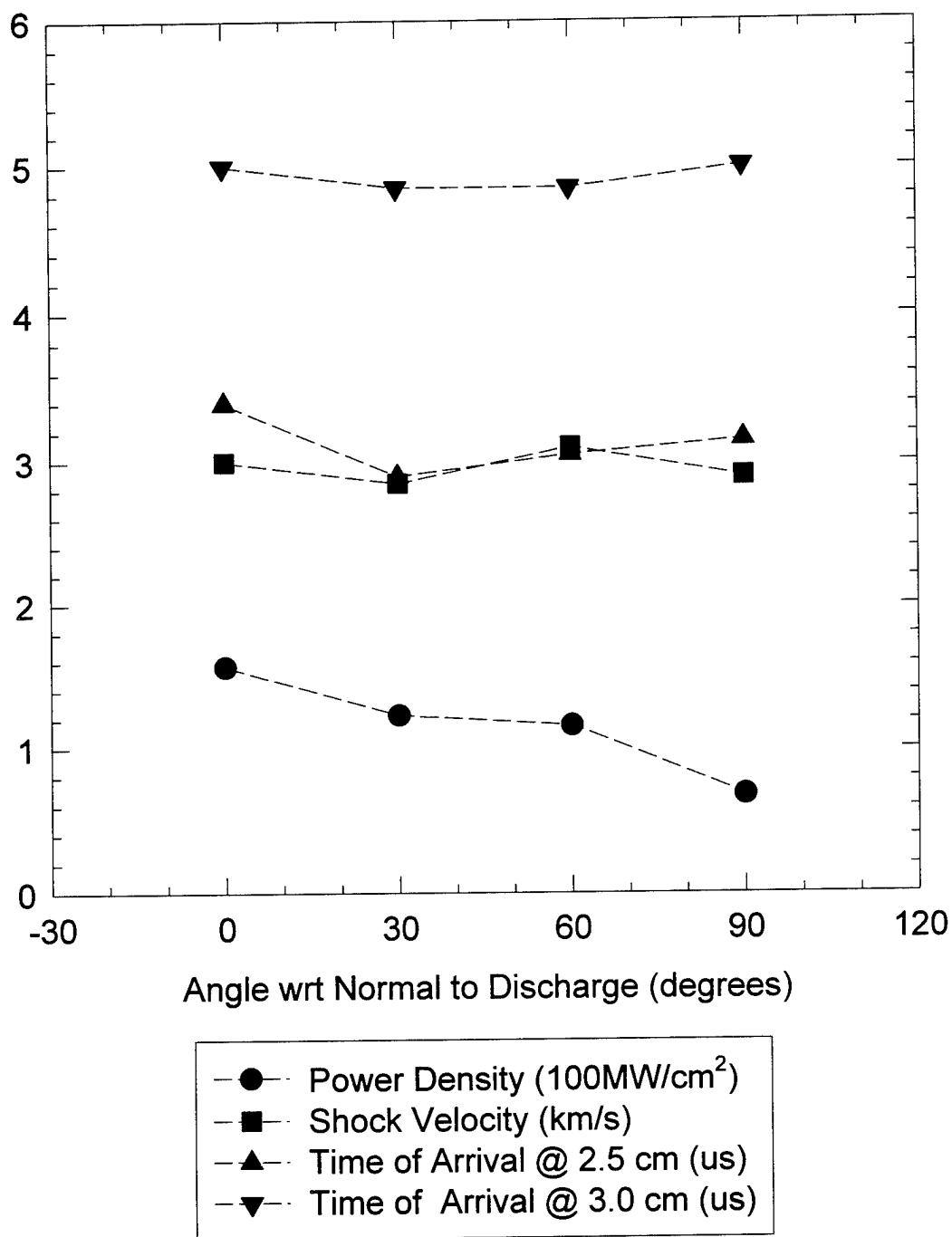


Figure 3-11. Velocity and time of arrival parameters vs. angle for shock produced from curved discharge simulation.

Some of the numerous problems encountered in trying to maintain high resolution at the source as well as simulate a large problem volume were eventually overcome and 3-D simulations on the Cray were initiated. For these runs a 20 kJ discharge 1.5 mm thick by 2.0 mm wide and initial temperature of 49,500 K was initialized along the circumference of a 1.25 cm radius aluminum oxide hemisphere. A 1.0 mm separating layer of cold water was placed on the surface. This put the outer portion of the discharge 2.5 mm and the inner portion 1.0 mm from the insulator surface respectively. Figure 3-12 shows this geometry.

Propagation of the resulting shock wave was examined out to a time of 4 μ s. The simulation terminated here due to a numerical instability 5 mm inside the ceramic near the y axis created by the strong compressive wave.

Figure 3-13 shows the geometry in the x-y plane with the edge of the alumina identified and the locations of the probes both in the alumina and the water approximately at $z = 1.5$ mm. Two probes were inside the insulator 2.89 mm and 5.85 mm from the surface. Three probes were in the water approximately at 2.24 mm, 5.16 mm and 7.13 mm above the surface of the insulator.

The peak pressures in the wave at the five probes and their distances from the origin of the problem are plotted in Figure 3-14. A line is also plotted to show the alumina surface relative to the origin. Note the peak pressure in the water 2.5 mm from the edge of the original plasma boundary is 11.1 GPa. This peak rapidly decays to about 3 GPa at 7.5 mm from the boundary. The first probe inside the alumina is about the same distance from the original plasma boundary (2.89 mm) as the first probe reached in the water, yet the peak pressure is nearly half that in the water. This shows that the reflector has been effective in reducing transmission of the shock. The pressure in the alumina also decays more slowly with range than that in the water because the discharge shape is tending to focus the shock toward the origin.

Figure 3-15 plots the average velocity of the shock from the initial plasma boundary to the probes based on their distance from the boundary and the transit time from t_0 to the time of

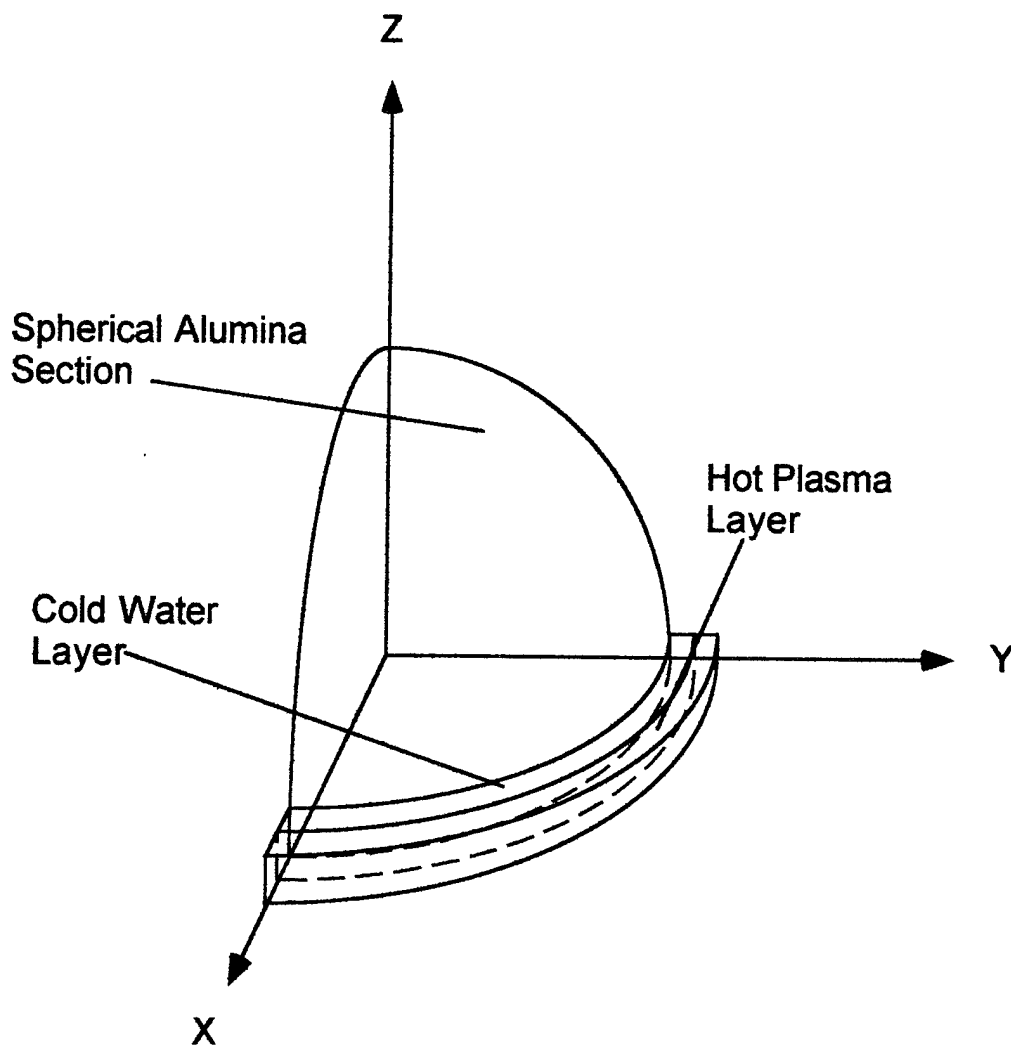


Figure 3-12. 3-D geometry for SPH simulation of hemispherical alumina insulator and 20 kJ discharge to model expected configuration for Phase II experiment.

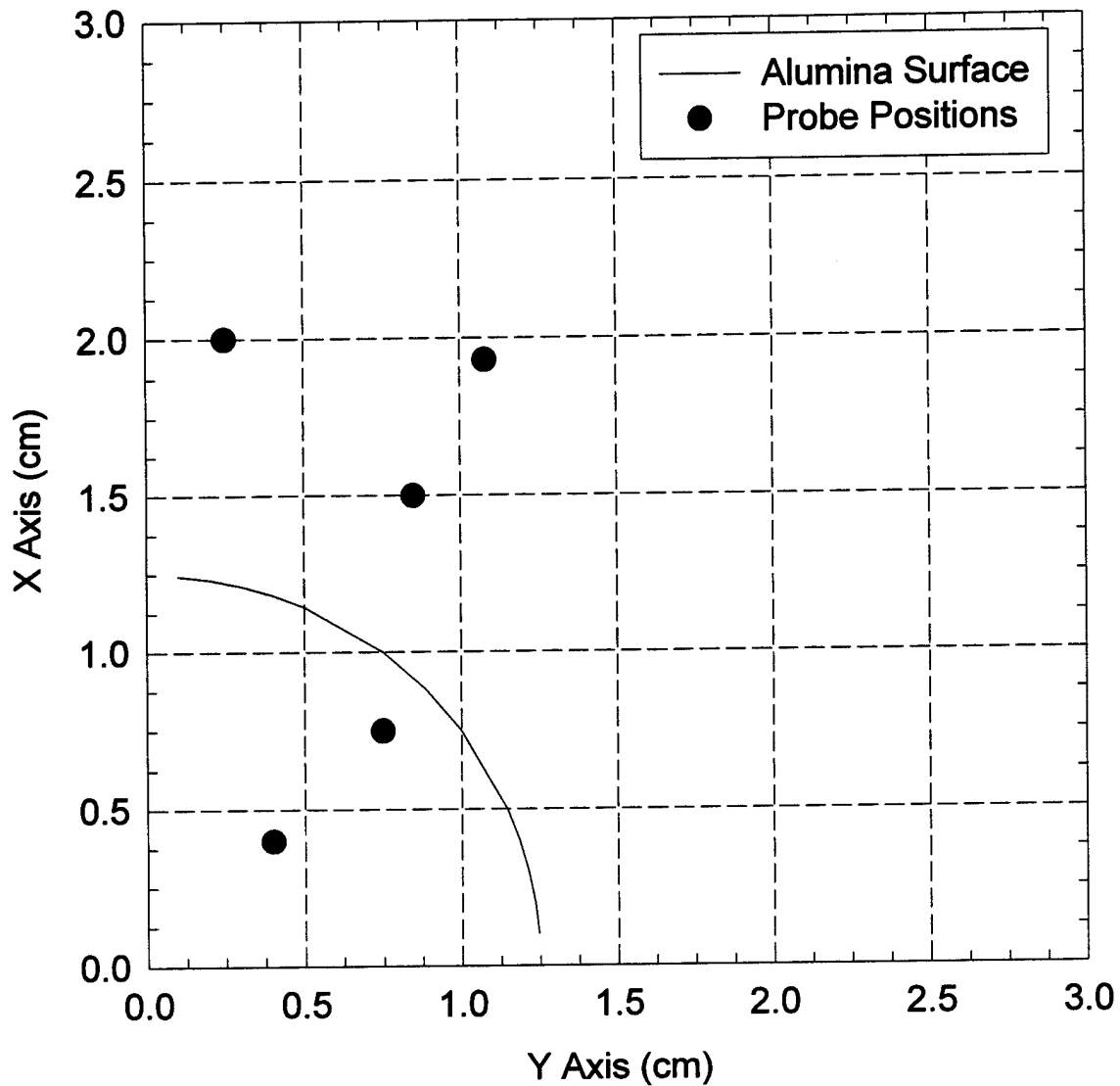


Figure 3-13. SPH geometry for the hemispherical insulator in the x-y plane (approximately at $z = 1.5$ mm) with the edge of the alumina identified and the locations of the probes both in the alumina and the water

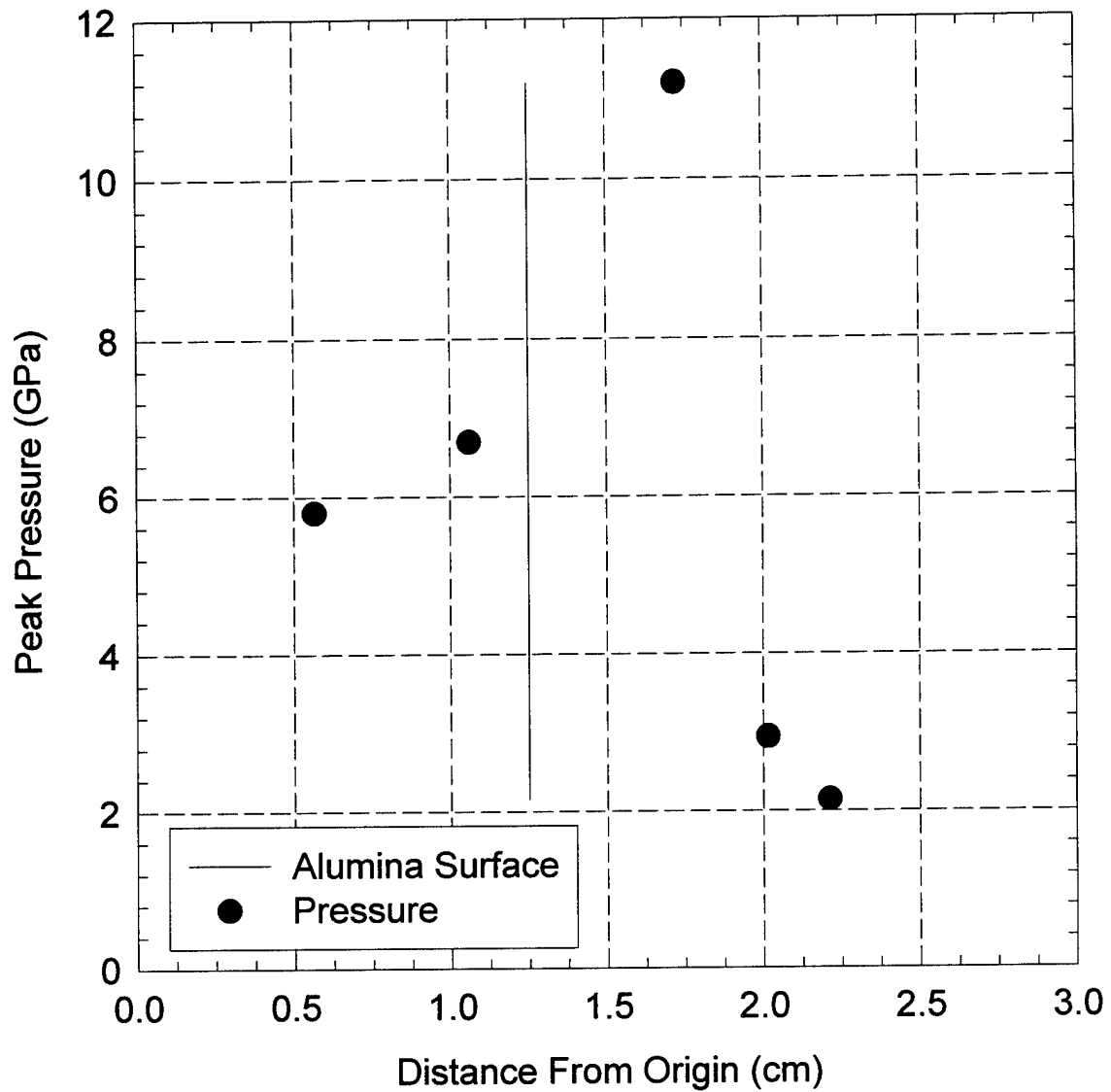


Figure 3-14. SPH results from 3-D simulation showing the peak pressures in the wave at the five probes and their distances from the origin of the problem. A line is also plotted to show the alumina surface relative to the origin.

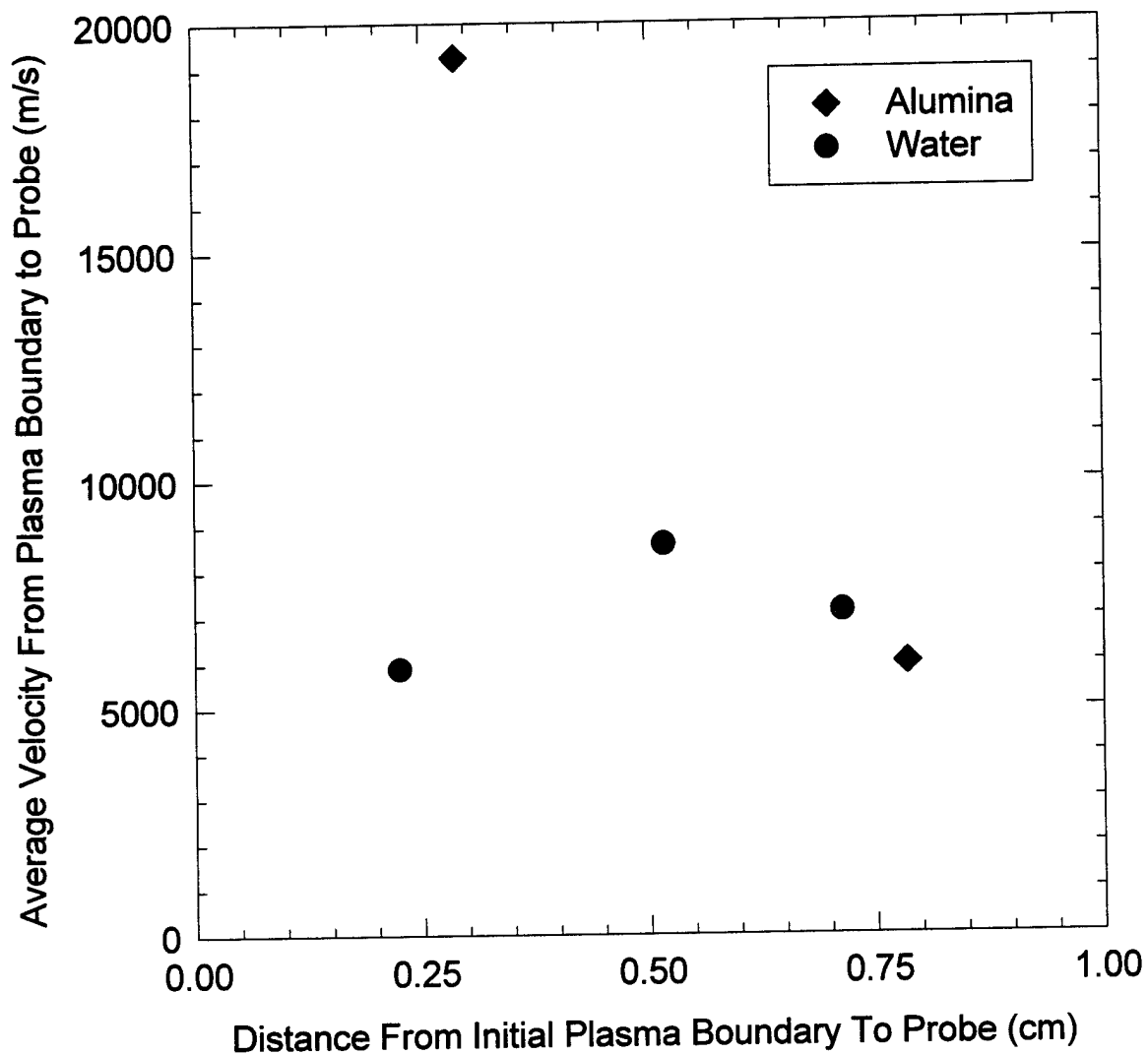


Figure 3-15. Plot of the average velocity of the shock from the initial plasma boundary to the probes based on their distance from the boundary and the transit time from t_0 to the time of arrival of the shock.

arrival of the shock. Immediately inside the ceramic the velocity is over 19,000 m/s or twice the sound speed for this material. Immediately inside the water the velocity is 6000 m/s or four times the sound velocity of water. The apparent initial increase and subsequent decrease in the water shock velocity could be due to a slower formation of the shock in the water versus that in the alumina.

Figure 3-16 shows the time dependent pressure response from the probe located 4.74 mm above the insulator in the water. Note the arrival time of the shock was about 380 ns which gives an average velocity from the plasma of 5895 m/s. Note also the primary shock and the apparent reflected shock from the alumina surface. The reflection must travel 3.5 mm in order to return to the origin of the initial outer plasma boundary. At the above velocity this would result in a 593 ns separation between the primary and reflected pulses. From the figure it is clear that the peaks are about 600 ns apart which confirms the reflection phenomena.

Figure 3-17 shows the response from the probe located 7.5 mm above the surface also in the plane of the discharge. Note how the reflected shock has overtaken the primary and only the internal reflection perturbation is visible. The energy density in the pulse, at this point, can be estimated by taking half the basewidth times the height and multiplying it times the peak mechanical power density which gives 202 J/cm². (See Eq. 3.6).

Figures 3-18 and 3-19 show slices of the problem volume in the x-y and y-z planes respectively. The profile is obviously spherical in the x-y plane. In the other plane, though, the profile is more cylindrical. Note, however, that a surface wave is propagating along the ceramic tending to increase the pressure in the y direction. This trend will likely result in the y-z profile becoming more spherical after additional propagation. At this point in time it is sufficient to assume the overall wave shape is that of two-thirds of a cylindrical tube with a 1.0 cm radius of curvature and 7.85 cm length. This is an area of 33 cm². The ends would add 4.2 cm². Therefore, there is at least 7.5 kJ of energy in the outward propagating wave based on the above energy density.

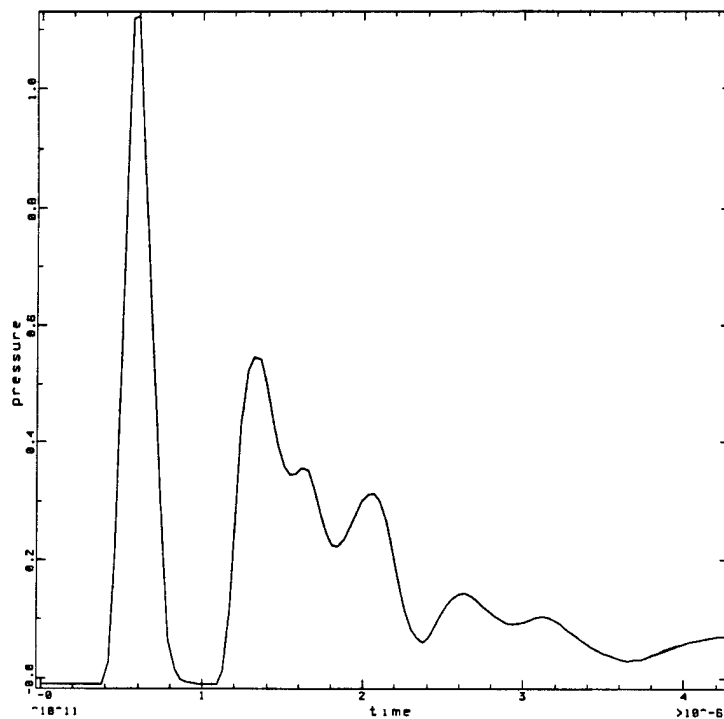


Figure 3-16. Plot of the time dependent pressure response from the probe located 4.74 mm above the insulator in the water. Note the arrival time of the shock was about 380 ns which gives an average velocity from the plasma of 5895 m/s. Note also the primary shock and the apparent reflected shock from the alumina surface.

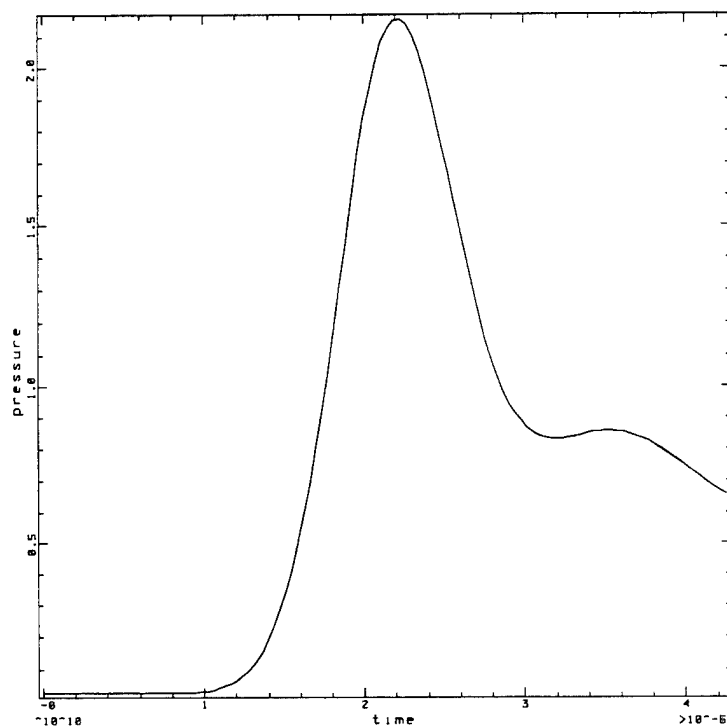


Figure 3-17. Plot of the response from the probe located 7.5 mm above the surface also in the plane of the discharge. Note how the reflected shock has overtaken the primary and only the internal reflection perturbation is visible.



Figure 3-18. SPH pressure field in x-y plan at 3.75 μ s. The vertical axis is x. The discharge occurs in the plane of the page. Note the sphericity of the main shock and the discontinuities in the secondary pulses which may be due to an instability. The pressure is in dynes/cm² so the highest pressure in the shock front is 250 MPa.

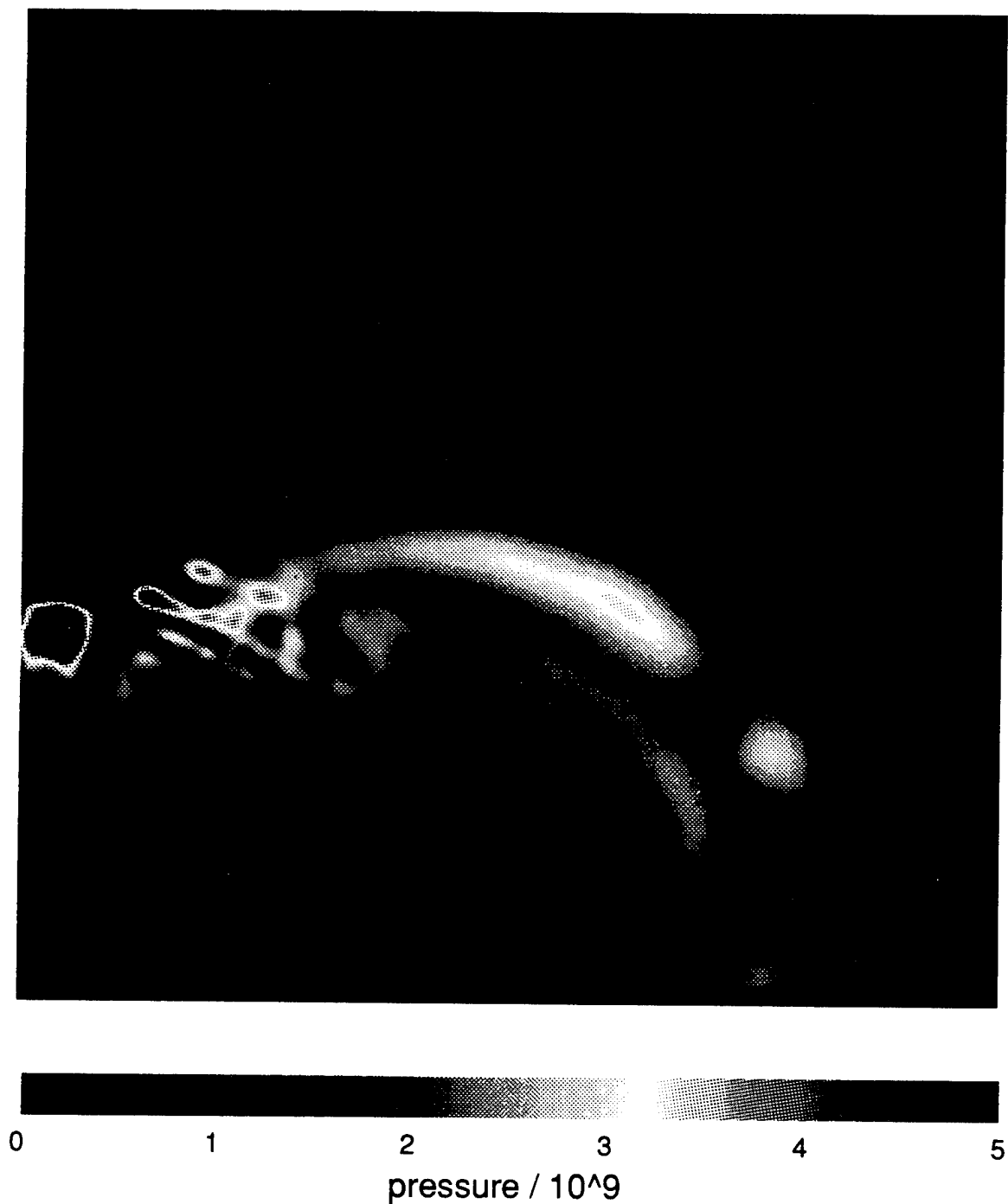


Figure 3-19. SPH pressure field in the y-z plane at 3.75 μ s. The vertical axis is y. The bright red spot inside the Alumina is due to a numerical instability. The discharge was into the page on the horizontal axis. Note the trend of spherical convergence. The pressure is in dynes/cm² so the maximum real pressure is 325 MPa in the portion of the wave moving along the y direction. Along z the maximum pressure is 250 MPa and is coincident with the position of the shock in the x-y plane.

These simulations showed, with an instantaneous energy release at a range of 1.0 cm, that at least 37.5% of the plasma energy could be coupled to the shock. This is less than would be expected from high explosives and may result from high initial internal energy in the plasma. Note that the efficiency for this run was about twice that of the 4 cm free-field simulation. Both simulations had linear energy densities of 5 kJ/cm. The higher efficiency is likely due to the additional shock energy reflected from the Alumina into the main shock.

These simulations support the two hypotheses: the discharge can be shaped to produce a spherical wave with higher effective energy density over a cylindrical discharge and the backward propagating energy can be reflected from a high acoustic impedance surface and added to the main shock from the plasma.

SECTION 4

EXPERIMENTAL RESULTS

4.1 INTRODUCTION.

Many iterations of the pulsed power diagnostic designs were necessary before confidence in their output and mechanical and electrical survivability were obtained simultaneously. It was desired to measure the current and voltage as close to the load as possible for purposes of accuracy.

For the initial electrode design a Rogowski coil was wound, shielded and placed inside the ground, stripline electrode. The response was nonlinear with current and a satisfactory calibration was never obtained. Several voltage divider configurations were also tried initially. One fixed resistor divider failed due to the shock waves in the water. A water divider was found to be unsatisfactory since the surrounding water raised the stray capacitance to ground and degraded the response time. Both of the dividers also had to be capable of absorbing the entire pulse energy if the gap should not breakdown which complicated the design. The final voltage divider design resolved these problems, but had to be located further from the load in the SF₆ gas box that enclosed the capacitor bank output and the stripline.

The electrode design was modified due to a failure of the insulator support for the stripline configuration. The new design incorporated a commercial current viewing resistor (CVR) in the return path to the capacitor bank and a low resistance divider calibrated with a commercial high voltage probe that had a 100 MHz bandwidth. The CVR had a manufacturer's calibrated resistance value of 20 $\mu\Omega$ so it was to provide approximately 10 V for a 500 kA current level. The voltage divider consisted of a 500 Ω water resistor in series with a 5 Ω array of high precision resistors. This divider provided an attenuation of approximately 100.

Early in the checkout it was determined that the CVR was providing signal levels at 50 kV charge voltages that were too high for the estimated impedance. On some shots the integrated power would provide an energy greater than that stored in the capacitor bank.

In the final electrode configuration, it was possible to install a current loop with a known calibration and it was discovered that the CVR reading was a factor of 4 too high. This was later confirmed as a design flaw by the manufacturer. To further confirm this, an additional model of the circuit was analyzed and compared to data taken with the gap shorted out to remove time dependent load effects. The circuit diagram is shown in Figure 4-1. The 2.4 m Ω resistance shown for the load was the resistance measured from the voltage monitor (attached to the output of the mechanical switch) to the bottom of the CVR (attached to the current return of the capacitors). The 20 m Ω resistance is that remaining portion of the circuit resistance chosen to give the best match to the data for the calibration shot and would include the resistance of the capacitors, stripline, and mechanical switch. This value could not be measured statically. The inductance values were chosen based upon those that provided the closest match to the peak voltage observed on the voltage monitor and oscillation period of the waveform. A trustworthy value of this very low inductance could not be obtained with an RLC bridge.

The calibration shot was fired by charging the bank to 2800 volts according to a calibrated high voltage probe. The mechanical switch was fired and the resulting waveforms recorded. The voltage and current loop waveforms for the calibration shot are shown in Figures 4-2 and 4-3. The CVR gave a peak current reading of 88.7 kA while the current loop indicated 22.18 kA. The CVR in this case read exactly 4 times higher than the current loop.

The experimental peak voltage and oscillation period values were within a few percent of those obtained from the simulation described above. The simulation indicated a peak current of 20 kA for the same charge voltage used in the calibration shot which is within 10% of the current obtained by the calibrated current monitor.

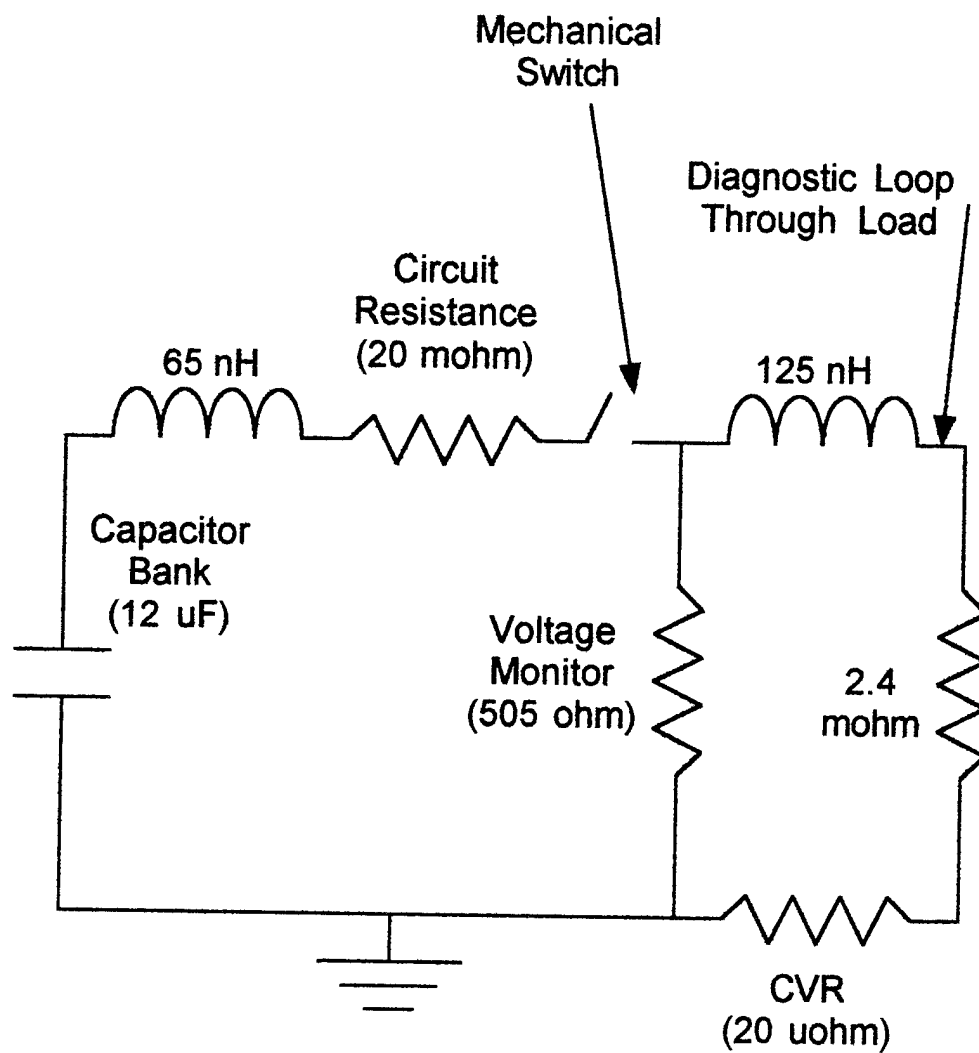


Figure 4-1. Circuit diagram for experiment. Note the load has been shorted and the resistance shown is that for the loop from the voltage monitor through the load.

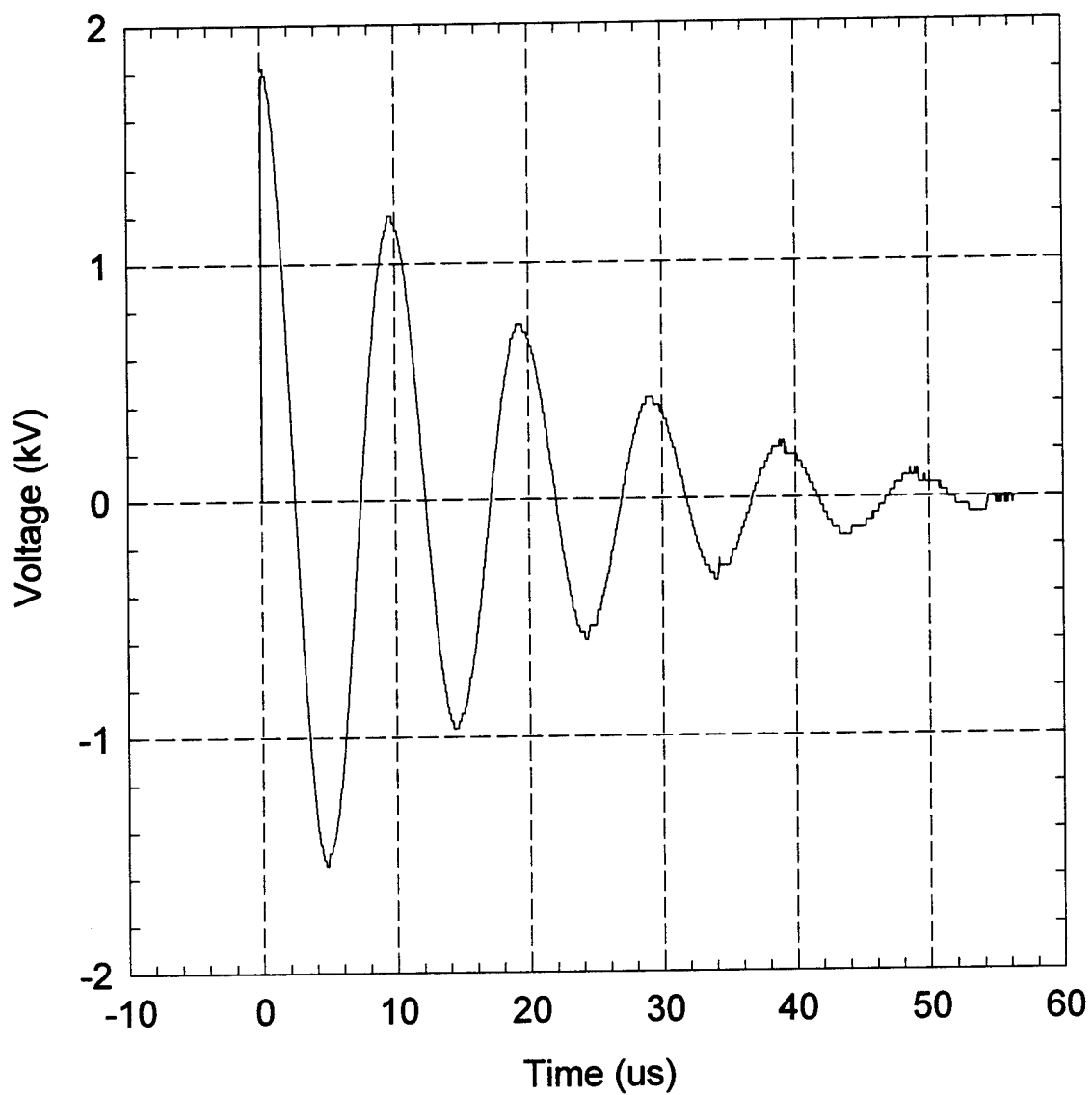


Figure 4-2. Voltage for calibration shot with the load shorted out. The peak voltage was 65% of the charge voltage.

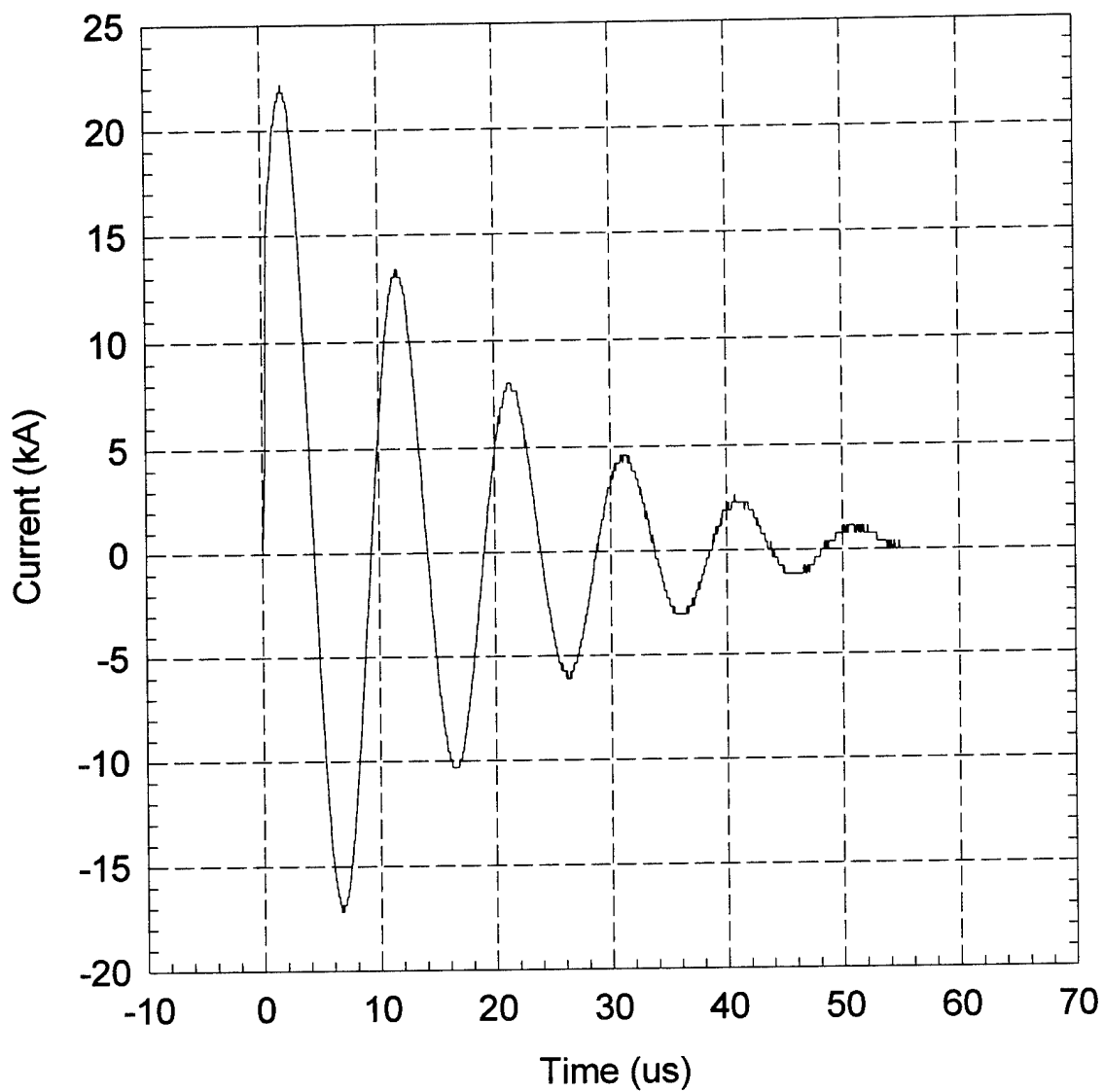


Figure 4-3. Current trace for calibration shot. The peak current was 22 kA or 7.86 times the charge voltage which indicates an impedance of 0.127 Ω .

Apparently, because of the good match of the simulation data to the calibration data, the CVR calibration was indeed off by a factor of 4. Note that the loop impedance of the simulation was $0.126\ \Omega$. The peak voltage should be divided by this value plus 80% of the circuit resistance to obtain the peak current or 0.144. The charge voltage divided by the peak current from the calibration shot gives a value of $0.127\ \Omega$ so there is approximately a 13% difference between the simulation and the experiment which indicates the simulated values are not exact. Continued iteration of these values was not considered useful since the important parameter is the energy calculation and it is unaffected by reactive effects.

4.2 ELECTRICAL PERFORMANCE.

Most of the data were acquired by placing very thin wires between the high voltage electrodes over one inch diameter alumina cylinders of one inch length. This was done in two configurations. A straight wire of length 3.7 cm between the electrodes provided minimum damping. A zig-zag wire of nominally 9 cm length was found to provide near critical damping which gave the highest efficiency.

Figure 4-4 shows the geometry for the ceramic and electrodes. The wires were draped over the ceramic, held with glue, and clamped with the electrodes in a manner that ensured good electrical contact between the wire and the electrode tips. An analysis performed by Ed Martin (Ref. 10) indicated that the wire would have minimum impact on the plasma. The wire diameter was 0.00254 cm (1 mil) and had an estimated resistance of $3\ \Omega$. Based upon quoted vaporization rate constants (Ref. 11) an estimated 3.46 J were required to vaporize this length wire. This occurred so rapidly that it was not expected to affect the circuit response and therefore would not distort the energy deposition profile in the plasma. Use of the wire was necessary because at these long gaps and low voltages the gap would not breakdown reliably. In shots made without the wire, some catastrophic failures of the voltage monitors resulted. The wire guaranteed no delay in breakdown. Without the wire, the breakdown delay could vary from tens to hundreds of microseconds for the same charge voltage.

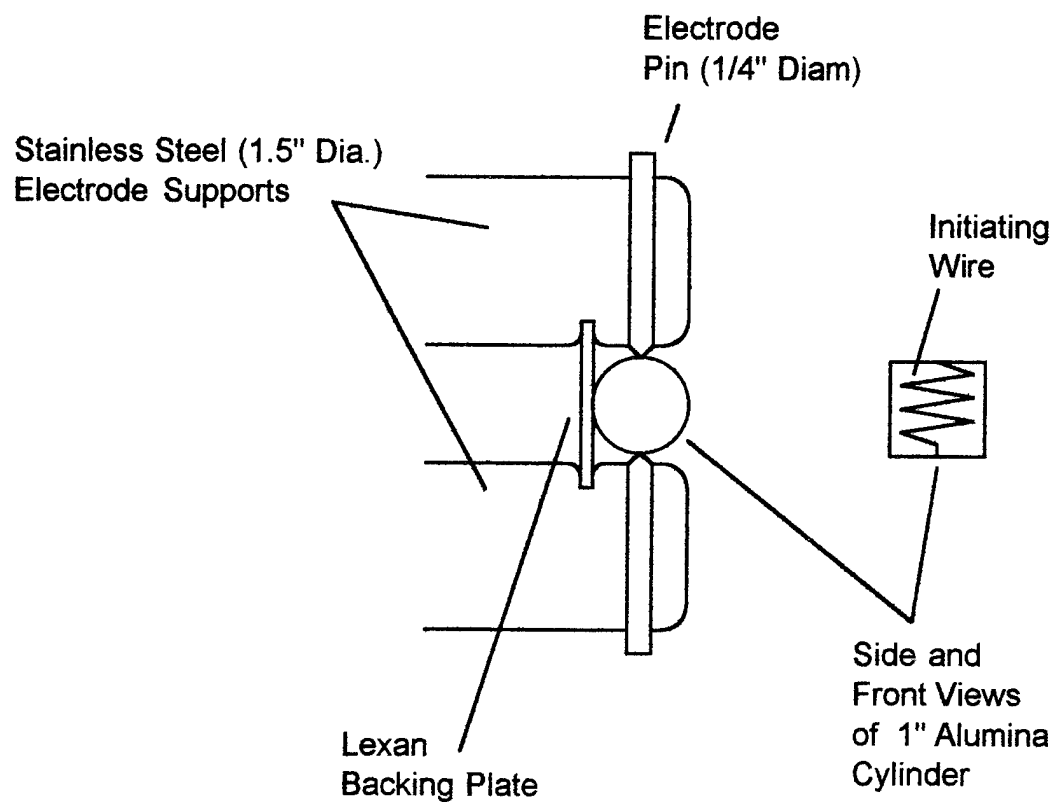


Figure 4-4. Geometry for electrodes and ceramic insulator/reflector that was used to support the initiation wire for the discharge and to form the discharge in a curve for shock wave shaping.

Two typical shots demonstrate the dramatic difference in damping and energy efficiency that resulted from the different discharge lengths are described below. Shot #32 was a 3.7 cm wire draped straight over the ceramic between the two electrodes so the shock would radiate away from the electrode structure into the main body of the tank. For this shot the charge voltage was 44.7 kV which resulted in a stored energy of 12 kJ. Shot #48 was from a 9 cm wire draped in a zig-zag pattern over the ceramic. For this shot the initial voltage was 31.6 kV which resulted in 6 kJ stored.

4.2.1 Underdamped Response.

Figures 4-5 through 4-9 show the voltage, current, power, energy dissipated, and the resistance in the plasma versus time for Shot #32. These data were obtained by removing losses within the diagnostic loop associated with stray resistance other than the plasma and by correcting the voltage for the effects of inductive drops in the discharge loop. Although the inductance has little or no effect on the integrated energy it does affect the peak power as will be shown.

The correction was not complete since the energy integral still indicates some reactive power in the signal. This may be due to the combination of chosen resistance and inductance values that were used to match the calibration.

Since flux is conserved, the direct energy integral contains only the energy dissipated in the circuit between the voltage monitor and ground. This loop beyond the diagnostic has some finite resistance in addition to that of the plasma. The plasma energy was obtained by subtracting the additional losses associated with the loop resistance of 2.4 m Ω . Out of 12 kJ stored only 2108 J were dissipated in the plasma and 490 J were dissipated in the stray resistance of the loop. This is about an 18% transfer efficiency from the bank to the plasma. For all of the straight wire shots tested, a similar underdamped response was obtained. In this case only 22% of the stored energy can be accounted for.

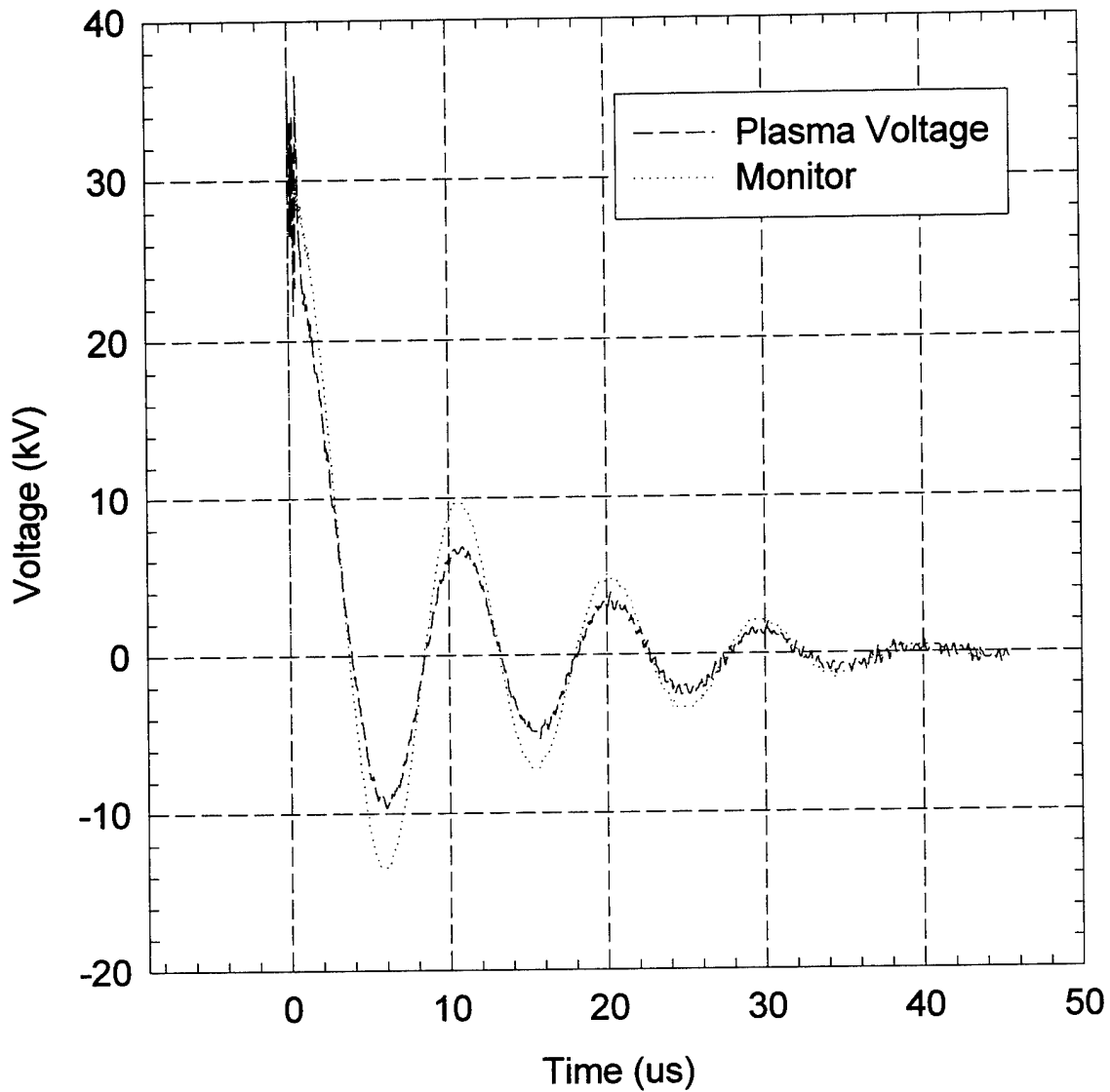


Figure 4-5. Voltage response (with and without the inductive correction) for a 3.7 cm discharge. Note that the underdamped response indicates a very low average plasma resistance.

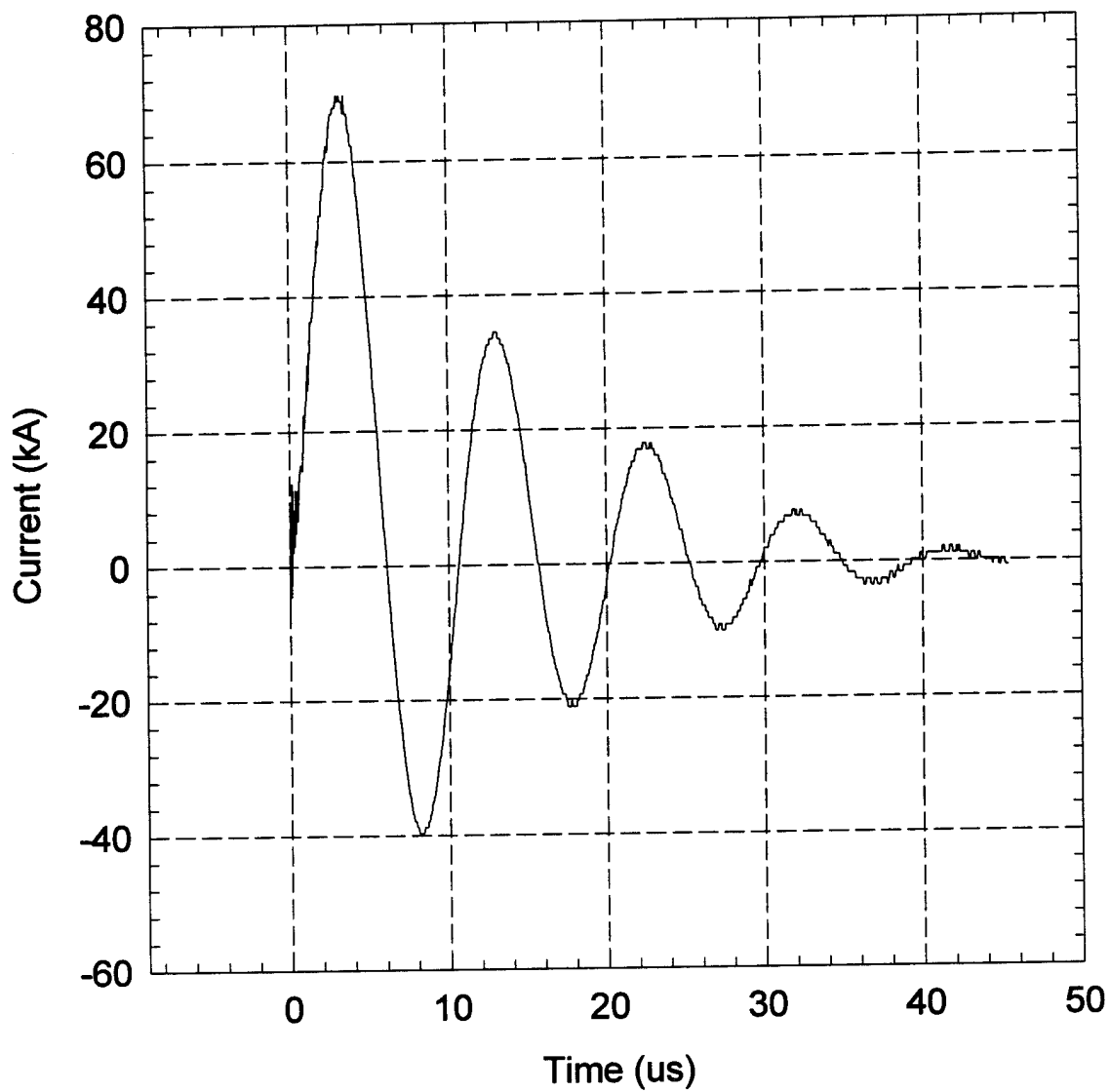


Figure 4-6. Current response for a 3.7 cm discharge.

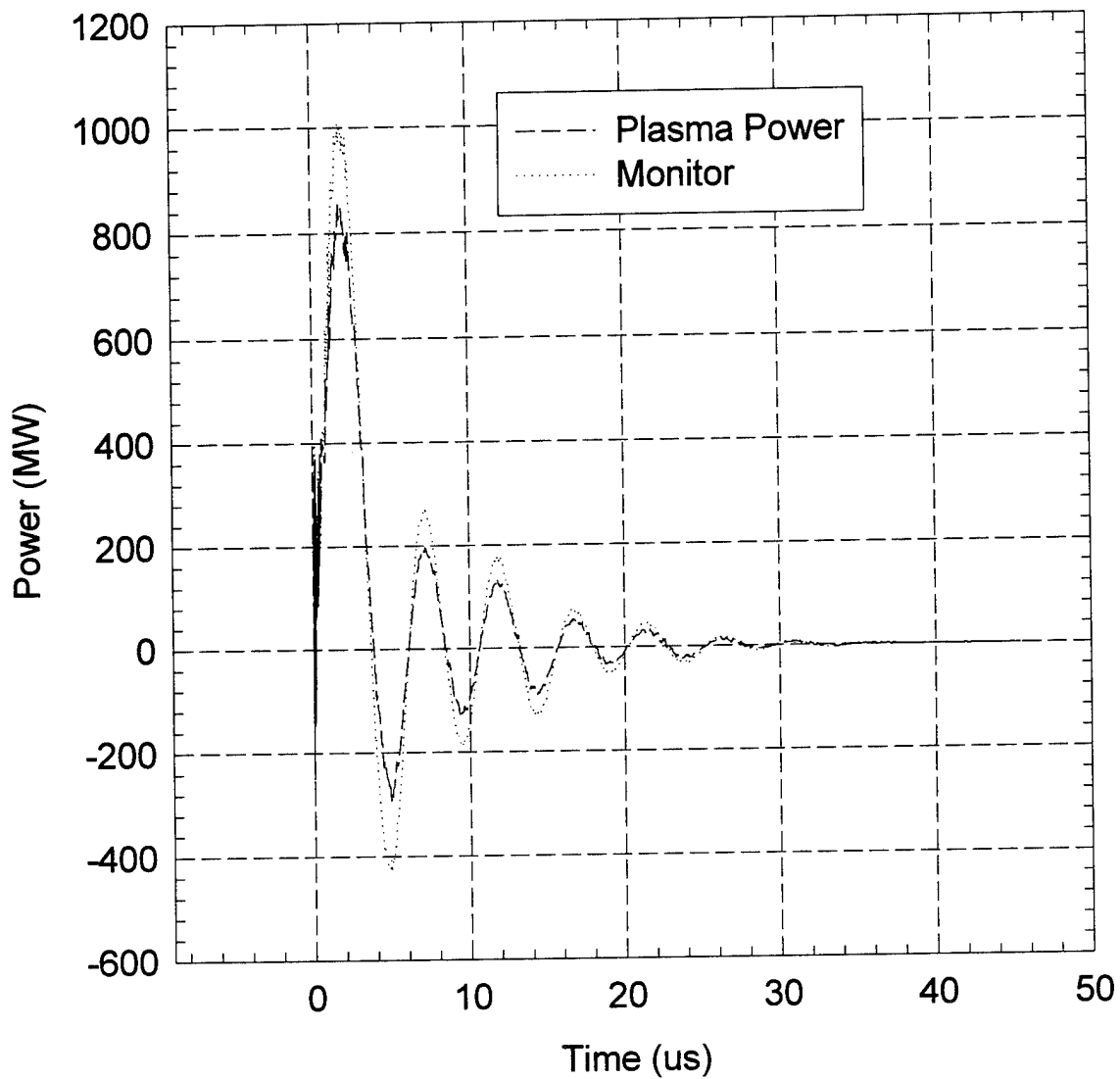


Figure 4-7. Electrical power for a 3.7 cm discharge. The reactive power is evident in the calculation with the uncorrected voltage monitor response.

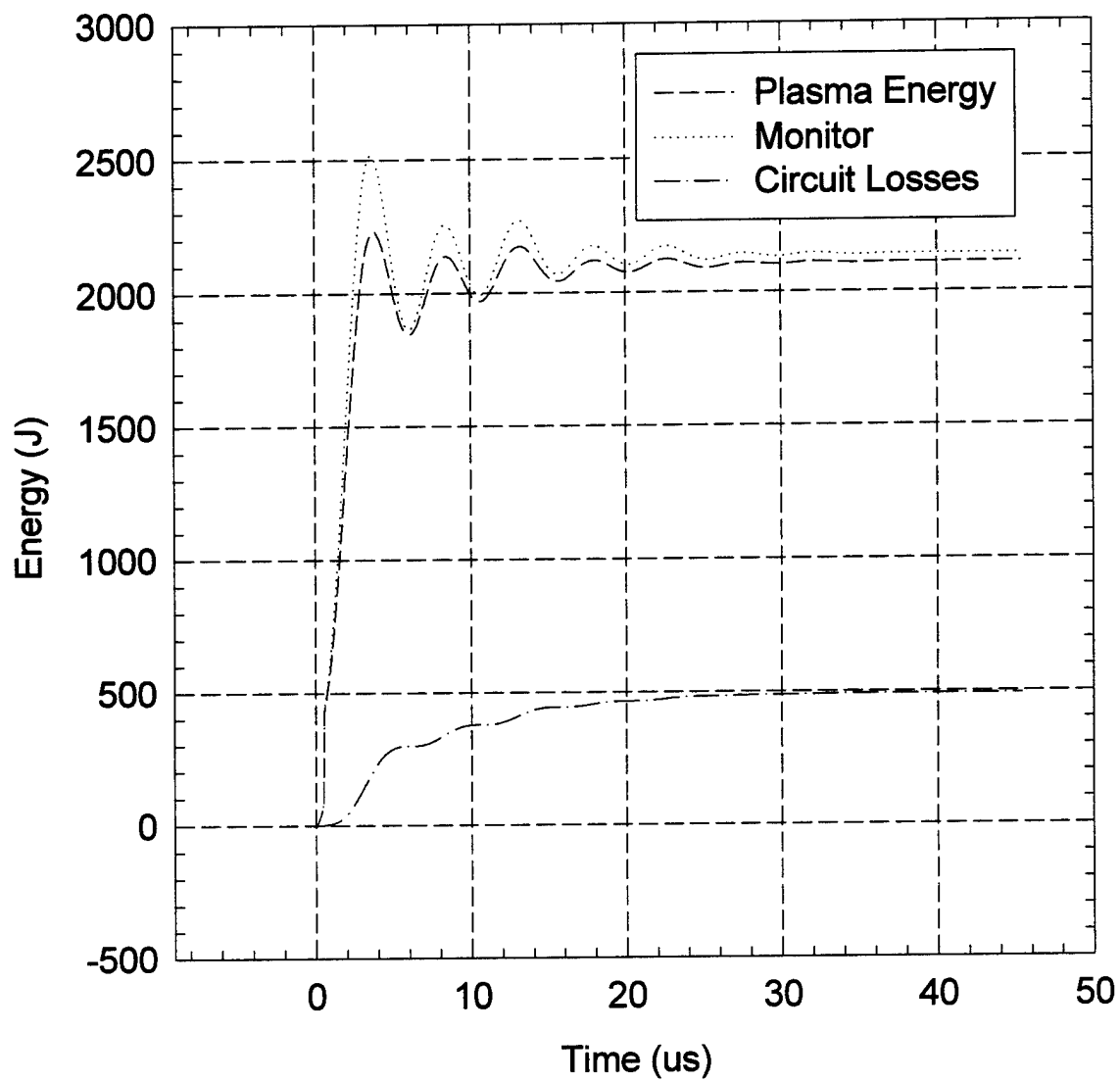


Figure 4-8. Plasma energy for a 3.7 cm discharge. Note how even the inductively corrected data overshoots and oscillates about the final value due to the reactive power in the circuit. The 10-90% energy delivery time was 2.2 μ s.

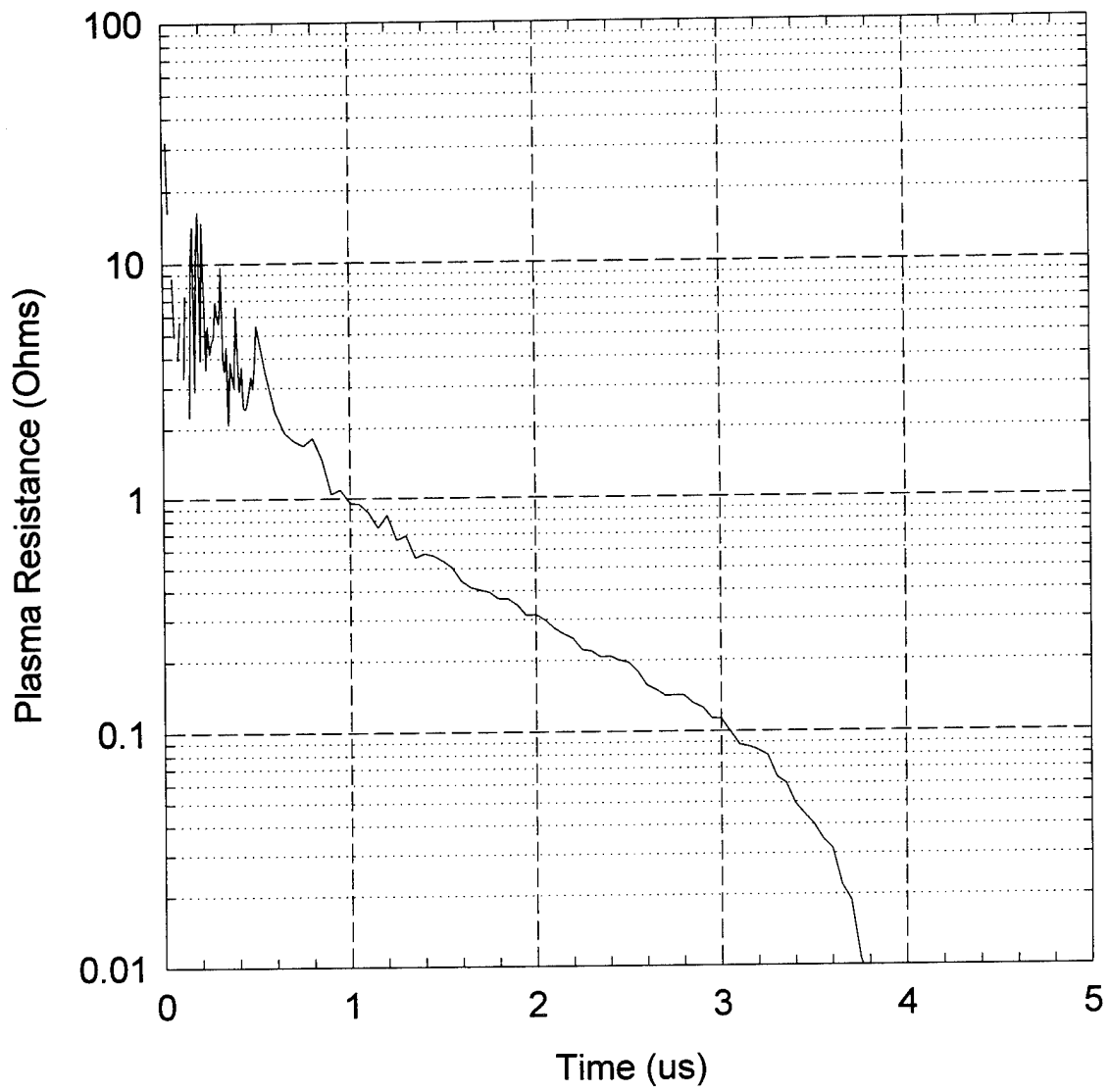


Figure 4-9. Plasma resistance for a 3.7 cm shot. Note that the resistance falls three decades in 3.8 μ s.

The ceramic surface was always burned more around the immediate vicinity of the electrodes as if the discharge tended to bunch in this region. Also stainless steel was visibly plated onto the ceramic where the surface was blackened from the discharge. The rest of the discharge path typically grew to a width of 6-10 mm which indicates that the plasma column grew to a significant size.

4.2.2 Overdamped Response.

In Figures 4-10 through 4-14 the same parameters are shown for a 9 cm discharge (Shot #48). The initial condition for this shot was 31.6 kV and 6 kJ were stored which was exactly half that of the straight 3.7 cm wire shot. In this case the wire was laid out on the ceramic in a zig-zag pattern so that the entire length was contained within the same 3.7 cm portion of the 8 cm circumference of the cylinder. A new piece of ceramic was used for this shot however.

In all cases, whether the wire was straight or a pattern was used, the discharge always followed the original position of the wire as evidenced by the burn marks on the alumina surface. In this case the discharge path only grew to about 3 mm and left a more visible greenish residue which was likely oxidized copper from the wire.

The data were processed for the direct readings from the current and voltage monitors and with the voltage corrected for inductive effects in the diagnostic loop as before. Note in the voltage (Figure 4-10) that the inductive correction results in a faster decay in the voltage from the peak and removes the negative excursion. This is more consistent with the current response.

In Figure 4-11, the current appears to persist long after the voltage has fallen to a level equivalent to the digitizer noise. Negligible power beyond 8 or 9 μ s is observed to contribute no further increase in energy dissipated by the plasma as shown in Figures 4-12 and 4-13. The inductive correction has a substantial impact on the peak power observed in the plasma versus the direct reading, but as indicated, there is virtually no difference (11 J out of 4308 J)

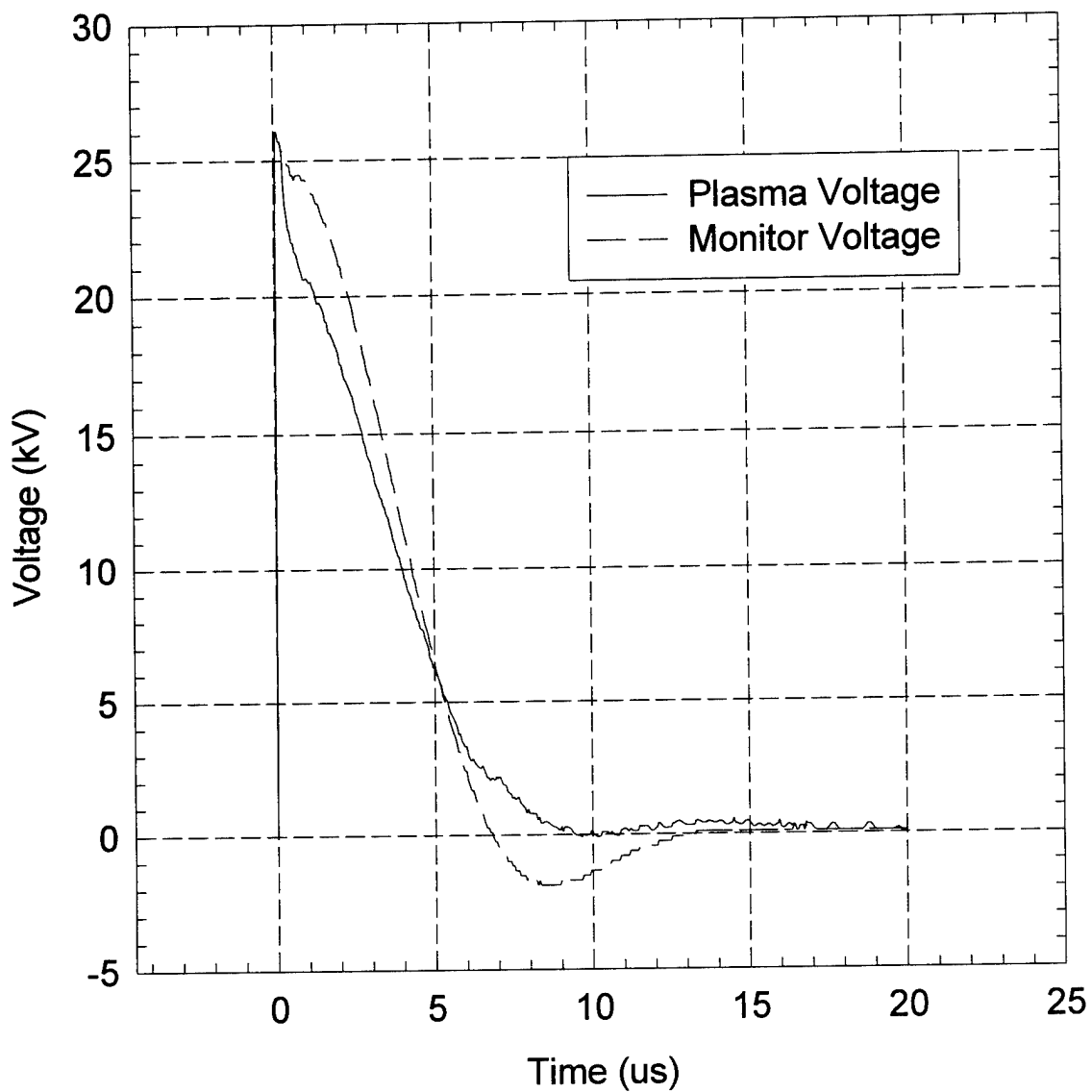


Figure 4-10. Voltage response for a 9 cm discharge. Note that the response is highly damped indicating a much higher average plasma resistance for the longer discharge path. Also the inductive correction shows a fully damped response.

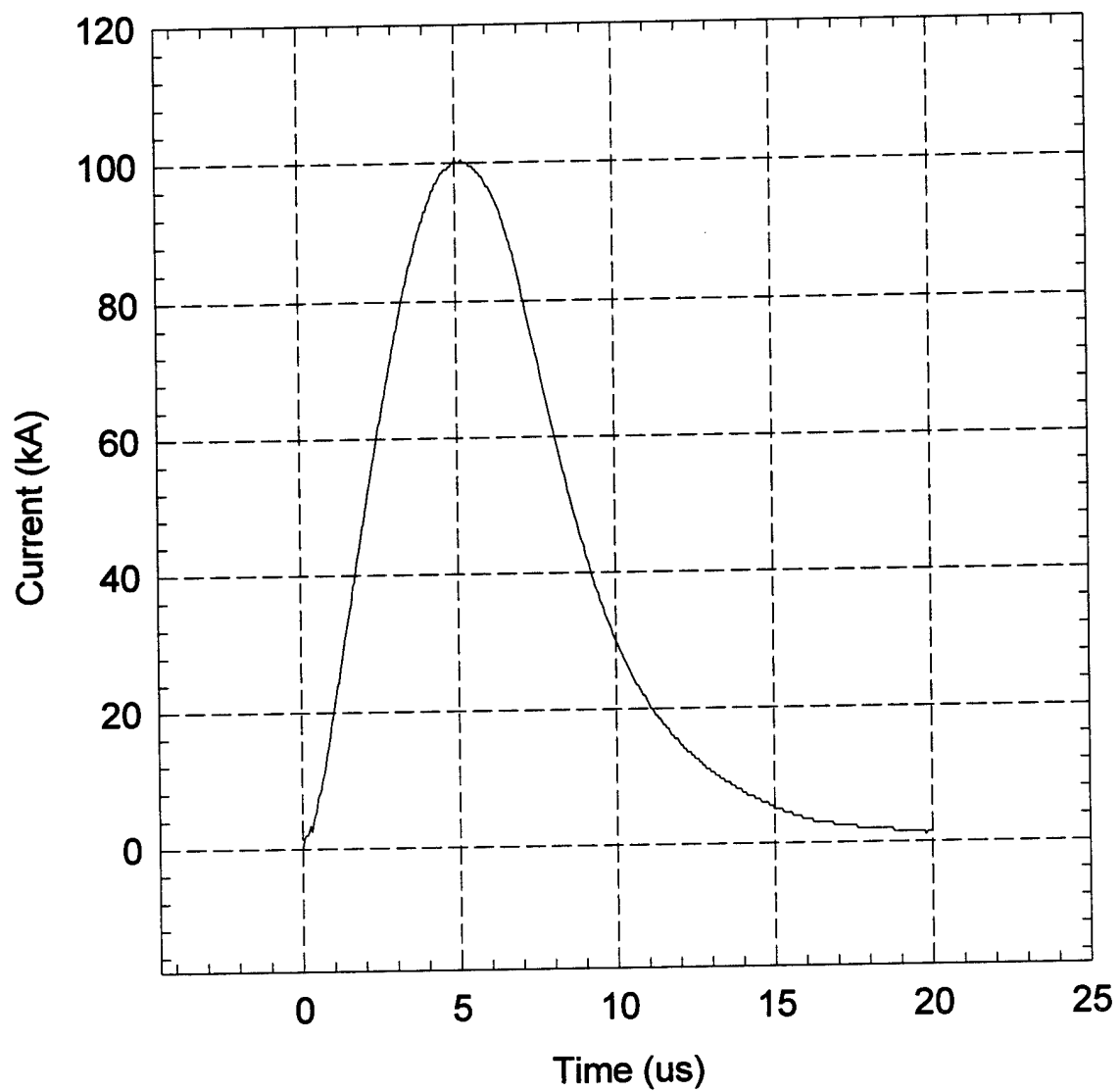


Figure 4-11. Current response for a 9 cm discharge.

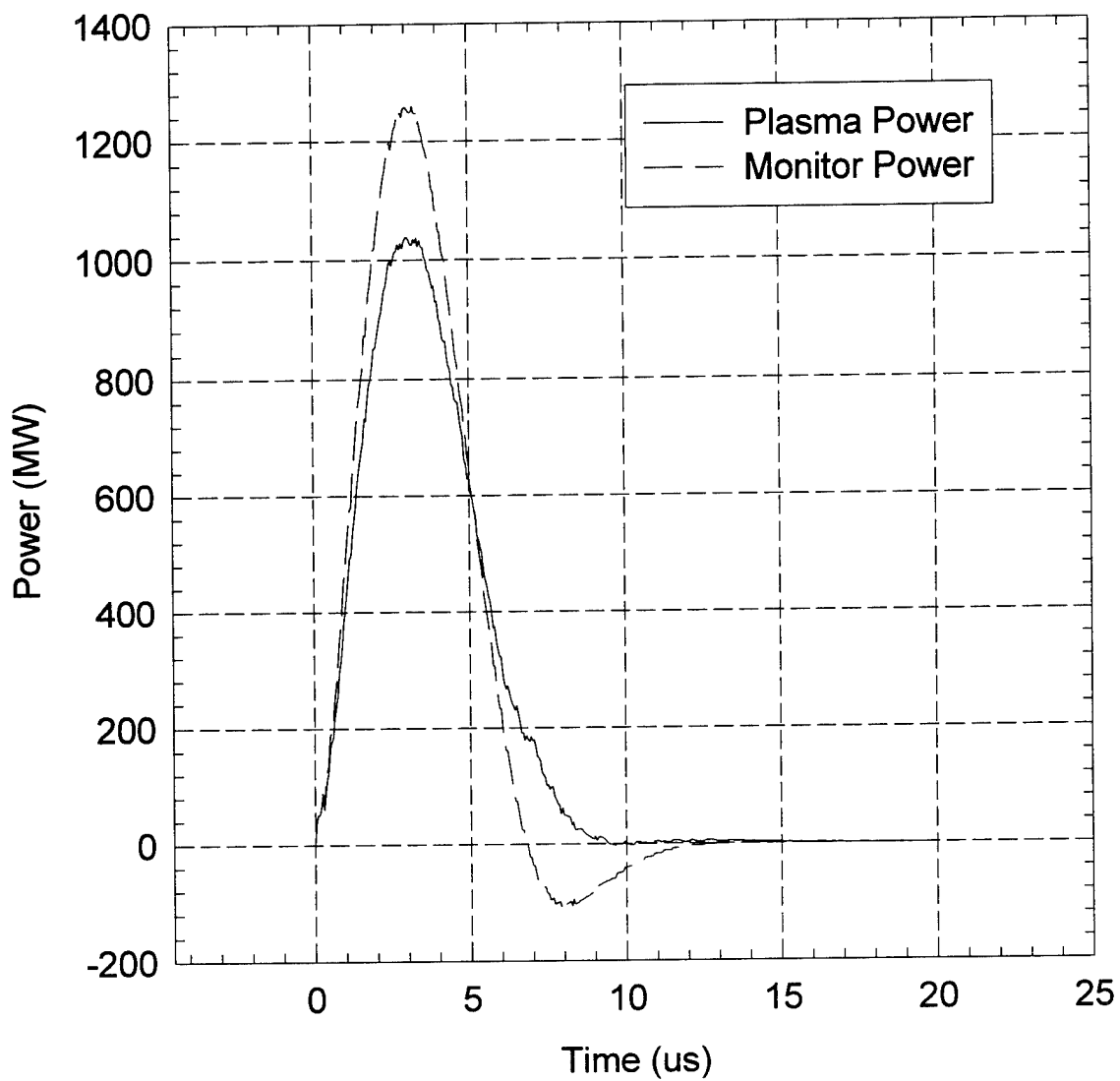


Figure 4-12. Electrical power for a 9 cm discharge. Note that the inductive correction makes almost a 20% difference in the peak power.

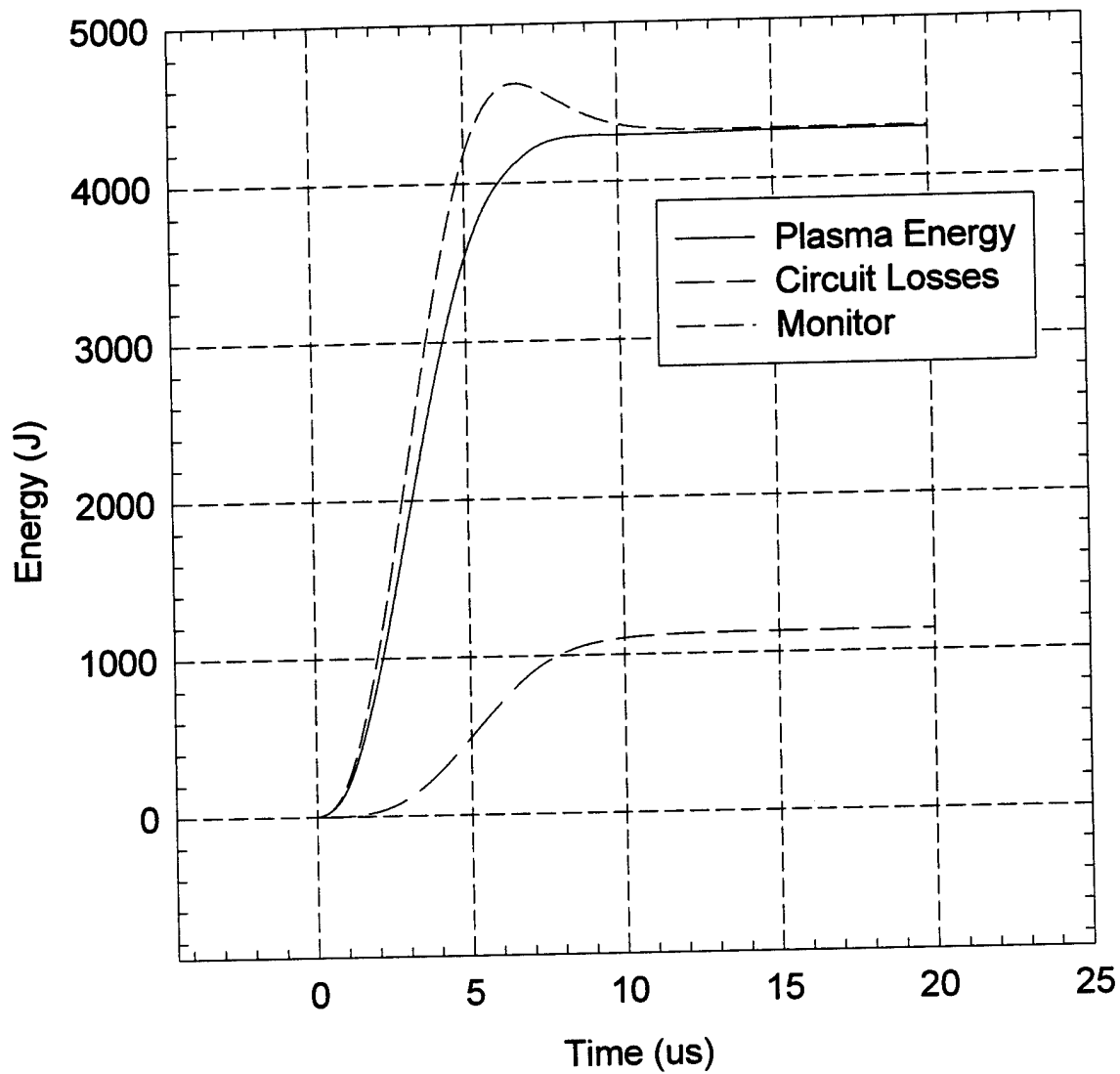


Figure 4-13. Plasma energy for a 9 cm discharge. Note that the inductive correction completely removes the overshoot in the energy integral. Also the 10-90% energy delivery time is 4.2 μ s.

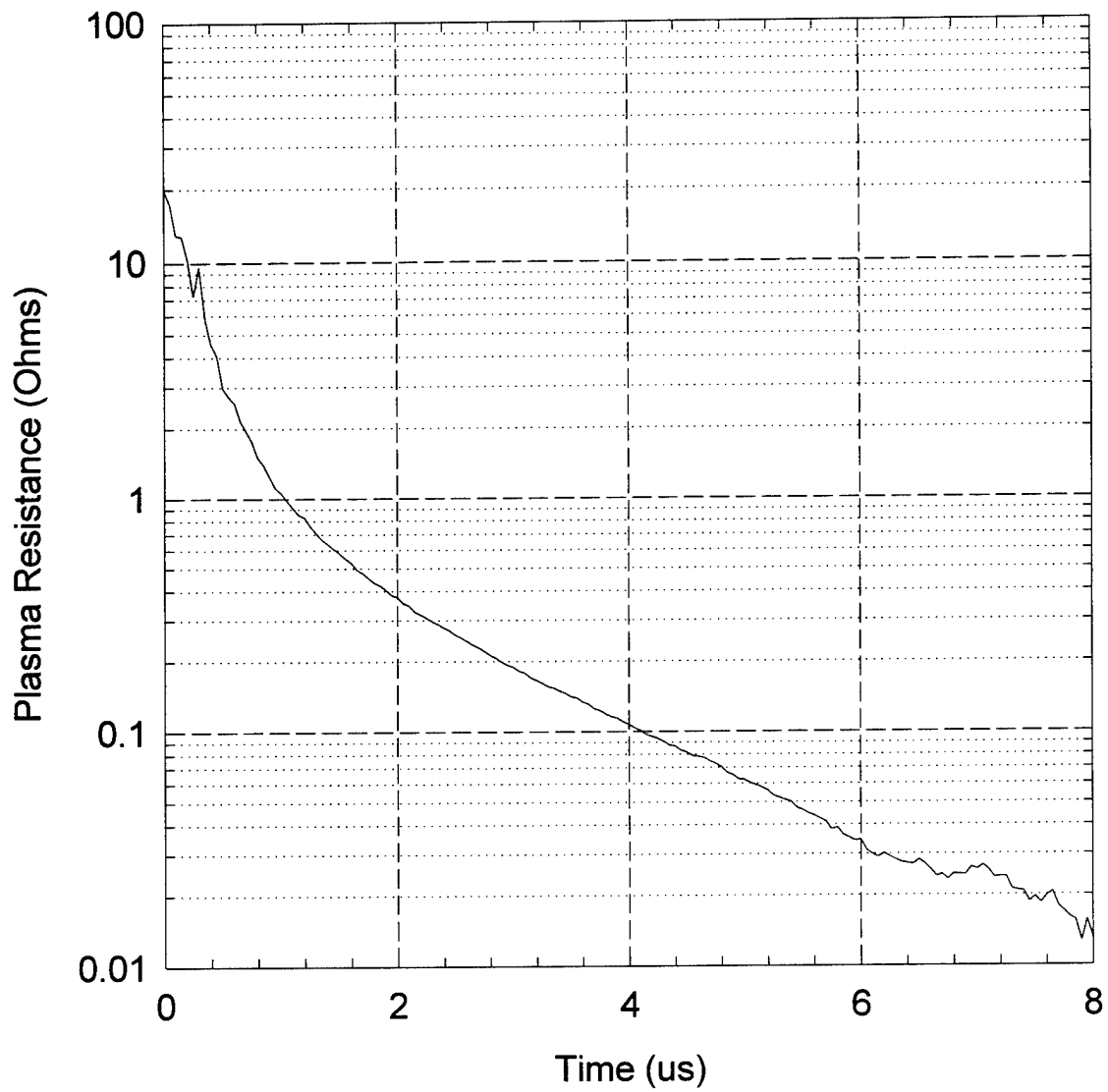


Figure 4-14. Plasma resistance for a 9 cm shot. Note that the resistance takes 8 μ s to fall three decades.

in the energy ultimately dissipated between the corrected and uncorrected calculations. In this case however the 10-90% energy delivery time is 4.2 μ s or nearly twice that of the 3.7 cm shot.

For this shot the plasma energy was 4.3 kJ while the losses due to the stray resistance of the loop were 100 J. If the 20 m Ω resistance assumed for the rest of the circuit is used to calculate other circuit losses the total circuit loss becomes 1132 J. This is a 72% transfer efficiency with 91% of the stored energy accounted for. This 9% discrepancy may be due to an inaccurate estimate of the total circuit resistance or other unaccounted for losses. The efficiency was four times greater for the longer discharge. This is the result of a larger average plasma resistance during the discharge.

Note that based upon the burn marks, the channel diameter was approximately one half that of the straight wire and the length was about 2.5 times greater. For the same plasma resistivity the total resistance should have been about 10 times greater. Comparing Figure 4-9 to Figure 4-14 shows that the 9 cm shot still had a resistance of 100 m Ω as long as 4 μ s into the discharge while the 3.7 cm shot had fallen to 10 m Ω at the same point in time which is consistent with the geometry argument. The peak current on this shot was 100.5 kA compared to 70 kA on the underdamped shot which had a greater charge voltage, but higher frequency due to the lower resistance.

Note that since the resistance fell much more slowly for the long discharge, it took twice as long to load 90% of the plasma energy. Even though the two shots had totally different responses and initial conditions, each loaded about 2 kJ in 3 μ s. Shot #32 had an electrical efficiency of only 15.2% compared to 72% for Shot #48.

4.3 SHOCK PERFORMANCE.

Pressure data were typically taken with 1/16" diameter calibrated Tourmaline gauges that provided a signal level of 0.5 mV/psi. PVDF gauges were also used and usually had a peak reading 30% higher than the tourmaline but the late time response often could not be

trusted. The PVDF gauges had a response time of better than 200 ns while the tourmaline gauges were limited to 1.5 μ s response time. Because the PVDF gauges are a differential reading gauge, after integration the signal would often fail to return to zero. This made energy calculations impossible. Therefore all energy calculations and efficiency estimates were made with the Tourmaline responses and should be considered conservative in the extreme. This is even more the case because of the way the data were reduced. Multiple reflections often occurred at different times in the pulse with gauges in similar positions. Thus the data were reduced by calculating the energy in the pressure pulse up to the first zero crossing. This was felt to be the most prudent way to view the data since the primary shock is of greatest interest; however it is conservative since some apparent reflections occur so closely behind the main shock that they could not be due to structure or wall reflections. All of the data presented here were for a range of 45 cm unless otherwise noted. Additionally only pressure data for probes directly in line with the discharge (zero degrees from the axis normal to the ceramic in both planes) were compiled.

Figures 4-15 and 4-16 show the time dependent pressure response for Shots 32 and 48 at a range of 45 cm (18"). The probe positions were within 1" of each other in the horizontal plane at the same depth as the center of the wire. Note that both pulses show a rarefaction wave that clips the main shock within 10-15 μ s of arrival of the shock. If this were the result of a free surface reflection the surface would have to be only 1 cm from the shock origination point. In the experiment the nearest free surface was the tank back wall which was at least 20 cm from the discharge. The earliest rarefaction should not occur until over 250 μ s after arrival of the primary shock. Since the ceramic has a sound speed of 9600 m/s, a 1" scale length would produce a relief wave after about 5.3 μ s which is more consistent with the observed behavior. In this case the energy associated with the oscillation could be legitimately included in the efficiency, but the response is not that desired for simulation purposes. Such a rarefaction however should not last for more than a few microseconds which is not the case in Figure 4-16.

In Figure 4-17 both shots are expanded on the same time scale to show the first zero crossing. Note also that they both have characteristic oscillations at the peak of nominally

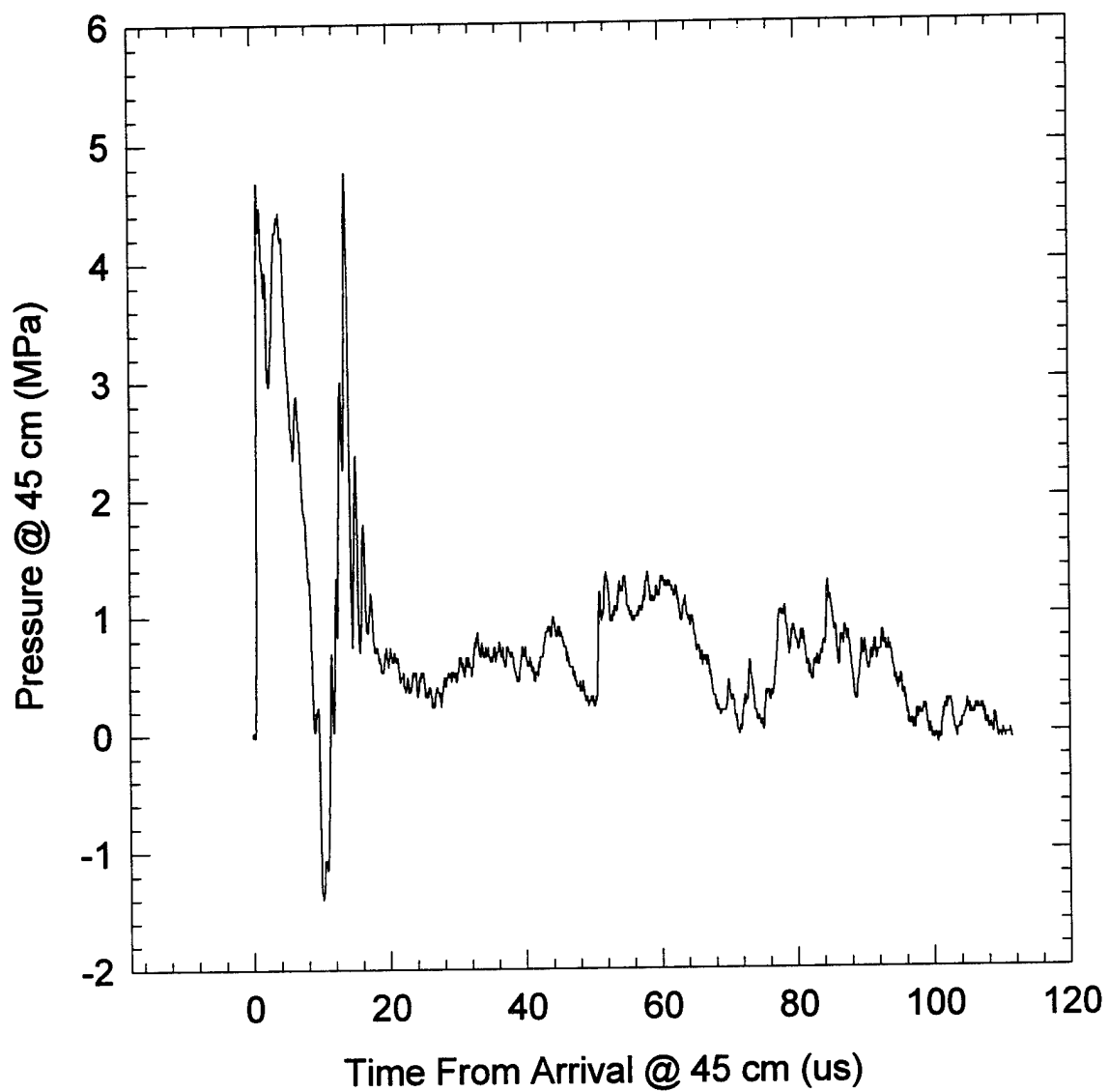


Figure 4-15. Tourmaline gauge pressure reading at 45 cm for Shot #32. Note the strong rarefaction that appears to clip the pulse and the long duration responses out to 100 us.

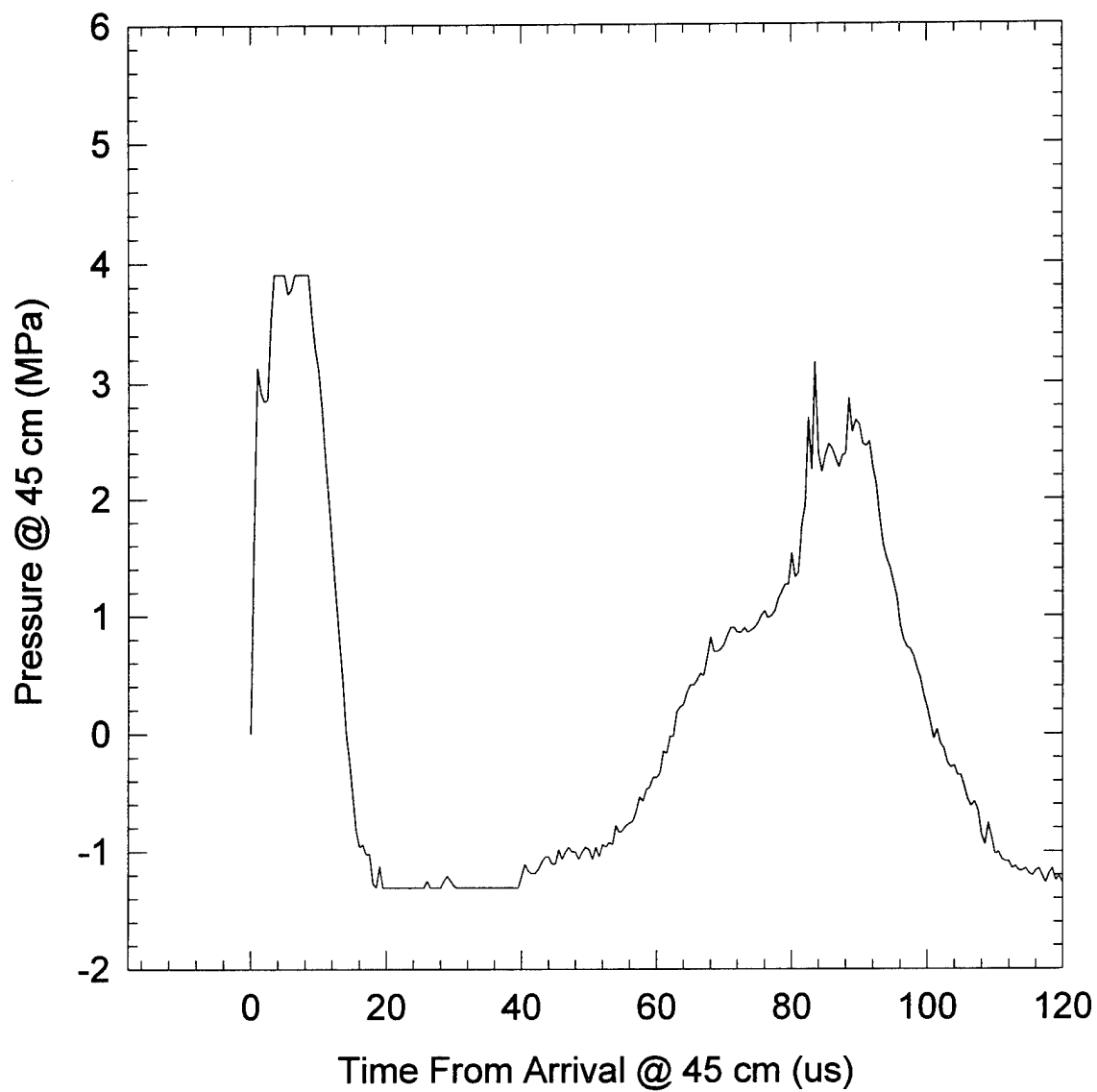


Figure 4-16. Pressure response at 45 cm for Shot #48. This shot also exhibits a strong rarefaction with an after pulse. Note that the channel saturated at about 4 MPa.

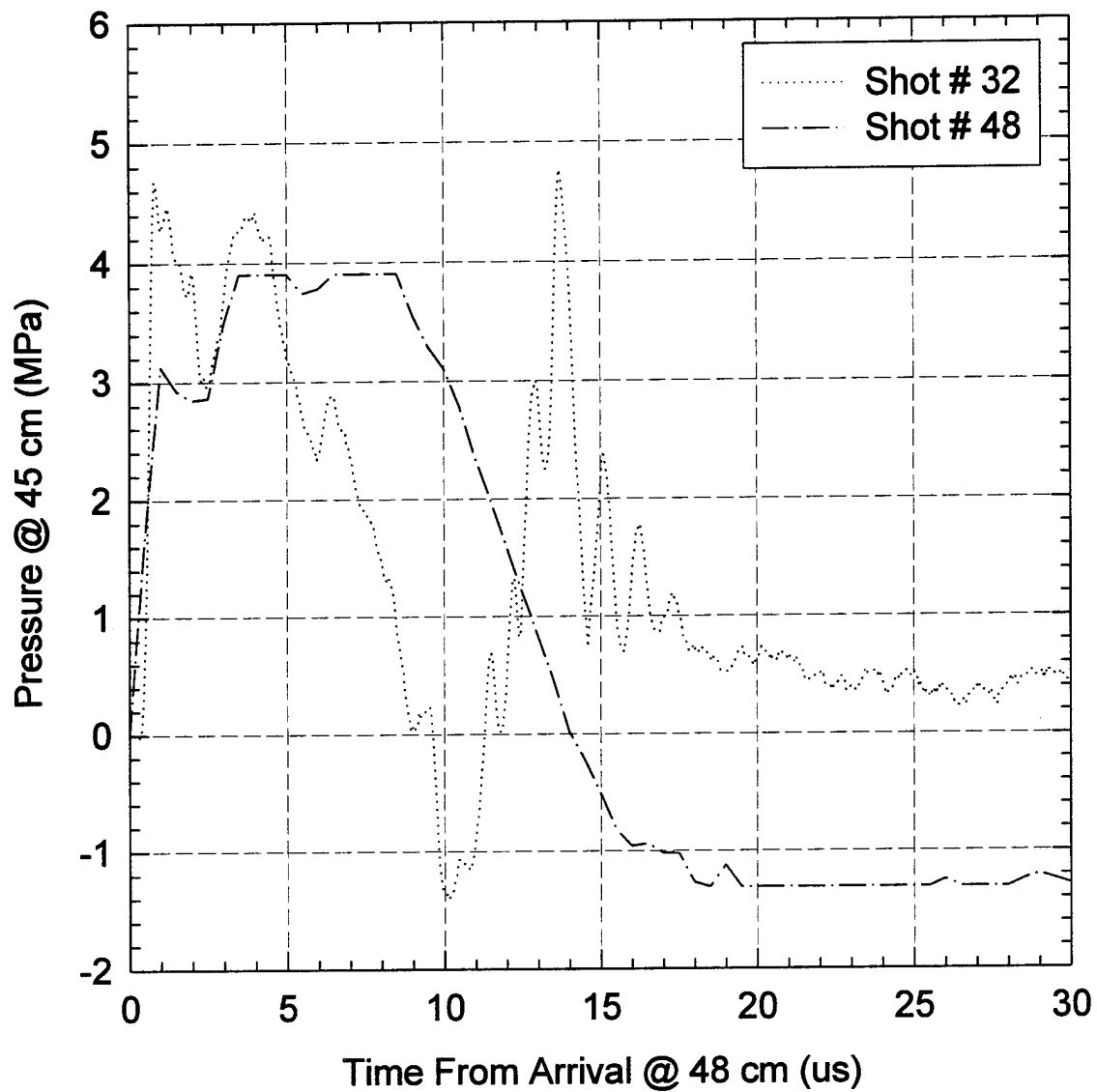


Figure 4-17. Overlay of pressure responses for Shots 32 and 48.

3 μ s period. Recall that these two shots both injected about 2 kJ of energy in approximately 3 μ s. And both pulses appear to reach about the same peak pressure. Note that the underdamped pulse (#32) has a faster rise time but a shorter pulsewidth (defined as the zero crossing time minus the arrival time). This pulse produced an energy fluence at 45 cm of 58 J/m². The overdamped pulse produced an energy fluence of 90 J/m². If an isotropic wave behavior is assumed, the two pulses produced shocks (at 45 cm) of 148 J and 229 J respectively. These are much lower levels than anticipated, but are also very conservative since they do not contain the entire response. The underdamped shot thus had a circuit efficiency (stored electrical to plasma energy) of 15.2% and a coupling or plasma efficiency (plasma to mechanical energy) of 8% for a total efficiency of 1.23%. The overdamped pulse only had a 5.3% plasma efficiency, but a 72% circuit efficiency so the total efficiency was 3%, nearly 3 times that of the underdamped response.

These two shots illustrate not only the process used to analyze the data, but also show that the multi-microsecond energy injection times are too long to efficiently couple energy into the shock. They also confirm other anecdotal reports of little or no improved shock response with greater delivered energy (Ref. 12). Evidently there is a point of diminishing return where additional energy added to the plasma contributes to internal heating and eventually steam bubble growth but not to the desired primary shock. Additionally, although some of this energy may be recovered in the form of a pressure wave at bubble collapse, thermal losses during the bubble lifecycle due to the relatively higher temperatures for plasma induced bubbles, will result in a lower overall efficiency. All indications are that the energy must be loaded within hundreds of nanoseconds to promote efficient coupling of plasma energy to mechanical energy.

The following data set is a compilation and analysis of data taken in the final electrode configuration. For the sake of consistency, data from earlier configurations were not included. These shots were produced with the most accurate diagnostics possible and after numerous problems with the Tourmaline gauges had been dealt with and confidence obtained in their readings. A total of ten shots are presented from Shots #26-50. Other shots were removed from the data set because they had incomplete data, were calibration

shots or because some unusual event occurred during the shot. For example during the analysis some shots did not fit the general trends. Initially this was considered to be due to scatter, but upon closer inspection each was found to be associated with failure of the main electrode support insulator or doubt about the acquired data, so they were removed. Four of these shots were initiated with 3.7 cm wires (hereafter referred to as 4 cm shots) and the remaining six were initiated with wires ranging from 8.25 cm to 10.5 cm (hereafter referred to as 9 cm shots). Where calculations were made using the discharge length, the actual wire length was used.

The shock energy density was computed by squaring the time dependent pressure, dividing by the density and sound speed and then integrating with time out to the first zero crossing of the pressure (see Eq. 2.5). If more than one gauge was available at the same range and equivalent angle the energy density values were averaged.

Figure 4-18 is a plot of the shock energy density in J/m^2 at 45 cm versus the total energy injected into the plasma. Clearly the higher energy long discharge shots produced much stronger shocks. The primary conclusion from the experiment is that a shaped plasma compressed into a small volume can indeed provide a spherical shock with greater energy density than a straight discharge. This proves the main hypothesis of the experiment. To the author's knowledge this has never been previously experimentally demonstrated. In general, the long discharge shots produced energy densities 30% greater than the short discharge shots from the same geometric volume (8.25 cm^3). It was not possible in this experiment to verify the secondary hypothesis that reflected energy from the Alumina could be added to the shock.

The above data were fit to the function $F_s = 15E_p^{1/5}$ with a correlation coefficient of 0.936 (where F_s is the shock fluence and E_p is the plasma energy). Thus the shock energy density scales with plasma energy to the one fifth power. This implies that the average pressure would scale approximately to the one-half power which is a much stronger dependence than would be expected for a spherical geometry (see Eq. 2.2).

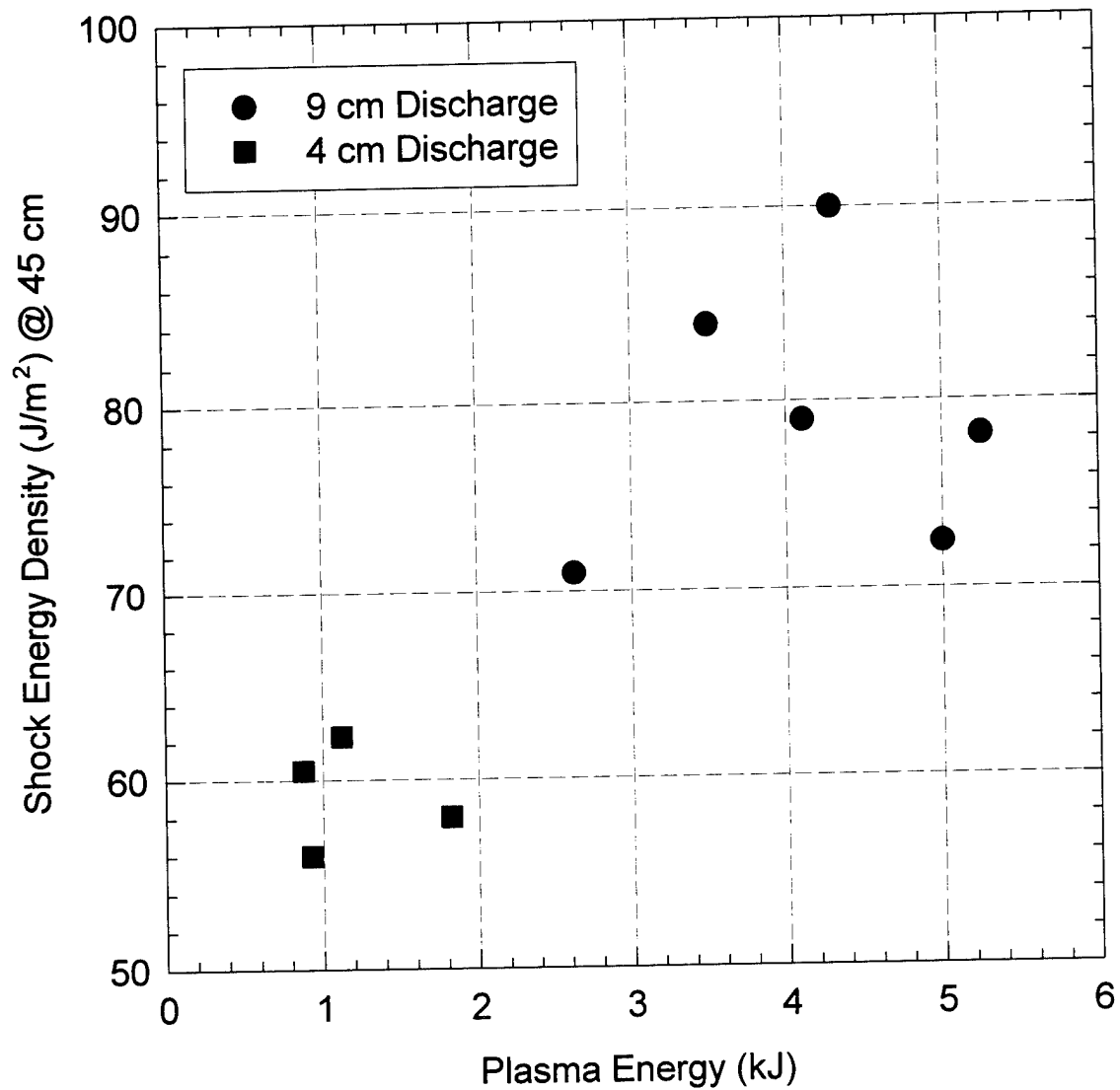


Figure 4-18. Shock energy density versus injected plasma energy. Note that the long discharge produced 30% stronger shocks from the same geometric 8.25 cm^3 volume. This demonstrates one of the main hypotheses of the experiment.

In Figure 4-19 the same data are plotted versus the 10-90% plasma energy injection time (t_p). A similar trend is observed as would be expected since the higher energy shots also had the longer injection times. In this case though, the data fit the relation $F_s = 53t_p^{1/4}$, with a correlation coefficient of 0.931. Evidently, there is a slightly stronger dependence on the injection time.

The plasma energy was divided by the discharge length to obtain the linear plasma energy density (E_l). The shock energy density is plotted against this parameter in Figure 4-20. In this case the fit is $F_s = 13.6E_l^{0.28}$ with a weaker correlation of 0.87.

To search for a stronger dependence, the linear plasma energy density was divided by the injection time to obtain the average linear plasma power density (P_l). Figure 4-21 shows a plot of this data and the best fit determined (with very poor correlation (0.39)) was $F_s = 82 - (P_l^{1.6})/250$. This is a stronger observed dependence and would seem to imply that a higher shock energy density can be obtained by injecting energy more slowly in a long convoluted path within a given small volume.

The shock energy density was used to compute the total energy and efficiency for a relative comparison by assuming the shock wave was isotropic. Measurements of wave arrival times at large angles off axis indicated that at 45 cm the deviation from sphericity was only about 1 cm. Note that these efficiency calculations are very conservative since they do not include the complete pressure response. Figures 4-22 through 4-25 are plots of the isotropic plasma efficiency (η_p , shock energy divided by the plasma energy) versus the previous same parameters.

When the efficiency data versus plasma energy was analyzed, a correlation of 0.986 was obtained for the relation, $\eta_p = 1.56 + (13500/E_p)$. Evidently the higher energy pulses, even though they produce a greater shock energy density, couple the plasma energy into the water much less efficiently than lower energy pulses. This is likely a direct result of loading energy too late in time for contribution to the outgoing shock. A fit to the efficiency versus linear energy density showed a much stronger dependence, but with less confidence (0.85).

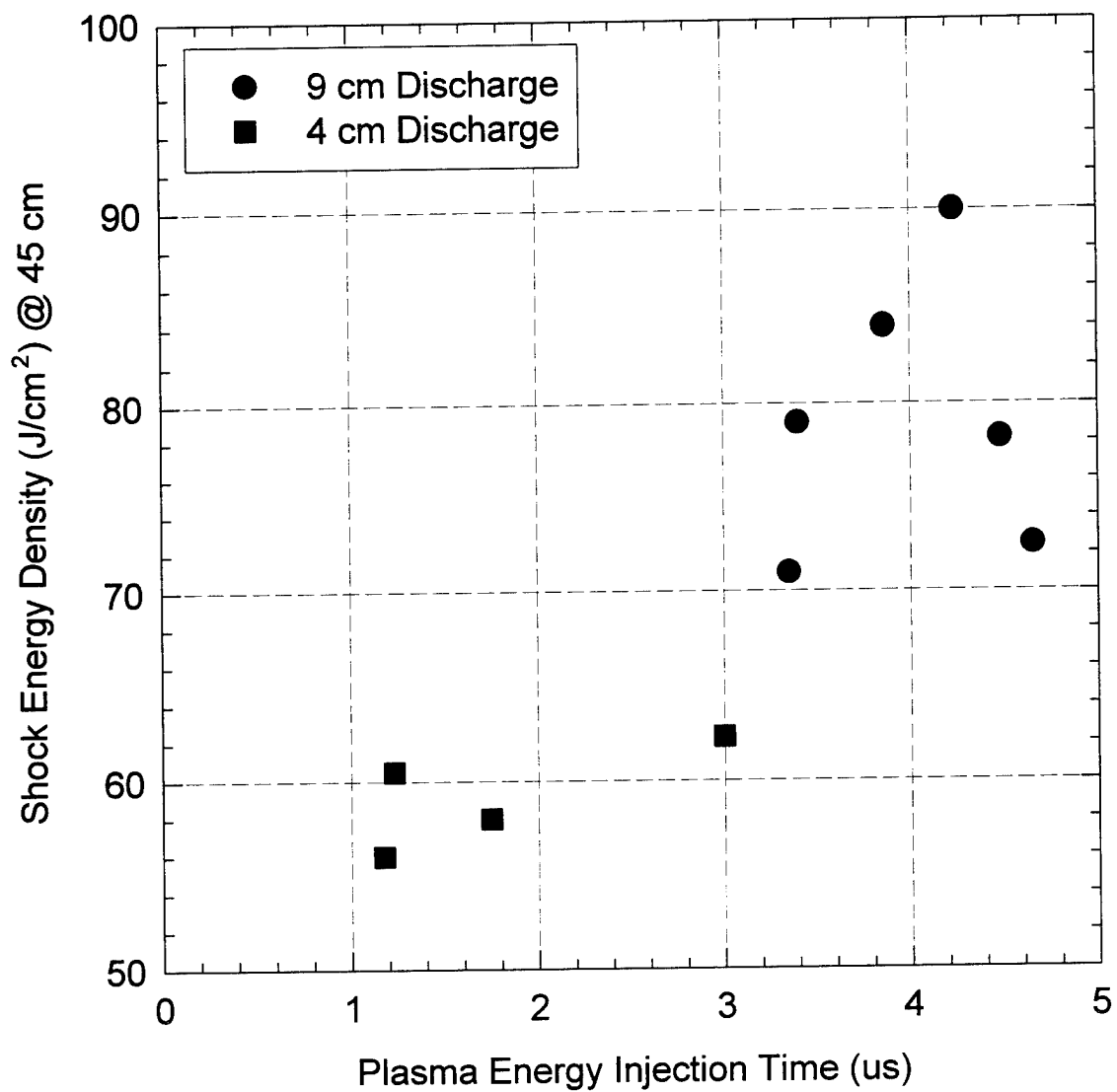


Figure 4-19. Shock energy density plotted against the 10-90% plasma energy injection time. The injection time has slightly stronger impact than the energy.

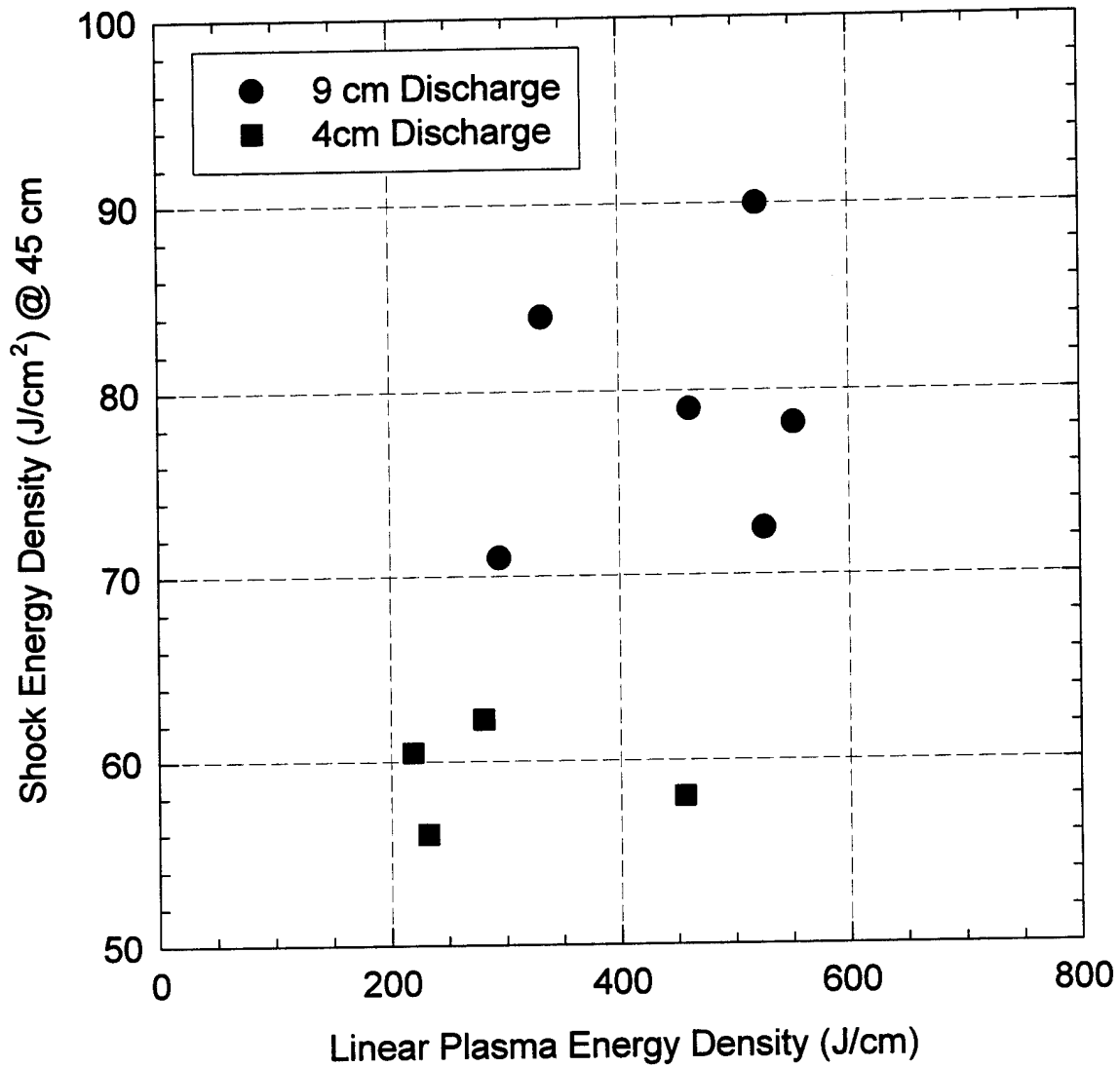


Figure 4-20. The shock energy density plotted against the linear plasma energy density (plasma energy divided by the discharge length).

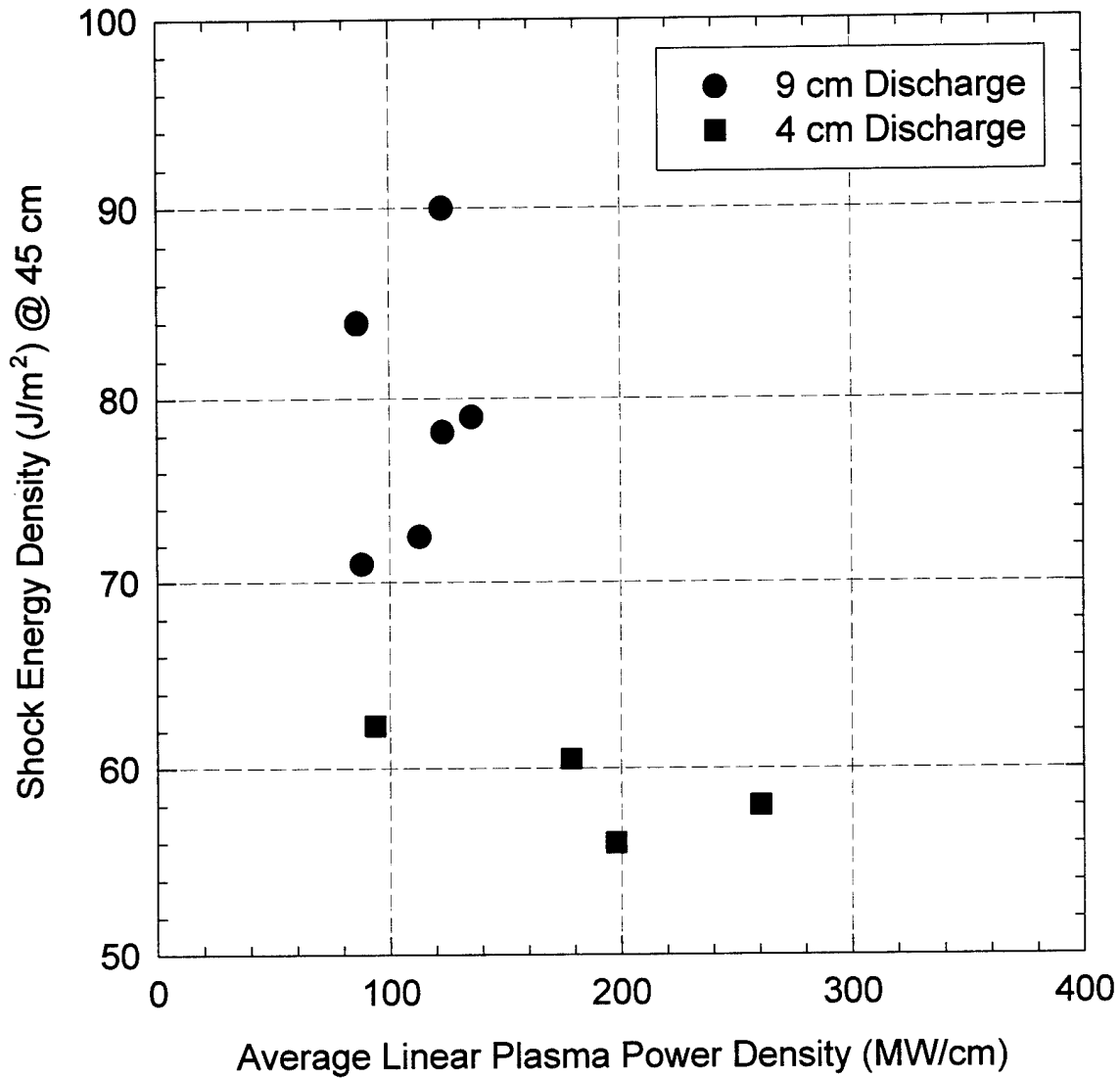


Figure 4-21. The average plasma power density was obtained by dividing the linear energy density by the injection time. Although these data show the strongest dependence, the correlation is poor.

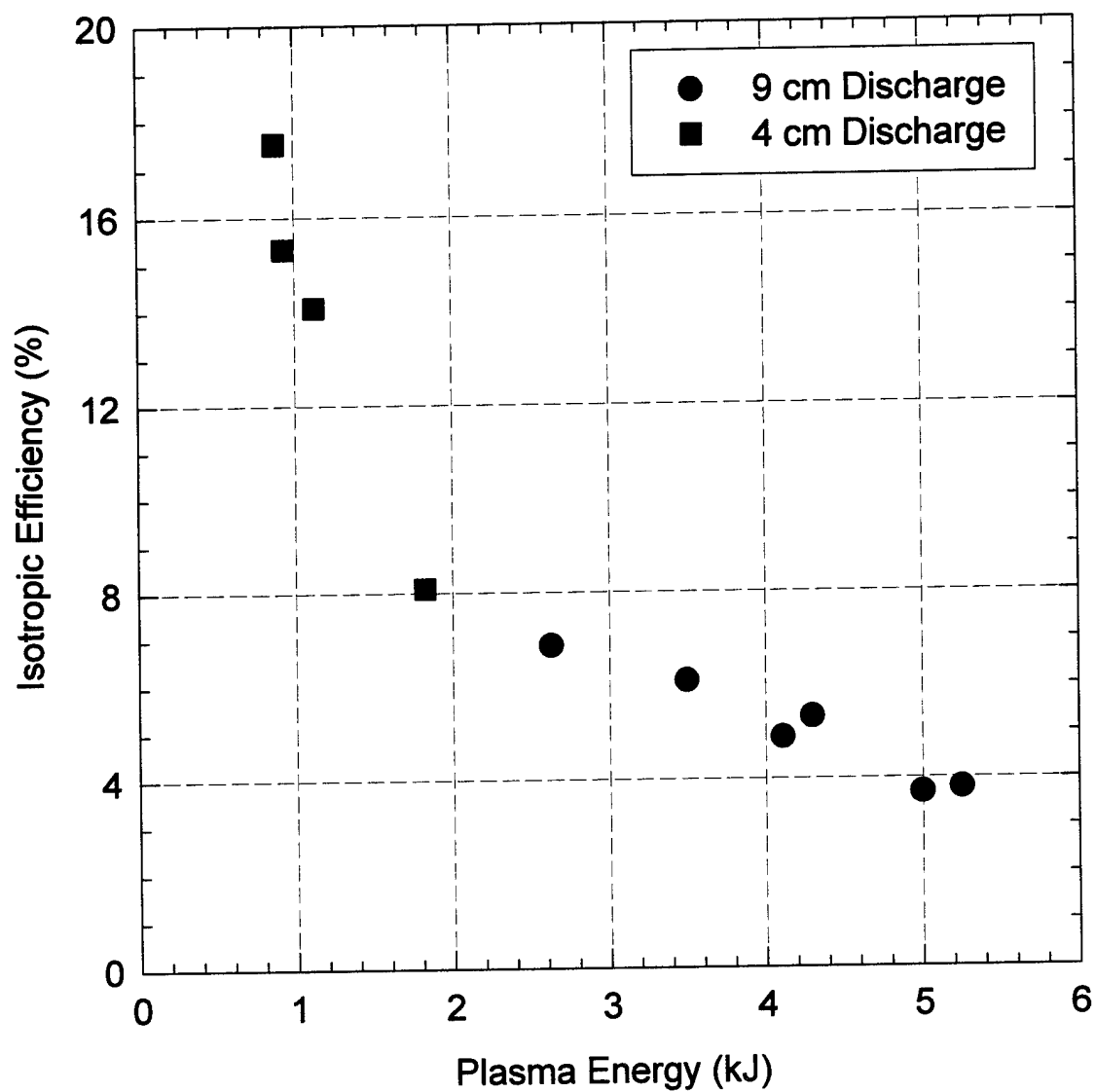


Figure 4-22. Plot of efficiency of coupling plasma energy to shock energy (η_p). The coupling efficiency falls off inversely with energy.

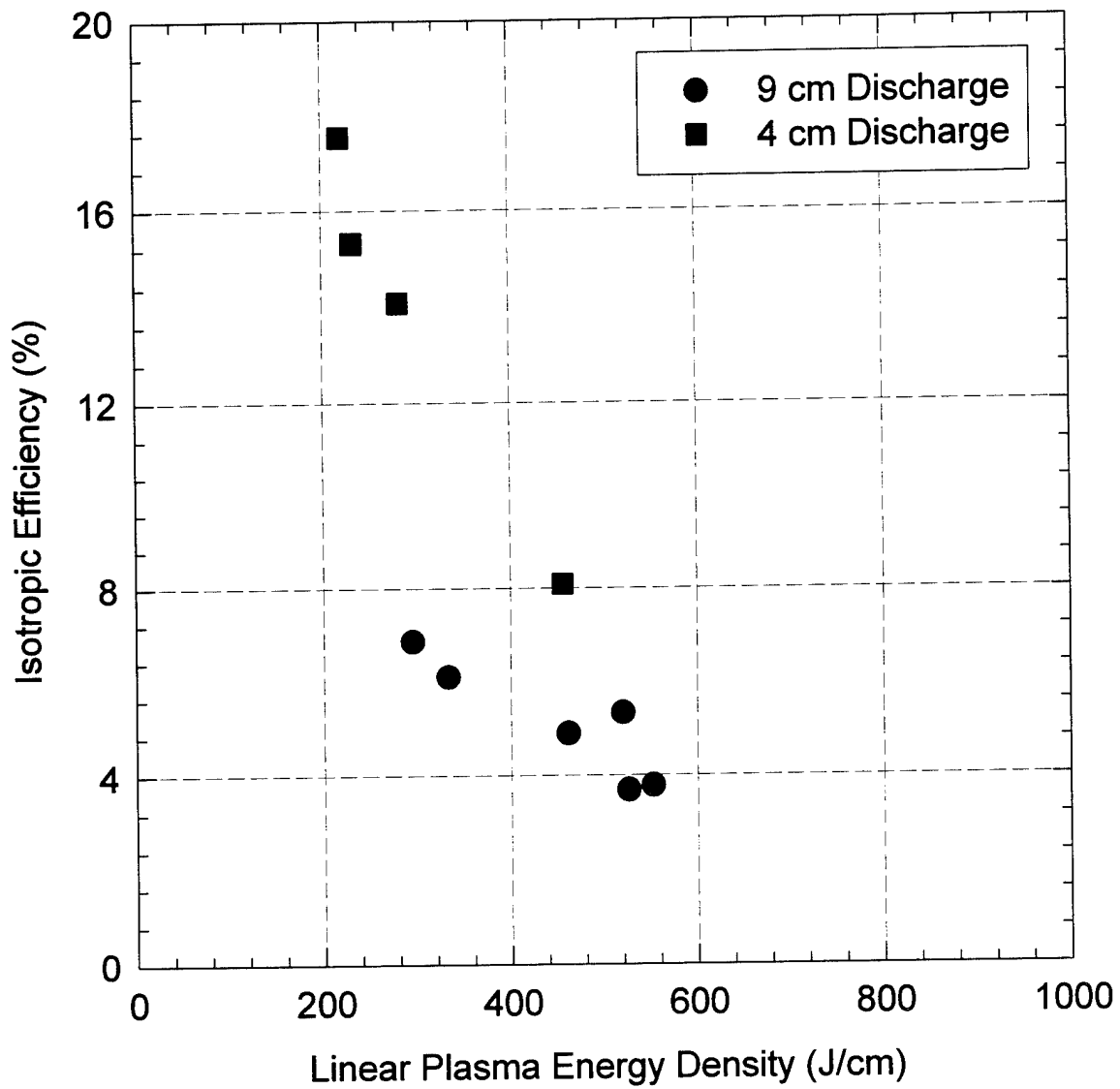


Figure 4-23. Plot of isotropic efficiency (η_p) versus linear energy density (E_l). In this case the coupling efficiency falls off inversely with the square of the energy density.

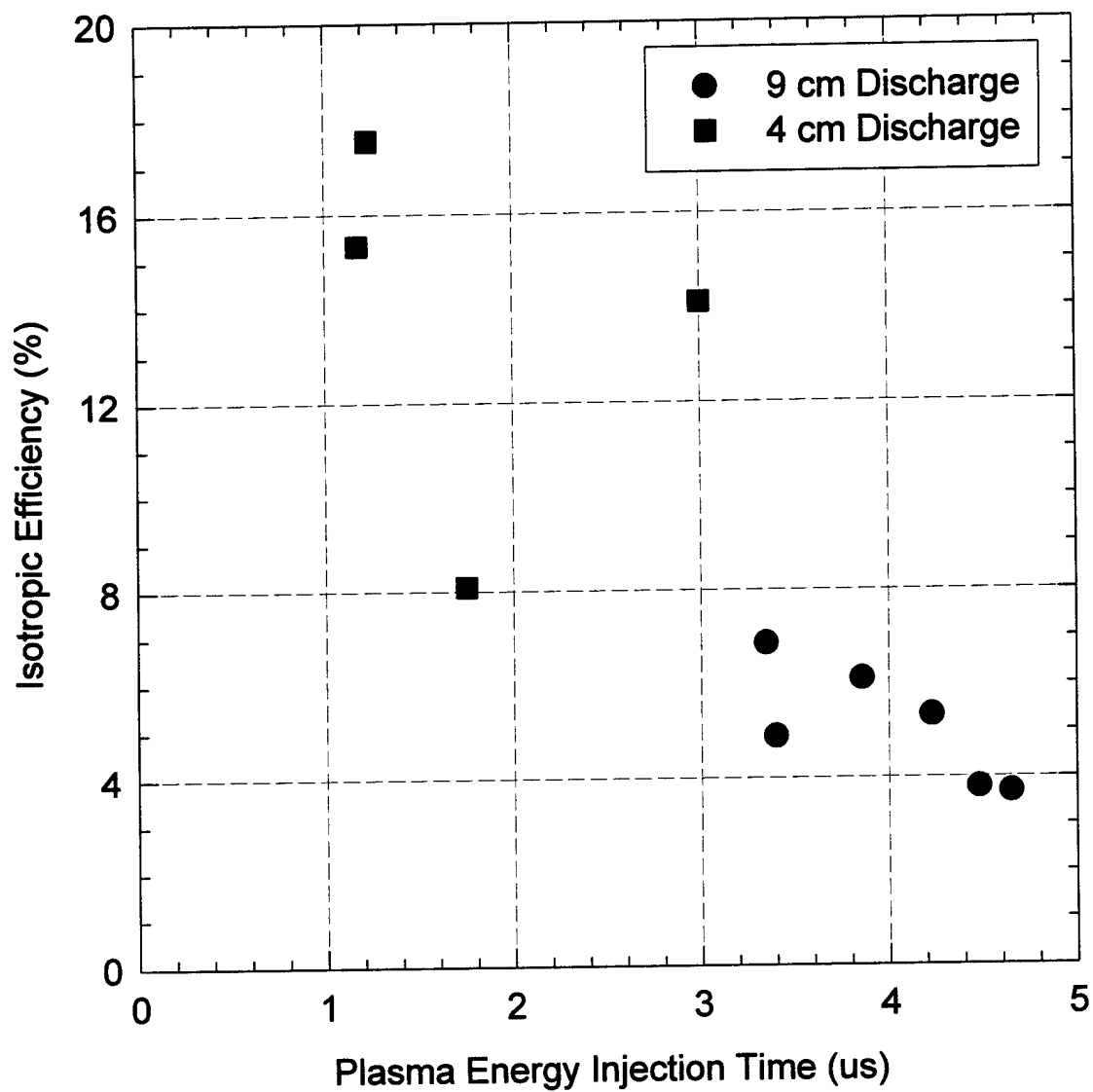


Figure 4-24. The coupling efficiency correlation with injection time is poor (0.71) due to a couple of outlying points. The efficiency scales as $t_p^{1/3}$.

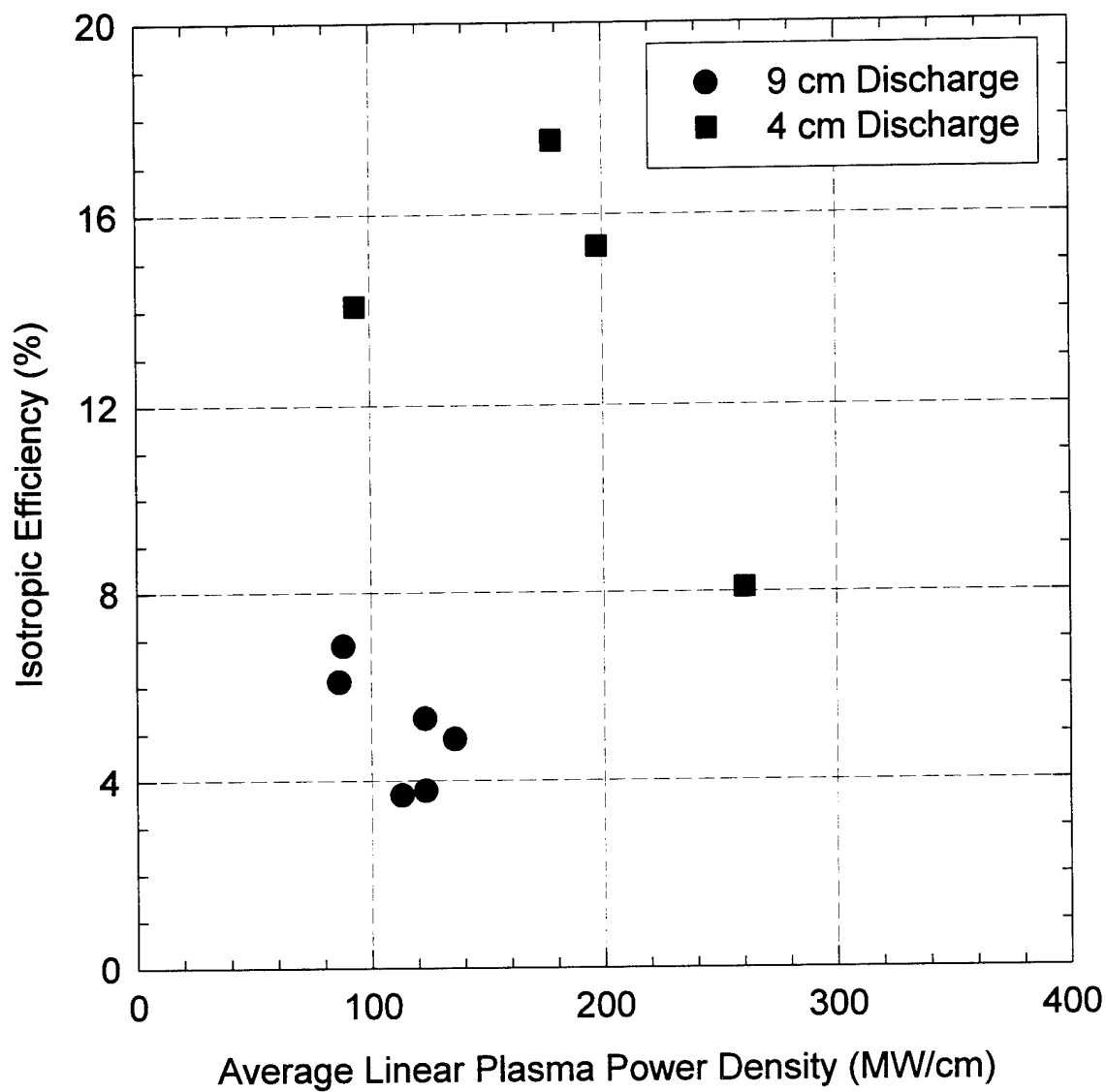


Figure 4-25. Very large scatter is observed in the coupling efficiency versus average linear plasma power density. In this case the efficiency scales as the square root of P_p .

In this case the established relation was $\eta_p = 1.78 + (857/E)^2$. This shows that the efficiency falls much more rapidly with increased linear energy density than with increased plasma energy. This is consistent with an interpretation that higher energy density would contribute to more rapid expansion and bubble formation thus reducing the amount of energy coupled to the shock.

Continued analysis of the data for the injection time and average plasma power density dependence showed poor correlation (0.71 and 0.32 respectively) with the best fit relationships being approximately $\eta_p = 35(1 - 0.5t_p^{1/3})$ and $\eta_p = 0.6P_l^{1/2}$. For such poor correlation and weak dependencies, the conclusion that must be drawn, for this data set, is that the linear plasma energy density is the primary control mechanism for the coupling efficiency. Stated another way, the longer the discharge for a given amount of energy the greater the amount of energy that can be coupled to the water from the plasma.

Many "cut and try" tests were run with various length wires to optimize the discharge. The circuit response was found to be very sensitive to the wire length and during the tests it seemed as though the nominal 9 cm wires had provided the highest plasma energies. However, these shots were typically overdamped and it is possible that an exactly critically damped shot might have been more efficient. Of course there is no way to confirm that the actual discharge path length was exactly the wire length, but in general the path followed the wire. To the extent that the measured wire length prior to application to the ceramic represented the actual wire length attached to the electrodes and variations in the discharge were minor, this length is an adequate representation. Some of the scatter in the data may be due to shot-to-shot variations in the plasma response associated with the wire, however.

Figure 4-26 is a plot of the circuit efficiency (η_c) obtained by dividing the plasma energy by the energy stored in the capacitors at voltage, versus the discharge gap length. It appears that the optimum discharge gap length was likely closer to 6 or 7 cm rather than the nominally 9 cm gap tested.

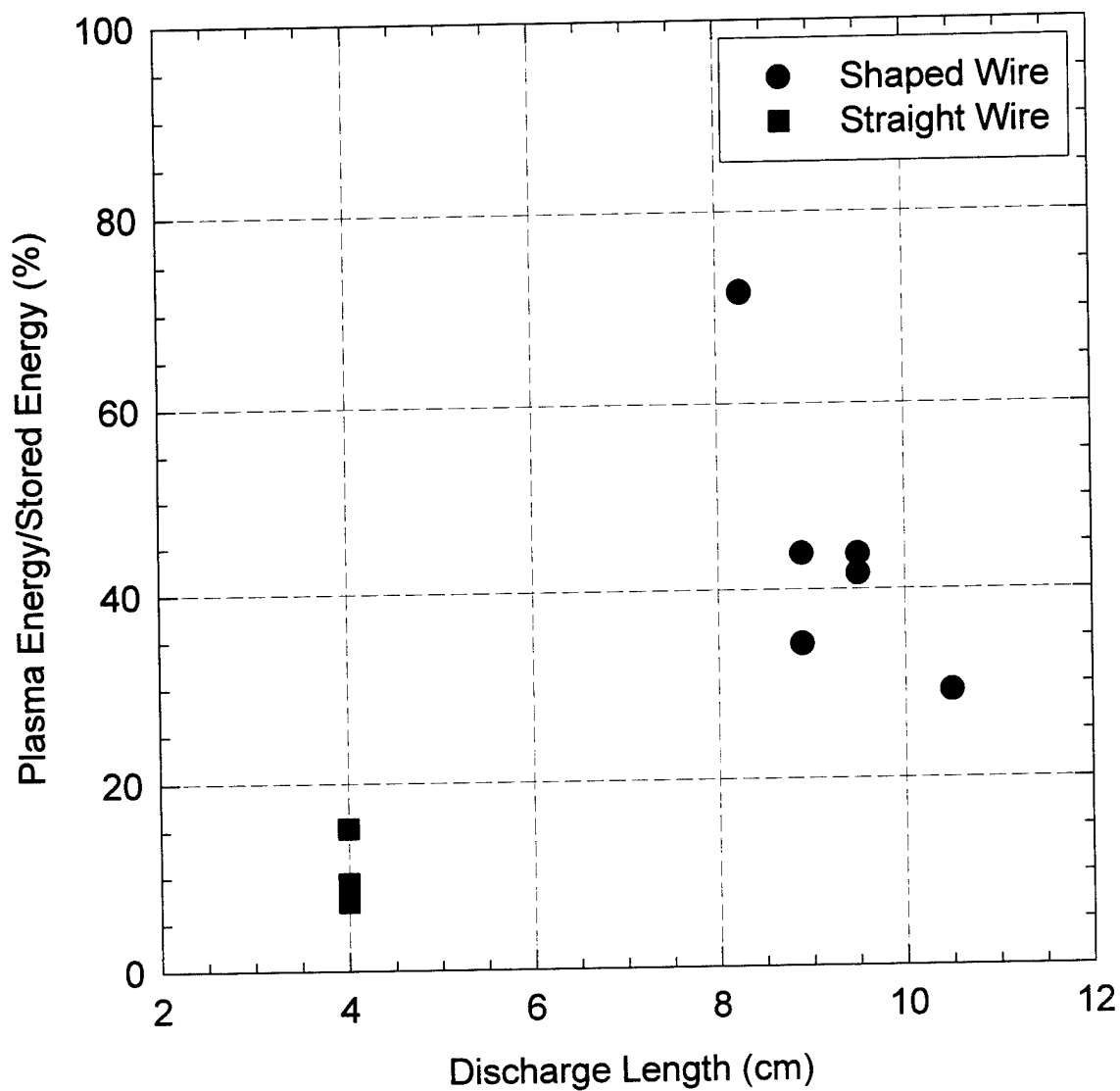


Figure 4-26. Plot of the circuit efficiency (η_c) versus the discharge gap length. Note that the optimum efficiency was likely between 5 to 7 cm where a critically damped pulse would be expected to provide more energy than the overdamped discharges of 9 cm.

The total efficiency (η_T) was computed as the product $\eta_p \eta_c$. This value is plotted versus the discharge length in Figure 4-27. Although the short wire typically produced a much higher coupling efficiency, the longer shaped wires provided a significantly higher circuit efficiency and consequently a higher total efficiency.

The final data taken were range measurements where gauges were placed at 3", 6", 12", 18", and 24" from the center of the outside surface of the ceramic. The gauges at 3 and 6 inches were $\pm 45^\circ$ from the normal in the horizontal plane. The gauge at 12" was 30° off normal and the gauge at 24" (later moved to 18") was on axis in the horizontal plane. Several shots were fired within the limited time remaining. One good data set was obtained after the dynamic range of the digitizers was optimized. Unfortunately, in all cases, the gauge at 6" exhibited a shorter pulsewidth than those at all other ranges. Subsequent data analysis showed the energy density to be lower than the gauges at longer ranges also. This data was therefore not used in the analysis. The pressure from the gauge at 24" was digitally noisy so it was moved in to 18". The discharge length for all of these shots was 3.25" and the stored energy was 6 kJ. For the data presented, the circuit efficiency was 60-62% (3.6-3.75 kJ plasma energy) and the injection time was 3.5 to 4.4 μ s. The data were not averaged since too few shots were available.

The shock energy density for the full pulsewidth from Shot #55 (points at 0.0762, 0.3048, and 0.4572 m) was fit to the relationship $E_d = 22.6 R^{-1.5}$ (where R is the range in meters) with a correlation coefficient of 0.999999 and a standard deviation of 0.84 J/m². This relationship is plotted as the solid line in Figure 4-28. Shown also is the energy density at 61 cm from Shot #52. Note that this point lies on the same curve as the data from 7.62 to 45.72 cm. Also shown are the energy density values for the same shot but only out to the point in time of the first zero crossing of the pressure. These data were also fit (with a lower error, 0.34 J/m²) to the same functional form, but with a lower coefficient or $E_d = 10.26 R^{-1.5}$. Remarkably, this curve is almost exactly half that generated from the full pulsewidth data which contains the previously described rarefactions and oscillations. It may be possible that these responses are not due to reflections but some sort of instability that grows slowly and then damps as the shock propagates further. This was observed in the range data where

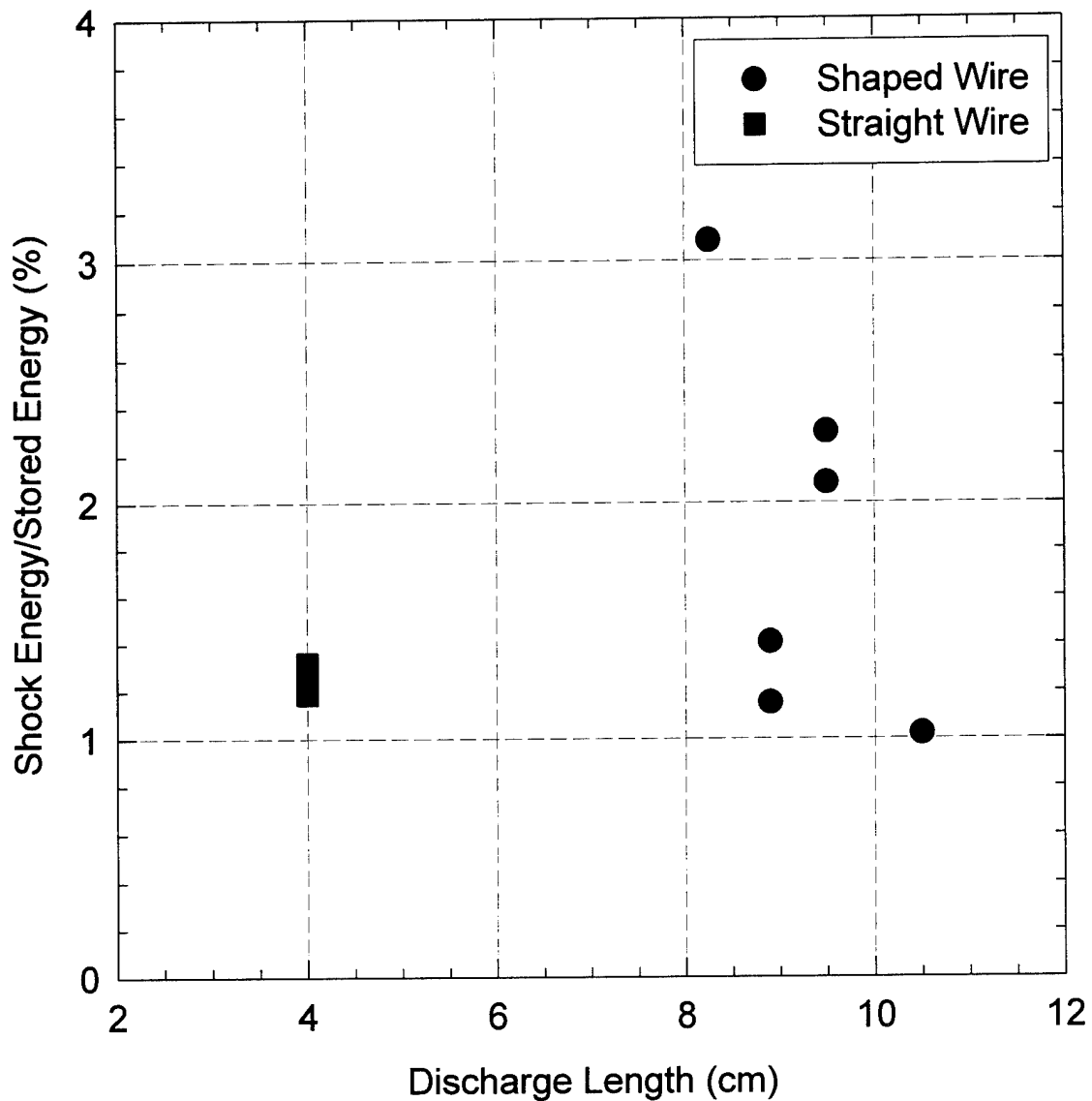


Figure 4-27. Plot of the total efficiency (η_T), obtained by the product of the coupling or isotropic efficiency and the circuit efficiency, versus the discharge length. Note that although the long discharges had very low coupling efficiencies, because of the higher circuit efficiency the total efficiency was higher.

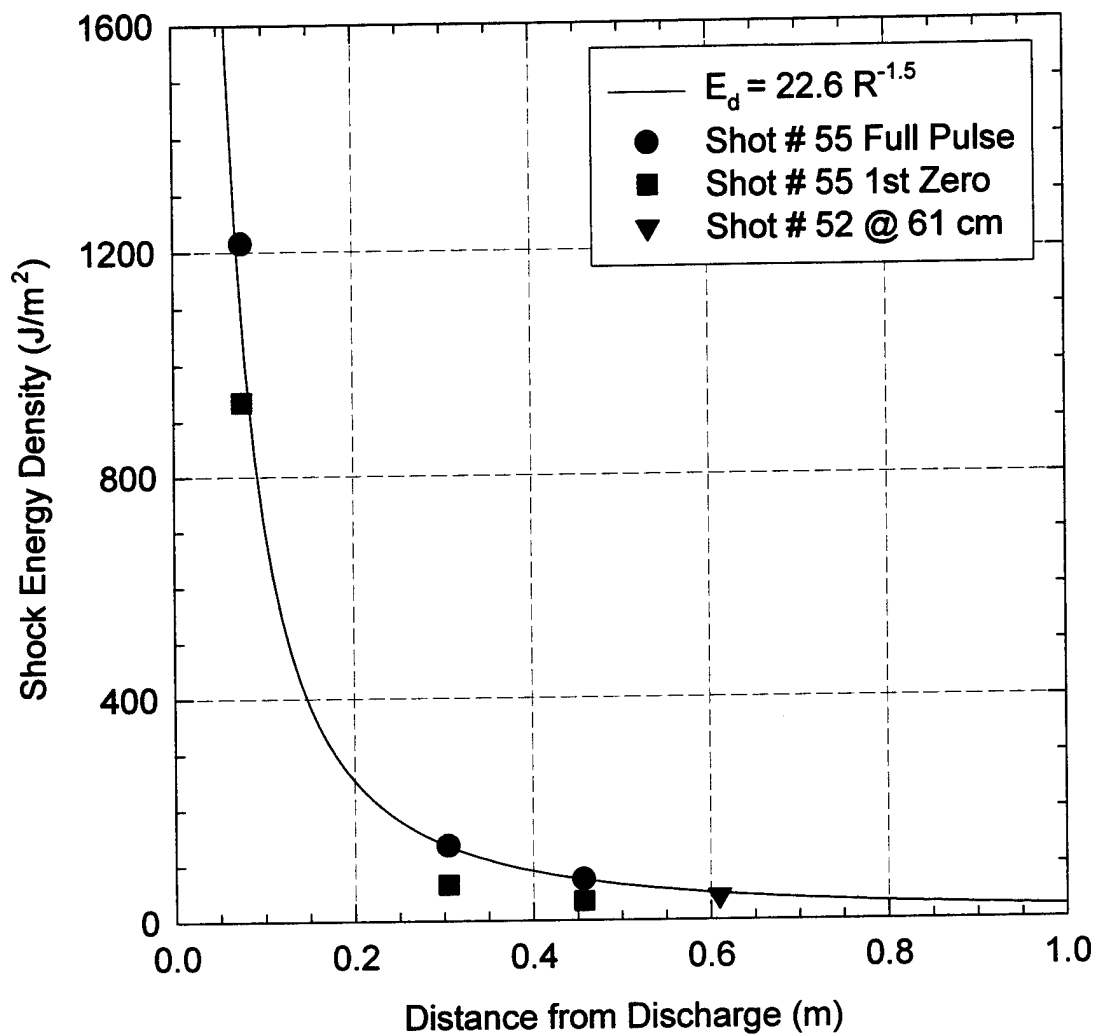


Figure 4-28. Plot of range data for two shots with gauges positioned from 7.6 cm to 61 cm. The solid line is the relationship $E_d = 22.6 R^{-1.5}$.

the close and far data were relatively clean but the intermediate range data showed odd oscillations. If this is the case, the previously mentioned efficiency values are low by a factor of two.

Evidently the energy density falls off a little more slowly than isotropic. However, the fit is based upon limited data and the error for R^2 behavior was not significantly higher. Several shots were attempted with a gauge at 3.81 cm but the digitizer went out of range at 160 MPa and it was impossible to resolve the peak pressure behavior. Also the gauge was only calibrated to 70 MPa. For the sake of completeness, the peak pressure was assumed to be 70 MPa, but only for the duration of the gauge response time of 1.5 μ s. For the remainder of the time the digitizer was clamped, the pressure was assumed to be 16 MPa which was the last value recorded before it went offscale. The calculated energy density in this case was 9053 J/m². When this point was added to the longer range data the best fit exhibited a R^2 dependence. This energy density for an isotropic total energy calculation gives 165 J. For a 4 kJ plasma energy the plasma efficiency would be about 4% and the total efficiency would be about 2.75% which is consistent with the results obtained at 45 cm.

The peak shock pressures for the estimated pressure at 3.8 cm and the measured pressure at the other ranges are plotted in Figure 4-29. Also shown is the best fit to these data, $P^1 = -0.029 + 1.147 R$. The pressure falls off as expected for a spherical wave. This indicates that the estimated pressure at 3.8 cm is probably reasonable and confirms the spherical wave behavior determined by shock arrival times. This determination was made with gauges at 45.75 cm and on vectors at 0° and at $\pm 63^\circ$ in the vertical and horizontal planes. In a single pulse the arrival times were within 10 μ s which represents a maximum distortion of 1.5 cm or about 3% of the radius of the wavefront at 45 cm.

In contrast, the SPH simulation of the 4 cm, 20 kJ discharge had a peak pressure of 600 MPa at 2.8 cm versus the 70 MPa at 3.8 cm in the experiment. The linear plasma energy density for this run was 5 kJ/cm which is almost ten times that in the experiment. Since the simulation had an instantaneous energy injection this could be expected to offset

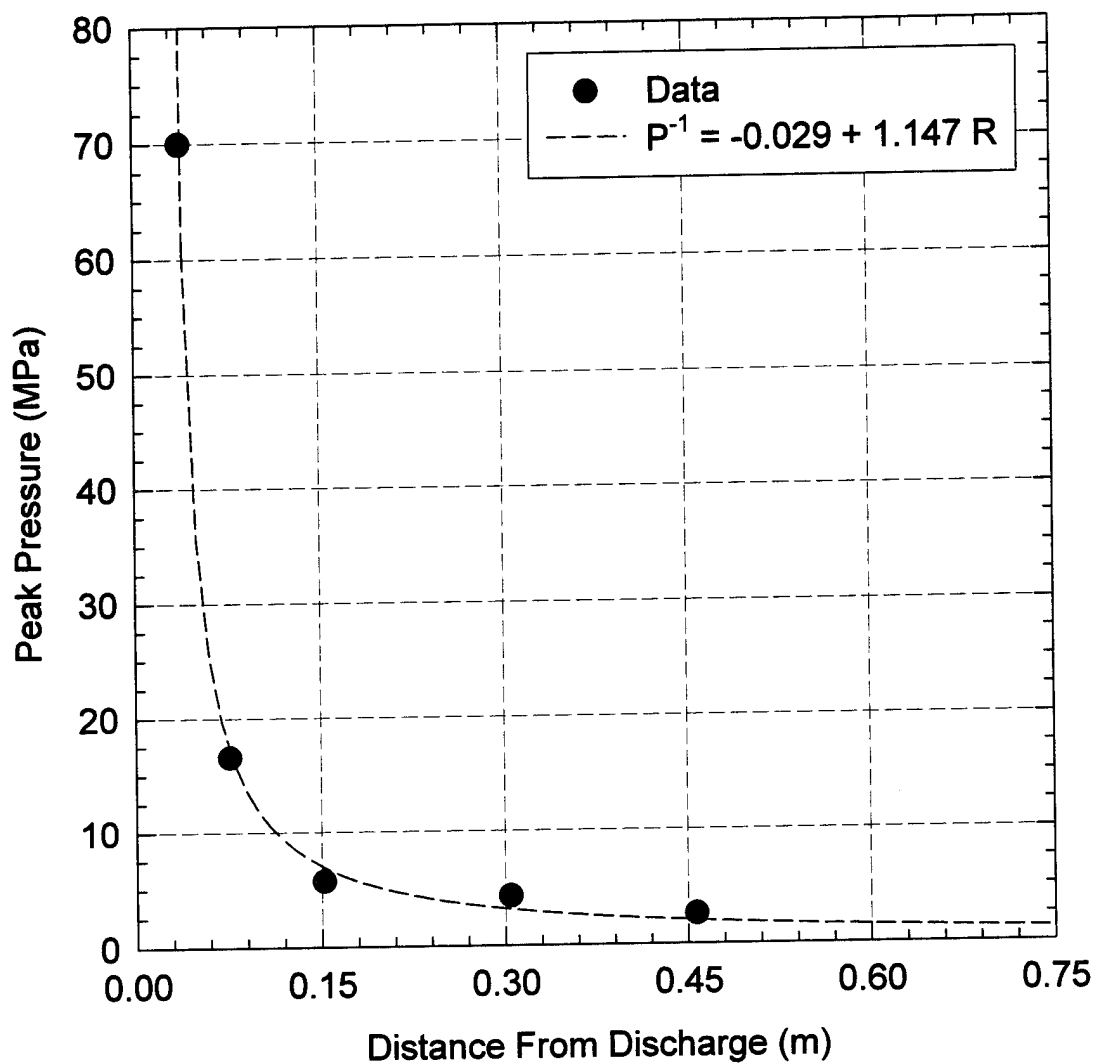


Figure 4-29. Plot of pressure data versus range for several shots. The 70 MPa, 3.81 cm point is estimated since the pressure was out of range for the gauge and digitizer. The dashed line is the best fit to the data and exhibits an R^{-1} dependence.

the effects of the energy density on reducing the efficiency. In fact, estimates of the total shock energy at 3 μ s and 6 μ s into the simulation indicated a coupling efficiency of only 11.5% (2300 J). Approximately 18 kJ is partitioned into the multi-phase fluid behind the shock. At 6 μ s, the sausage shaped bubble had grown to a 1.2 cm diameter (7.4 cm^3) with an average internal temperature of 3000 K. This represents an average bubble wall velocity of 750 m/s. Note that, at this time, the shock was out to nearly 2 cm from the initial channel and had an average velocity of 3000 m/s. As early as 3 μ s, the bubble was over 0.25 cm behind the tail end of the shock wave. This indicates rapid separation of the plasma/shock boundary. Any energy injected after this separation would not be expected to couple to the shock.

This aspect of the phenomena explains the low efficiencies obtained in the Phase II effort. In Phase I the linear plasma energy density was about 50 J/cm and the injection time about 200 ns. These are much more optimum parameters for efficient coupling than even the 5 kJ/cm, instantaneous injection in the simulation let alone the 500 J/cm, 3 μ s injection in the Phase II experiment.

SECTION 5

CONCLUSIONS

A shaped discharge has been successfully implemented to produce a spherical wave from an effective energy density of 584 J/m^3 as the source. This was accomplished with circuit efficiencies as high as 70%.

For 2 to 4 μs energy injection times, higher energies have been shown to lead to lower coupling efficiencies from the plasma to the water. Specifically, the greater the energy per unit length of the discharge, the lower the coupling. This may be due to rapid heating of the surrounding fluid which results in lower coupling of the energy into the shock during the plasma discharge.

Also reduced energy injection times have been shown to have higher coupling efficiency, but at the sacrifice of circuit efficiency for the circuit configuration tested.

The experimental results have shown the necessity of rapid energy injection to achieve high efficiency. In Phase I, the overdamped response demonstrated an estimated total efficiency of 40% while the oscillatory response had an estimated efficiency of only 14%. In Phase I though, the energy injection time was an order of magnitude faster (less than 200 ns). In Phase II, with energy injection times from 2 to 5 μs , the total efficiencies were about an order of magnitude smaller (1 to 4%). With an assumed similar circuit efficiency (70%), subsequent analysis of hydrocode simulations with order of magnitude higher linear energy densities (5 kJ/cm) and instantaneous energy injection showed a total efficiency of about 12%.

The results of both phases have dramatically demonstrated that the most efficient way to provide high energy from stored electrical to radiated mechanical is with a relatively high impedance transmission line circuit similar to that used in Phase I. The average plasma resistance calculated for the overdamped discharge (9 cm) over the period of time that 90% of the energy was delivered (3.8 μs) was 1.28Ω . For a 7 cm discharge in Phase I, an

injection time of less than 200 ns was obtained for a 2.5 Ω transmission line. The discharge resistance information was not available at the end of Phase I to guide the Phase II design.

The main difficulty encountered in Phase II was survivability of the electrodes and their support structure. A design that imbeds the transmission line in a larger tank will be necessary not only for survivability, but for the purpose of providing a non-intrusive environment for bubble growth and diagnoses.

What was believed at the time to be very large shock energies due to the comparatively greater loudness of Phase II over Phase I, is now attributed to bubble collapse. Although the coupling efficiencies were lower in Phase II, the circuit efficiency was just as high. This indicates that substantial energies were imparted to creation of steam and subsequent bubble growth. Using Equations 3.4 and 3.5, the estimated free-field bubble size for the 4-5 kJ plasma energies obtained in the experiment is approximately 21 cm in diameter with a period of time to collapse of 39 ms. The bubble collapse pressure would be extremely high in this case due to the bubble size. Unfortunately, there was no means to diagnose the size of the bubble. No attempts were made to measure the pressure out to the tens of milliseconds required to diagnose the bubble collapse pressure pulse, due to the reverberation.

There are strong implications, based on these results, for simulation using high explosives (HE) or numerical simulations that depend upon HE results. The fact that the coupling efficiency from the plasma to the water is strongly dependent upon the energy for the microsecond time scales used here, implies that relationships developed for shock characteristic behavior from HE tests dependent upon available chemical energy or "yield" may be extremely suspect when applied to nuclear generated phenomena with radically different behavior than conventional explosives.

Additionally, the relatively higher temperatures associated with the plasma state found in electrical discharges and nuclear explosions due to their higher initial energy densities casts further doubt on HE comparisons. These effects and their relative importance in shock generation should be given priority for study rather than calculations, tests, demonstrations,

or simulator development that provide estimates of "range to effect" that may bear a limited relationship to the physics of interest.

Evidently, use of a "pill" source (commonly accepted procedure for nuclear coupling) for calculations shows that a calculated HE scaled burst is more efficient than the equivalent nuclear burst by 67%, but the two responses at far ranges resemble each other (Ref. 13). This is used as justification for calculated nuclear environment predictions if the calculations can reproduce the HE event response. There is inherent danger in such an assumption if the "pill" source acceptance is based on calculations which reproduce HE event responses. Based on the results of this experiment, nuclear coupling may be even less efficient than indicated above. Perhaps a less risky alternative would be to use the understanding that can be gained from detailed laboratory study of the "nuclear-like" water plasma for development of code nuclear sources. In this way the calculations are directly validated by a convenient experimental phenomena that is far more similar to the nuclear environment than HE.

In spite of the many years of research devoted to the use and study of pulsed power produced water plasmas, there is much that is unknown about the phenomena. Most of the existing literature is experimentally limited in scope and depth or depends upon unverified analytical descriptions of behavior. The current effort to develop a simulator using a water plasma is premature. Less emphasis should be placed on creation of a spherical wave for simulation and more attention should be devoted to development of a better understanding of the extreme time-scale sensitivity of the near field coupling from the plasma, early time thermal losses, and subsequent bubble behavior. If it is true that a nuclear event has only 60% of the efficiency of HE, it is possible that the subsequent bubble collapse could have an impulse close to or larger than the primary shock. This would result from the relatively greater effectiveness at bubble growth for the higher temperature nuclear event than HE, in the same fashion as the water plasma. The implications of such a double-bang for structures response justifies the effort involved to determine if "fast-burn," high density energy release produces different bubble phenomena than HE.

SECTION 6

REFERENCES

1. G. R. Hess and R. F. Stellingwerf, "Plasma Driven Water Shock Phase I Final Report," DNA-TR-91-72, March 1992. (UNCLASSIFIED)
2. G. R. Hess and A. E. Rodriguez, "Sonoluminescence from Large, Plasma-induced Vapor Bubbles," 127th Meeting of the Acoustical Society of America, Austin, TX, November 1994. (UNCLASSIFIED)
3. R. H. Cole, *Underwater Explosions*, Dover Publications, Inc. New York (1948). (UNCLASSIFIED)
4. G. Goodfellow, private communication, August 1990. (UNCLASSIFIED)
5. J. C. Martin, unpublished notes (1954). (UNCLASSIFIED)
6. J. C. Martin, "Nanosecond Pulse Techniques," SSWA/JCM/704-49(V). (UNCLASSIFIED)
7. W. D. Kingery, H. K. Bowen, and D. R. Uhlmann, *Introduction to Ceramics*, 2nd ed., John Wiley & Sons, New York, 1976, p. 777. (UNCLASSIFIED)
8. R. F. Stellingwerf, private communication, February 1994. (UNCLASSIFIED)
9. H. I. Willis, "Underwater Explosions, Time Interval Between Successive Explosions," Brotosh Report WA-47-21 (1941). (UNCLASSIFIED)
10. E. A. Martin, "Experimental Investigation of a High-Energy Density, High-Pressure Arc Plasma," *Journal of Applied Physics*, Vol. 31, No. 2, February 1960. (UNCLASSIFIED)
11. R. J. Adler, *Pulsed Power Formulary*, August 1989. (UNCLASSIFIED)
12. I. Smith, private communication, June 1993. (UNCLASSIFIED)
13. R. England, et al., "Calculated Water Shock for a Small-Scale HE Experiment," US Army Corps of Engineers, Waterways Experiment Station Contract Report SL-93-4, August, 1993. (UNCLASSIFIED)

DISTRIBUTION LIST

DNA-TR-95-76

DEPARTMENT OF DEFENSE

DEFENSE INTELLIGENCE AGENCY

ATTN: DB-6E1
ATTN: DIW-4
ATTN: OGA-4B2

DEFENSE NUCLEAR AGENCY

2 CY ATTN: ISST
ATTN: WE

DEFENSE TECHNICAL INFORMATION CENTER

2 CY ATTN: DTIC/OCF

FIELD COMMAND DEFENSE NUCLEAR AGENCY

ATTN: FCTO

DEPARTMENT OF THE ARMY

ARMY RESEARCH LABORATORIES

ATTN: TECH LIB

U S ARMY CORPS OF ENGINEERS

ATTN: CERD-L

U S ARMY ENGR WATERWAYS EXPER STATION

ATTN: CEWES-SD
ATTN: J ZELASKO CEWES-SD-R
ATTN: R WHALIN CEWES-ZT
ATTN: RESEARCH LIBRARY

U S ARMY NUCLEAR & CHEMICAL AGENCY

ATTN: MONA-NU DR D BASH

U S ARMY WAR COLLEGE

ATTN: LIBRARY

DEPARTMENT OF THE NAVY

DAVID TAYLOR RESEARCH CENTER

ATTN: CODE 172
ATTN: CODE 173
ATTN: CODE 1740
ATTN: CODE 1750
ATTN: CODE 1770
ATTN: CODE 2740

DEPARTMENT OF NAVY

ATTN: J PETROUSKY CODE 40

MARINE CORPS

ATTN: CODE POR-21

NAVAL COASTAL SYSTEMS CENTER

ATTN: CODE 7410

NAVAL RESEARCH LABORATORY

ATTN: CODE 5227 RESEARCH REPORT

NAWC-WD CODE 4712E00D

ATTN: CODE 2741 D HERIGSTAD

NEWPORT NEWS SHIPBUILDING

ATTN: DEPT E20 S RUNGE

NUWC, DETACHMENT NLON

ATTN: CODE 0261

OFFICE OF CHIEF NAVAL OPERATIONS

ATTN: NOP 091
ATTN: NOP 223
ATTN: NOP 225
ATTN: NOP 37
ATTN: NOP 605D5
ATTN: NOP 957E
ATTN: NUC AFFAIRS & INT'L NEGOT BR
ATTN: N851
ATTN: OP 21

OFFICE OF NAVAL RESEARCH

ATTN: CODE 1132SM
ATTN: CODE 23

DEPARTMENT OF THE AIR FORCE

AIR FORCE INSTITUTE OF TECHNOLOGY/EN

ATTN: COMMANDER

HQ USAF/CCN

ATTN: AFCCN

DEPARTMENT OF ENERGY

DPEARTMENT OF ENERGY

ATTN: DR C V CHESTER

LAWRENCE LIVERMORE NATIONAL LAB

ATTN: D MAGNOLI

LOS ALAMOS NATIONAL LABORATORY

ATTN: REPORT LIBRARY
ATTN: TECH LIBRARY

SANDIA NATIONAL LABORATORIES

ATTN: TECH LIB 3141

OTHER GOVERNMENT

CENTRAL INTELLIGENCE AGENCY

ATTN: OSWR/NED 5S09 NHB

DEPARTMENT OF DEFENSE CONTRACTORS

ANALYSIS & TECHNOLOGY INC

ATTN: V GODINO

APPLIED RESEARCH ASSOCIATES, INC

ATTN: R FRANK

CALIFORNIA INSTITUTE OF TECHNOLOGY

ATTN: T AHRENS

COLUMBIA UNIVERSITY

ATTN: F DIMAGGIO

GENERAL DYNAMICS CORP

ATTN: AUSTIN ALVAREZ
ATTN: D BARASSO

DNA-TR-95-76 (DL CONTINUED)

JAYCOR
ATTN: CYRUS P KNOWLES

KAMAN SCIENCES CORP
ATTN: LIBRARY

KAMAN SCIENCES CORPORATION
ATTN: DASAC

LOCKHEED MARTIN CORPORATION
ATTN: TECH INFO CTR D/COLL

MAXWELL LABORATORIES INC
ATTN: K D PYATT JR
ATTN: R SEDGEWICK

MISSION RESEARCH CORP
2 CY ATTN: G R HESS

NKF ENGINEERING INC
ATTN: T MOYER

PACIFIC-SIERRA RESEARCH CORP
ATTN: H BRODE

SCIENCE APPLICATIONS INTL CORP
ATTN: TECHNICAL REPORT SYSTEM

TITAN CORPORATION
ATTN: J THOMSEN

TITAN CORPORATION (THE)
ATTN: LIBRARY
ATTN: S SCHUSTER

WEIDLINGER ASSOC, INC
ATTN: H LEVINE

WEIDLINGER ASSOCIATES, INC
ATTN: T DEEVY

WEIDLINGER ASSOCIATES, INC
ATTN: M BARON